Multi-Mode Squeezing of Light via Four-Wave Mixing in a Hot Rubidium Vapour

by

Joshua Samuel David Rayne

A thesis submitted to
The University of Birmingham
for the degree of
DOCTOR OF PHILOSOPHY

Ultracold Atoms Group
School of Physics and Astronomy
College of Engineering and Physical Sciences
The University of Birmingham

September 2018

Abstract

Light is used across a broad range of applications from imaging to communications. These fields have advanced sufficiently that measurements are now limited by the fundamental behaviour of light, such as fluctuations inherent to its quantum nature. This is dictated by quantum mechanics, most noticeably Heisenberg's uncertainty principle, having been adapted to describe light and form quantum optics.

As it is bound by the uncertainty principle, measuring an observable of light can be made more accurate by adding uncertainty to conjugate observables. This improved accuracy is then gauged against the quantum noise limit (QNL) of the measured observable. Such measurements are then squeezed where the noise of the measurement is below this QNL.

In this thesis, we examine the squeezing of light via four wave mixing (4WM) in a rubidium 85 (Rb85) atomic vapour. This includes the generation and detection of squeezed light in its temporal and spatial degrees of freedom. We consider various methods of detection, such as homodyne detection to measure field quadratures, then intensity difference after a waveguide to observe preservation of local correlations, and finally local intensity difference squeezing with a CCD camera.

The three experiments each present different results. The broadband squeezing of light yielded variable squeezing across a bandwidth of 60MHz, displaying the multi-temporal mode nature of the process. Photodetection measurements and intensity difference of entangled light after being passed through a waveguide displayed local correlations between a range of corresponding regions within the beam profile, with squeezing of $\sim$-1dB. CCD photodetection and intensity difference of this light showed squeezing of approximately -0.75dB in a single set of spatial Fourier frequencies encircling the central spatial frequency, 0mm^{-1}, also referred to as DC, corresponding to 8 distinct squeezed spatial modes within the beams.

The use of a waveguide in transmitting local multi-spatial mode (MSM) correlations presents interesting possibilities in guiding said correlations for use in quantum communications and encryption protocols, with a vastly improved bit rate, if not also transmission of quantum images. This supplements the use of a CCD camera in measuring local MSM correlations in these beams which, in yielding positive results, can be utilized as a means of improved imaging beyond the QNL.

Given this exhaustive computational investigation, the results have conclusively shown MSM squeezing in signal beams generated from 4WM in a Rb85 vapour. Using the results from Chapter 6, this squeezing is distributed across 8 distinct spatial modes, with vertical spatial frequencies of $\pm 4.96\text{mm}^{-1}$, $\pm 2.48\text{mm}^{-1}$ and 0mm^{-1} and horizontal frequencies $\pm 0.60\text{mm}^{-1}$, $\pm 0.30\text{mm}^{-1}$ and 0mm^{-1}.

These frequencies correspond to real space vertical sizes of 0.20mm and 0.40mm and horizontal sizes of 1.66mm and 3.33mm. These can be seen to be MSM squeezed regions, given that the size of the beams in the results were larger than this. The average height of the probe was 0.70mm, while the conjugate was 0.66mm while the average lengths were 6.17mm and 5.95mm. As these size exceed the length scales derived from the spatial frequencies, these frequencies thus show MSM squeezing.

Acknowledgements

I would like to thank Dr. Vincent Boyer, Dr. Plamen Petrov Dr. Chris Embrey and Dr. Chris Gill for their help during my PhD, as well as Dr. Anna Kowalcyzk, Dr. Giovanni Barontini and Dr. Daniel Orenes for their help with our collaborative work. Thanks also to Professor Kai Bongs for organising the opportunity and the DSTL for funding my research. I would also like to thank my wife, Kondwa, for her patience and support. Mentions also go to colleagues and friends Andrew Lamb, Andrew White, Dr. Lyndsie Smith, Kae Graham, Ellie Fradgley and Qasim Ubaid as well as the University of Birmingham Kickboxing Society.

Contents

List of Figures

Chapter 1

Introduction

The way light is perceived and understood has changed substantially over the course of the last century, being founded in classical interpretations of light, [1] [2] [3], with recent years seeing elaboration of this theory through quantum mechanics and quantum field theory [4] [5]. Though the issues addressed by these investigations have varied, its main concern has been measurement, not only pertaining to the fundamental nature of light [6] [7], but into how light itself propagates and behaves [8]. Such studies into light have garnered improvements in imaging [9] [10] [11] and communications [12] [13] [14] [15]. The culmination of this progress has exceeded classical limits, requiring even more intricate understanding and manipulation to improve further.

More specifically, light-based systems and investigations have encountered problems with the fundamental nature of light itself, a restriction on the manipulation and arrangement of photons [16] [17]. This inherent limit arises from the nature of quantised light, where any two non-commuting observables of light, $\hat{A}$ and $\hat{B}$, have their uncertainty bound by an uncertainty principle of the form:

$$\Delta\hat{A}\Delta\hat{B} \geq \frac{|[\hat{A}, \hat{B}]|}{2}$$

as found in [18]. It is due to this behaviour that these observables can not be simultaneously measured with accuracy greater than this principle imposes. They are thus bound to display quantum uncertainty. However, the behaviour of this restriction can be exploited given appropriate technique [19]. Thus to proceed requires more technical handling of light, one such phenomenon being squeezing [20]. This technique takes advantage of the same uncertainty principle that restricts measurement, by increasing the fluctuation on one non-commuting observable to improve measurements of the other.

Intuitively, the kind of squeezing will depend on the observables being squeezed. This thesis presents investigations into multi-mode squeezing, which considers simultaneous and multitudinous EM field pair generation within an amplified beam of light. The multi-mode squeezing of the EM fields refers to squeezing over a mode basis, typically involving either frequency or spatial frequency. The relevant observables will hence vary according to these modes, though being quantised they are still subject to quantum limitations.

This behaviour in the fluctuations of these quantised observables naturally occurs within Quantum Mechanics, applicable in this case due to its quantisation of light. The very first instance of this treatment of light was proposed by Einstein in his 1905 paper [21]. The concepts introduced in this paper would be further utilized by Bohr in his own paper in 1913 [22], and eventually led to de Broglie forming a generalized formalism for quantisation that included particles in 1925 [23].

From there, Heisenberg, Schrodinger and Dirac then formulated the familiar mathematics that persists in quantum mechanics today [24] [25] [26], followed by Born's probability interpretation of these quantum mechanics a year later [27]. Such works allowed for the aforementioned individual efforts by Heisenberg and Kennard in expressing uncertainty of observables and its application to light [16] [17] respectively.

Efforts progressed from there with Fermi and Dirac investigating further into the expression of and interactions between quantized light and atoms [28] [29]. Here the history of quantum

mechanics delves mostly into particle physics, including Einstein, Podolsky and Rosen's seminal paper on the absurdity of some of quantum mechanic's conclusions at the time [30]. It was in 1950s that quantum optics, the quantum theory of light, began to separate into its own subject through studies on intensity correlations [31]. Alongside these efforts were ongoing investigations into maser technology, which culminated in the inception of laser technology in 1960 [32]. As a result of these breakthroughs, the 1960s saw an explosion of papers on the theory of light [33–41], including a Nobel prize-winning paper on optical coherence by Glauber [34]. These papers provided a solid foundation for further development in quantum optics.

This progress continued into the 1970s and 80s [42], with this prolonged period of interest in quantum optics resulting in a variety of experimental systems being designed and implemented. The specifics of their motivations and experiments varied from improved optical communication [43] to overcoming amplifier noise limitation [44] to noise-free imaging [45], but all shared a common goal of more accurate measurements involving light-based systems.

The 1980s saw the most successful realisation of quantum optics to date, with experiments typically explored one of three means of generating "non-classical light": parametric down conversion , converting photons of a certain frequency to photon pairs of half that frequency, four wave mixing (4WM), the intermixing of photons corresponding to certain atomic transitions, and optical parametric oscillators , generating correlated intensities via parametric down conversion in a cavity.

For the most part, the schemes were successful in generating positive results. Through the use of parametric down conversion in a MgO:$LiNbOs_3$ crystal, Wu et al. showed a noise reduction of 3dB, relative to the vacuum noise level, in the amplitude of generated light via a balanced homodyne detector in 1986 [46]. Utilisation of 4WM also garnered results, with Slusher et al. presenting a 0.3dB decrease in noise via homodyne detection of correlated light, and $\sim$1dB noise reduction in vacuum noise, produced from 4WM in Sodium vapour

in 1985 [47], and two years later Slusher, Yurke et al. went on to demonstrate 0.6dB below shot noise decrease in squeezed light pulses, generated through the use of 4WM in $KTiOPO_4$ crystals in 1987 [48]. Further to this, Slusher, Yurke, Grangier et al. also demonstrated 4WM with greater than 1dB noise reduction in the same year [49]. The use of optical parametric oscillators was not overlooked, with Slusher, Yurke, La Porta et al. demonstrating 2dB decrease in noise of a polarisation interferometer using squeezed later in 1985 [50].

Though promising, these investigations were ultimately inapplicable outside of scientific context, lacking adequate efficiency and resolution to be of ulterior use. Despite this, however, the same physics behind these studies not only expanded quantum optics and quantum mechanics in general, but found theoretical utility in data encryption with the development of quantum key distribution [51] [52].

In addition, quantum optics found further consideration in quantum communications as a means of establishing a benchmark for improved bit rates [53]. Meanwhile, during 1995, Kwiat et al. developed a set-up using beta barium borate crystal that was capable of emitting adequate intensity beams, correlated not by the intensities themselves, but by polarization [54]. This same arrangement went on to be adapted by Poppe et al. who, in 2004, used it to conduct the first bank transfer using quantum key distribution [56]. In the same year, Beskrovnyy and Kolobov made progress in quantum imaging through the use of prolate spheroidal functions in restoring and extrapolating images beyond the diffraction limit and up to the quantum limit of light [55].

Shortly after these breakthroughs, 2007 and 2008 saw further breakthroughs in quantum optics, the first of which was McCormick et al., who presented results on intensity correlations generated from rubidium yielded noise reductions of 3.5dB below coherent levels, due to the increased gain of their 4WM [57]. This was beaten a year later by Vahlbruch et al, who increased this precedent to 10dB [58].

In the same year, Halder et al showed how spontaneous parametric down conversion in

rubidium produces signals able to sustain quantum communication protocols [59], while Boyer et al. showed how 4WM in rubidium could be seen to exhibit MSM correlations in the far field using a pair of slits and a pair of photodetectors [60]. Boyer, Marino et al. went on to show how the same scheme could be used for homodyne detection in 2009, with a 4dB decrease in noise in either the amplitude or phase, depending on the combination of photons being generated, and could be used in imaging [61].

With the inadequacy of the schemes from the 1990s addressed, progress continued from there with further implementations. In 2011, Eckstein et al. used beams generated from parametric down conversion in a PP-KTP waveguide to show a decrease in noise across a wide range of frequencies within the telecom wavelength regime [62], useful for telecommunications. In 2012, Marino et al. presented a set-up capable of amplifying a vast range of spatial modes, once again through 4WM in rubidium [63]. This was the first experiment to advertise the quantum imaging capability of 4WM in rubidium, and a pivotal breakthrough in establishing it as a means of doing so. Thereafter, the utility of quantum optics began to become more mainstream [64].

It is around this point in time my PhD started, investigating rubidium as a means of MSM squeezed light and its application in quantum imaging. I began toward the end of Dr. Chris Embrey's PhD, who began writing his own thesis shortly after. His degree built on the work of Dr. Matt Turnbull, who worked on the set-up before him. Given the overlapping nature of their work, there is considerable overlap between their theses and mine. Hence, a lot of base material in this thesis can also be found in their work.

Building on their efforts, my project sought to unify several concepts introduced throughout quantum optics, with an aim to provide imaging beyond both the conventional (classical) and quantum limit. During this time, I was also able to pursue additional opportunities in related experiments, yielding results outside of the original aims. During my project, I also married and assumed a change of name, from Hordell to Rayne, though my papers were

published before I could acquire a deed poll. These papers thus bear my former name.

In this thesis I present the results of three investigations into the use of Rb85 as a means of generating multi-mode correlated light beams whose fluctuations can be cancelled out through their measurement and subtraction. Though only one involves direct detection of MSM, the mechanism for generating the correlations is the same throughout.

These experiments are demonstrations of broadband squeezing of light via homodyne detection (referred to as the BLO experiment, published in [65]), waveguidance and subsequent detection of squeezing through a conduit (referred to as the conduit experiment, published as [66]) and imaging and detection of MSM squeezed light via CCD camera (referred to as the camera experiment).

This thesis proceeds from here with Chapter 2, an explanation of Quantum Optics and the necessary theory to describe the EM fields required to achieve squeezing, limited to the expressions most relevant to our experiments. Chapter 3 continues this theory through more detailed explanations of the experiment's characteristics, using Nonlinear Optics to show how the expressions from Chapter 2 are realised by our chosen medium. Chapter 4 provides general details on the experiments, as well as the results and analysis from the first two experiments. Chapter 5 then presents the third and final experiment, its analysis and results, while Chapter 6 summarizes and concludes the thesis.

Chapter 2

Quantum Theory of Light

In this chapter, we examine the theory of the fluctuations of light as observed by the detection methods used in the experiments detailed later. These observables are photon number and field quadratures, as measured by intensity difference and homodyne detection measurements respectively.

We outline the theoretical background of the quantum nature of light, the resulting fluctuations and how the quantum state of light can be manipulated to observe lower levels of noise. In particular, we then proceed to outline the behaviour of the fluctuations of the observables of interest and provide a metric for measuring the noise reduction, called the Quantum Noise Reduction (QNR).

This section then presents the theory on achieving this noise reduction via an idealised amplifier. This theory concludes with several equations, notably the uncertainty principles for our observables of interest, an equation to provide the QNR of these observables, an amplification equation for operators on which the observables depend and how these equations can be used to lower the quantum noise. This chapter is largely taken and adapted from [4], [5] and [67].

2.1 Quantisation of Light

As we intend to manipulate our observables of interest in the quantum regime, we must first specify their quantum nature. To do so, we will relate these observables to their shared originator, light, for which we will derive a quantised expression for the field propagating in free space. We can then proceed to show how these observables and their uncertainties follow certain relations, how these relations are used to define squeezing and present the metric we will use to observe noise reduction, the QNR. Thus this section details the quantum theory of light with regard to our observables of interest and provide a general description of squeezing.

2.1.1 Quantised Light & Fluctuations

As stated, we begin by deriving a quantisable expression for light propagating in free space. We then quantise this equation, before relating it to our observables of interest. First, we consider the EM wave equations:

$$\begin{aligned} \left(c^2\nabla^2 - \frac{\partial^2}{\partial t^2}\right)\mathbf{E} = 0, \\ \left(c^2\nabla^2 - \frac{\partial^2}{\partial t^2}\right)\mathbf{B} = 0. \end{aligned} \tag{2.1}$$

Here $\mathbf{E}$ and $\mathbf{B}$ are the electric and magnetic vector fields respectively.We can then take the example of a plane wave and assume an EM field of the form:

$$\begin{aligned} \mathbf{E}(\mathbf{r},t) = [E_x(z,t),0,0] \text{ with } E_x(z,t) = \sqrt{\frac{2\omega^2}{\epsilon_0}}q(t)\sin(kz), \\ \mathbf{B}(\mathbf{r},t) = [0,B_y(z,t),0] \text{ with } B_y(z,t) = \frac{\mu_0\epsilon_0}{k}\sqrt{\frac{2\omega^2}{\epsilon_0}}p(t)\cos(kz). \end{aligned} \tag{2.2}$$

Here Equations 2.2 express an EM field with electric field E in the x direction and magnetic field B in the y direction, both propagating along z, with frequency ω and wavenumber k.

The factors $q(t)$ and $p(t)$ are the canonical position and momentum of a harmonic oscillator of unit mass, respectively (see Appendix A for validation of Equations 2.2). We can then obtain the energy of this field from its Hamiltonian, given as:

$$H = \frac{1}{2}\int_{-\infty}^{\infty}\left[\epsilon_0 E_x^2(z,t) + \frac{1}{\mu_0}B_y^2(z,t)\right]dz. \tag{2.3}$$

Using Equations 2.2, Equation 2.3 can be reduced to:

$$H = \frac{1}{2}(p(t)^2 + \omega^2 q(t)^2). \tag{2.4}$$

Equation 2.4 thus makes it apparent that an EM field of frequency ω is analogous to a harmonic oscillator of unit mass, with E and B themselves being analogous to q and p, respectively. This same model can then be quantised by invoking the correspondence rule with regards to the canonical factors q and p, giving:

$$\begin{aligned}\hat{E}_x(z,t) &= \sqrt{\frac{2\omega^2}{\epsilon_0}}\hat{q}(t)\sin(kz),\\ \hat{B}_y(z,t) &= \frac{\mu_0\epsilon_0}{k}\sqrt{\frac{2\omega^2}{\epsilon_0}}\hat{p}(t)\cos(kz).\end{aligned} \tag{2.5}$$

Equation 2.5 provides quantised expressions of the electric and magnetic field and a means of expressing quantised light. We are going to show that our observables can be related to these fields through the following expressions:

$$\begin{aligned}\hat{E}_x^2 &= 2\mathcal{E}_0^2\sin^2(kz)\left(\hat{n}+\frac{1}{2}\right),\\ \hat{B}_y^2 &= -2\mathcal{B}_0^2\cos^2(kz)\left(\hat{n}+\frac{1}{2}\right),\\ \hat{E}_x(z,t) &= 2\mathcal{E}_0\sin(kz)(\hat{X}\cos(\omega t)+\hat{Y}\sin(\omega t)),\\ \hat{B}_y(z,t) &= -i2\mathcal{B}_0\cos(kz)(\hat{X}\cos(\omega t)-\hat{Y}\sin(\omega t)).\end{aligned} \tag{2.6}$$

Here $\mathcal{E}_0$ and $\mathcal{B}_0$ represent the electric and magnetic fields "per photon" respectively, $\hat{n}$ is the photon number operator, directly related to intensity, $\hat{I}$, and $\hat{X}$ and $\hat{Y}$ are the field quadrature operators. As Equations 2.6 show an interrelation between $\hat{n}$, $\hat{X}$, $\hat{Y}$, $\hat{E}$ and $\hat{B}$, it is clear that their behaviour, including their fluctuations, are interlinked. We can demonstrate this interrelation more simply by introducing the annihilation operator, $\hat{a}$, on which our observables and light share a dependency. Using known results for the quantum harmonic oscillator, we introduce expressions for the annihilation and creation operators similar to those for said oscillator:

$$\begin{aligned} \hat{a}(t) &= \sqrt{2\hbar\omega}(\omega\hat{q}(t) + i\hat{p}(t) \\ \hat{a}^\dagger(t) &= \sqrt{2\hbar\omega}(\omega\hat{q}(t) - i\hat{p}(t)), \end{aligned} \tag{2.7}$$

where the time evolution is given by (as in Appendix A):

$$\begin{aligned} \hat{a}(t) &= \hat{a}(0)e^{-i\omega t}, \\ \hat{a}^\dagger(t) &= \hat{a}^\dagger(0)e^{-i\omega t}. \end{aligned} \tag{2.8}$$

Similarly to the quantum harmonic oscillator, the annihilation and creation operators increase or decrease the energy of the quantum state of light. In terms of number states, these operators correspond to increasing or decreasing photon number by one photon of a certain frequency, ω. Substituting Equation 2.7 into Equations 2.5, we obtain the following expressions for our EM field:

$$\begin{aligned} \hat{E}_x(z,t) &= \mathcal{E}_0(\hat{a}(t) + \hat{a}^\dagger(t))\sin(kz), \\ \hat{B}_y(z,t) &= -i\mathcal{B}_0(\hat{a}(t) - \hat{a}^\dagger(t))\cos(kz). \end{aligned} \tag{2.9}$$

From here, we can relate our EM field to our observables of interest through relating said observables to the annihilation and creation operators:

$$\hat{n} = \hat{a}^\dagger(t)\hat{a}(t), \tag{2.10}$$

$$\begin{aligned} \hat{X}(t) &= \sqrt{\frac{\omega}{2\hbar}}\hat{q}(t) = \frac{\hat{a}(t) + \hat{a}^\dagger(t)}{2}, \\ \hat{Y}(t) &= \sqrt{\frac{\omega}{2\hbar}}\hat{p}(t) = \frac{\hat{a}(t) - \hat{a}^\dagger(t)}{2i}. \end{aligned} \tag{2.11}$$

Substituting Equations 2.10 and 2.11 into Equations 2.9 then returns Equations 2.6. Equations 2.9, 2.10 and 2.11 also allow us to express the fluctuations of our observables through a single operator, $\hat{a}$. From Equations 2.11 it can also be seen that the quadratures operators are in fact the operators q and p scaled to be dimensionless. Despite this relation to $\hat{a}$, we do not intend to measure $\langle\hat{a}\rangle$, as the annihilation operator is unobservable. However, we can still derive the behaviour of our observables from $\hat{a}$, for which we introduce coherent states, $|\alpha\rangle$ with $\alpha > 0$, to facilitate this approach:

$$\begin{aligned} \hat{a}|\alpha\rangle &= \alpha|\alpha\rangle, \\ \langle\alpha|\hat{a}^\dagger &= \alpha^*\langle\alpha|. \end{aligned} \tag{2.12}$$

As can be seen from Equation 2.12, these coherent states are an eigenstate of the annihilation operator, which provides us with a means of obtaining expectation values for our observables. Moreover, these coherent states are near-classical quantum states of an EM field. This can

be shown, for instance, through using $|\alpha\rangle$ to calculate the variance of a coherent state:

$$\begin{aligned}
\mathrm{Var}(\hat{a}^\dagger\hat{a})_{|\alpha\rangle} &= \langle\alpha|(\hat{a}^\dagger\hat{a})^2|\alpha\rangle - \langle\alpha|\hat{a}^\dagger\hat{a}|\alpha\rangle^2 \\
&= \langle\alpha|\hat{a}^\dagger\hat{a}\hat{a}^\dagger\hat{a}|\alpha\rangle - \langle\alpha|\hat{a}^\dagger\hat{a}|\alpha\rangle^2 \\
&= \langle\alpha|\hat{a}^\dagger\hat{a}^\dagger\hat{a}\hat{a} + \hat{a}^\dagger\hat{a}|\alpha\rangle - \langle\alpha|\hat{a}^\dagger\hat{a}|\alpha\rangle^2 \\
&= |\alpha|^4 + |\alpha|^2 - |\alpha|^4 \\
&= |\alpha|^2
\end{aligned} \tag{2.13}$$

As previously stated, these states can then used to obtain to expectation values of our observables, which from Equations 2.10 and 2.11 give the following:

$$\begin{aligned}
\langle\hat{n}\rangle &= \langle\alpha|\hat{a}^\dagger\hat{a}|\alpha\rangle = \alpha^*\alpha = |\alpha|^2 = \bar{n}, \\
\langle\hat{X}\rangle &= \frac{\langle\alpha|\hat{a} + \hat{a}^\dagger|\alpha\rangle}{2} = \frac{\alpha + \alpha^*}{2} = \bar{X}, \\
\langle\hat{Y}\rangle &= \frac{\langle\alpha|\hat{a} - \hat{a}^\dagger|\alpha\rangle}{2i} = \frac{\alpha - \alpha^*}{2i} = \bar{Y}.
\end{aligned} \tag{2.14}$$

Here $\bar{n}$, $\bar{X}$ and $\bar{Y}$ are the mean values of the photon number and field quadratures respectively. Thus we continue to consider our original observables and the EM field, with the intent to observe and manipulate them and their fluctuations. Specifically, it is these fluctuations that we intend to decrease in order to improve our measurements with light. To do so, we must first elaborate on the behaviour of such fluctuations,.

Given their quantum nature, our observables are now subject to quantum effects, one of which is the non-commutation of certain operators. As introduced in Chapter 1, given any two non-commuting operators, $\hat{\mathcal{O}}_1$ and $\hat{\mathcal{O}}_2$, and their commutation $[\hat{\mathcal{O}}_1, \hat{\mathcal{O}}_2] = \hat{\mathcal{O}}_3$, we find that there exists an uncertainty principle of the form [18]:

$$\Delta\hat{\mathcal{O}}_1\Delta\hat{\mathcal{O}}_2 \geq |\langle\hat{\mathcal{O}}_3\rangle/2| \text{ or } \mathrm{Var}(\hat{\mathcal{O}}_1)\mathrm{Var}(\hat{\mathcal{O}}_2) \geq \langle|\hat{\mathcal{O}}_3^2|\rangle/4. \tag{2.15}$$

Here $\Delta\hat{\mathcal{O}}$ is the standard deviation of $\mathcal{O}$ and $\mathrm{Var}(\hat{\mathcal{O}})$ is the variance of $\hat{\mathcal{O}}$. Thus, the fluctuations of our observables are bound to a certain minimum limit. This limit, $|\langle\hat{\mathcal{O}}_3\rangle/2|$ or $\langle|\hat{\mathcal{O}}_3^2|\rangle/4$, is the Quantum Noise Limit (QNL). As such, these fluctuations impose an unavoidable minimum amount of noise on our observables. However, given the form of this uncertainty principle, we may still proceed to lower the fluctuations of one of our observables of interest, providing the fluctuations of the corresponding non-commuting observable are raised in compensation, a technique referred to as "squeezing". In the case of our observables, $\hat{X}$, $\hat{Y}$ and $\hat{n}$, they exhibit a non-commutative nature which can be seen to stem from their dependency on $\hat{a}$, which itself is given by the following commutation:

$$[\hat{a}, \hat{a}^\dagger] = 1. \tag{2.16}$$

Having defined what constitutes squeezing, we now look to quantify it with an appropriate and intuitive metric, which we define as the Quantum Noise Reduction (QNR). For some measured observable, $\langle\hat{\mathcal{O}}\rangle$, the QNR is given by:

$$\mathrm{QNR} = \frac{\mathrm{Var}(\hat{\mathcal{O}})}{\mathrm{Var}(\hat{\mathcal{O}})_{\mathcal{C}}}. \tag{2.17}$$

Here the subscript $\mathcal{C}$ refers to a coherent state of equivalent brightness to the detected state. This coherent state corresponds to the QNL of the measured observable and exhibits fluctuations $\mathrm{Var}(\hat{\mathcal{O}})_{\mathcal{C}}$. These fluctuations are equal for either observable in Equations 2.15, such that $\mathrm{Var}(\hat{\mathcal{O}}_1) = \mathrm{Var}(\hat{\mathcal{O}}_2) = \mathrm{Var}(\hat{\mathcal{O}})_{\mathcal{C}} = \sqrt{\langle|\hat{\mathcal{O}}_3^2|\rangle/4}$. The measured observable, $\hat{\mathcal{O}}$, is then squeezed if its fluctuations, $\mathrm{Var}(\hat{\mathcal{O}})$, fall below the value of the QNL, and the QNR resultantly falls below 1.

2.1.2 Quadrature & Photon Number Fluctuations

Proceeding to squeezing of our observables, we first consider squeezing of the field quadratures, $\hat{X}$ and $\hat{Y}$, for which we will note their shared commutation:

$$[\hat{X}, \hat{Y}] = \frac{i}{2}. \tag{2.18}$$

In the context of Equations 2.15, Equation 2.18 indicates that squeezing of these observables is limited to either $\hat{X}$ or $\hat{Y}$, but not both simultaneously. Thus, from Equations 2.15 and 2.18, we obtain the following:

$$\mathrm{Var}(\hat{X})\mathrm{Var}(\hat{Y}) \geq \frac{1}{16}. \tag{2.19}$$

Here Equation 2.19 gives the QNL on light's fluctuations via the product of the variances of the quadratures. For brevity, the photon number uncertainty principle is taken from the result of a derivation in [4] (pg.135-136), and is given here as:

$$\Delta\hat{n}\Delta\hat{\theta} \geq \frac{1}{2}. \tag{2.20}$$

In the referenced derivation, Equation 2.20 only holds providing that the average photon number remains sufficiently large enough, $\langle\hat{n}\rangle \gg 1$, and for a state close to a coherent state, such as in Figure 2.1c). In the context of the applicable experiments (the conduit and camera experiment) featured later in Chapters 5 and 6, this assumption holds as the results of such experiments concern the measurement of bright states. For clarity, we now present these observables and their fluctuations in phase space, depicted as bright states where $\alpha \gg 0$ and $\bar{n} \gg 0$, in Figure 2.1.

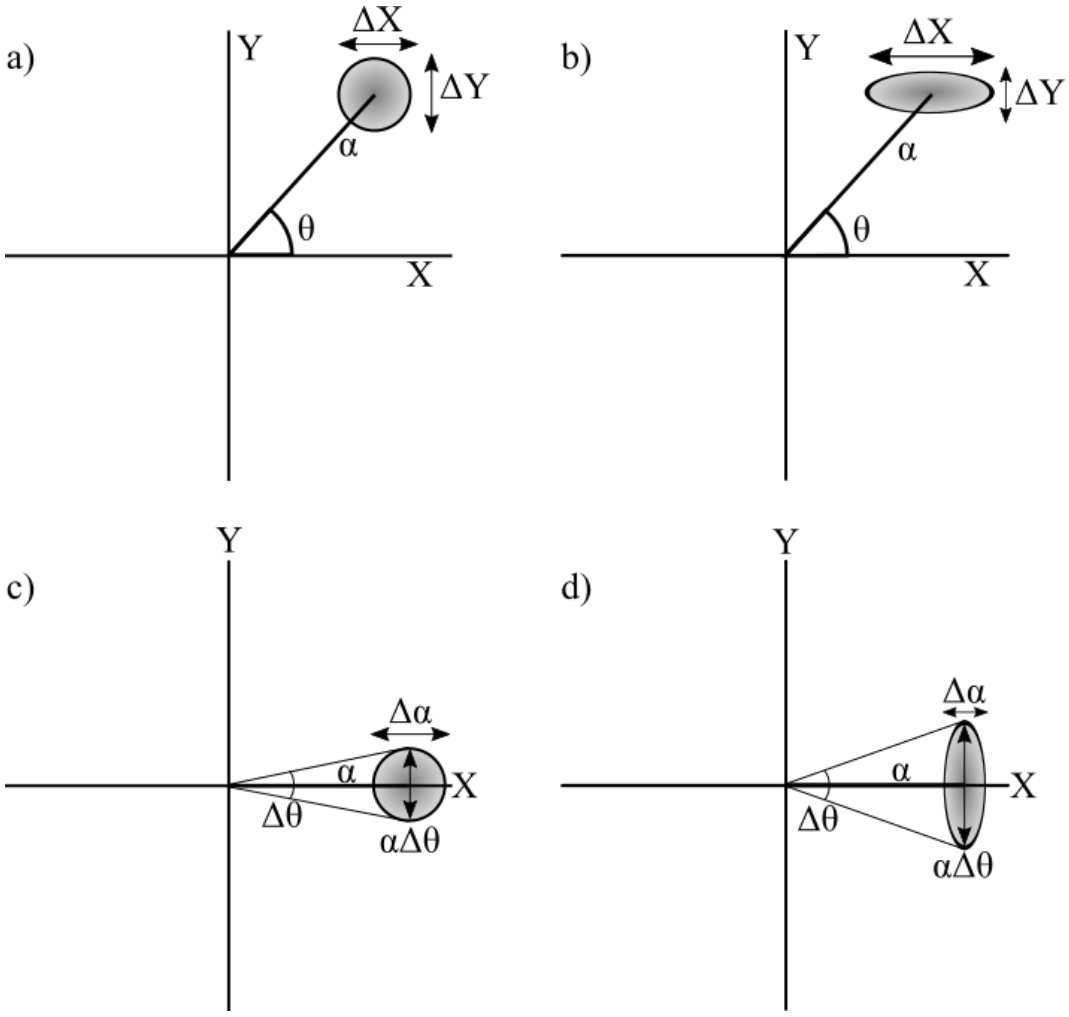

Figure 2.1: Representation of uncertainties in phase space. Diagrams a) and b) display the behaviour of the field quadratures and their uncertainties for a coherent and squeezed state respectively. Diagrams c) and d) display the behaviour of the same state with $\theta = 0$ phase when unsqueezed and amplitude squeezed respectively.

Here the length of the phasor (the displacement from the origin) is equivalent to the eigenvalue α. As can be seen from Equation 2.13, α is proportional to the mean photon number of the state, $\bar{n}$, in fact being equivalent to $\sqrt{\bar{n}}$. This relates the uncertainty $\Delta\alpha$ to the photon number uncertainty $\Delta\hat{n}$, through which Equation 2.20 can be found. The

measurable phase, θ, of the state is the angle made between the phasor and the X axis. We have thus established the quantum nature of our observables' fluctuations, theoretically showing their potential for squeezing. We will discuss more specifically how this is achieved and how QNR is applied as a metric during Section 2.3.

2.2 Multimode Light

Before theoretically demonstrating squeezing, here we introduce mode descriptions of light, divided into longitudinal and transverse modes. These modes provide a shorthand referring to particular aspects of light, specifically referring to either temporal behaviour of the EM field along the propagation axis (longitudinal modes) or the spatial distribution of the EM field perpendicular to it (transverse modes). These modes also distinguish between the different bases measured in Chapters 5 and 6.

We introduce these modes by revisiting the EM field expressions in Equations 2.2 and, by restricting our approach to modes propagating along the z axis, instead consider the following decomposition:

$$\mathbf{E}(x, y, z, t) = \mathbf{E}(x, y)\mathbf{E}(z, t) \tag{2.21}$$

Here we have decomposed the EM field into generic transverse and longitudinal mode EM fields, and can now impose mode conditions on them independently.

2.2.1 Longitudinal Modes

Here we consider the original quantisation of our EM field from the previous section, which was quantised in free space. Longitudinal modes can be imposed by emphasising the role of the frequency in the EM field expression, for which we consider the $\mathbf{E}(z, t)$ part of our EM field. More to the point, we can observe how the annihilation operator depends on frequency. Here we refer back to Equation 2.16, and note that including the frequency dependency from

Equation 2.8 yields:

$$\begin{aligned}[\hat{a}_\omega(t), \hat{a}_{\omega'}(t)] &= 0 = [\hat{a}^\dagger_\omega(t), \hat{a}^\dagger_{\omega'}(t)], \\ [\hat{a}_\omega(t), \hat{a}^\dagger_{\omega'}(t)] &= \delta(\omega - \omega').\end{aligned} \tag{2.22}$$

Here $\hat{a}_\omega(t) = \hat{a}_\omega(0)e^{-i\omega t}$ and the subscripts ω and ω' refer to two different modes by their frequencies. Equations 2.22 thus shows the general behaviour of operators associated with our EM field: that the same operators of two modes commute, while the different operators of any and all modes do not. Despite this, we can still obtain the same uncertainty principles for observables of different modes as before, though now they are additionally denoted by that mode's frequency. This does not alter the final results either, but only adds the caveat of similar modes having commutable annihilation operators.

2.2.2 Transverse Modes

To examine transverse modes, we now consider the $\mathbf{E}(x, y)$ part of our EM field. Unlike longitudinal modes, transverse modes require an arbitrary basis of orthogonal modes, signified by $\mathbf{E}_i(x, y)$. They can be quantised as previously, though in this case it is more useful to quantise with regard to their axes, and with modes that are more appropriate, such as the Hermite-Gauss modes, or any of the Transverse Electro-Magnetic modes. Despite this, the annihilation operators of these field modes follow the same result as the previous section, where same operators of different modes commute and different operators of differing modes do not:

$$\begin{aligned}[\hat{a}_i, \hat{a}_j] &= 0 = [\hat{a}^\dagger_i, \hat{a}^\dagger_j], \\ [\hat{a}_i, \hat{a}^\dagger_j] &= \delta_{ij}.\end{aligned} \tag{2.23}$$

Here $\hat{a}_i$ and $\hat{a}_j$ are annihilation operators from two different transverse field modes, as denoted by the i and j subscripts.

2.3 Squeezing of Light

Having expressed the EM fields in terms of quantum operators and summarised their mode dependency, we return to the subject of squeezing as presented in Section 2.1. We recall our observables of interest, photon number and field quadratures, upon which we intend to impose greater accuracy via squeezing. We also recall the annihilation operator, $\hat{a}$, and its relation to these observables. We now introduce and apply our means of squeezing, an idealised amplifier, to our original annihilation operator, $\hat{a}$ and use the resultant annihilation operator, $\hat{b}$, to obtain the relevant QNR expressions.

2.3.1 Optical Amplification of Light

We begin by specifying the operation of this amplifier on the annihilation operator. Here we introduce two generic longitudinal mode fields, 1 and 2, with arbitrary transverse modes, which we pass through the amplifier. This approach is modelled on material found in [4]. The effect of the amplifier on the annihilation and creation operators, $\hat{a}_j$ and $\hat{a}_j^\dagger$, is given as follows:

$$\begin{aligned} \hat{b}_1 &= U_1\hat{a}_1 + V_1\hat{a}_2^\dagger, \\ \hat{b}_2 &= U_2\hat{a}_2 + V_2\hat{a}_1^\dagger. \end{aligned} \tag{2.24}$$

Here $\hat{b}_j$ are the output annihilation operators from the amplifier, U_j and V_j are functions dependent on s, which is the squeezing parameter, both real and positive. For the operators $\hat{b}_1$,$\hat{b}_1^\dagger$ and $\hat{b}_2$,$\hat{b}_2^\dagger$ to follow a canonical commutation relation $[\hat{b}, \hat{b}^\dagger] = 1$, U_j and V_j must follow the relations $|U_j|^2 - |V_j|^2 = 1$ and $U_1V_2 = U_2V_1$. We then satisfy this requirement by selecting

$U_1 = U_2 = U = \cosh(s)$ and $V_1 = V_2 = V = \sinh(s)$. Thus we obtain:

$$\begin{aligned} \hat{b}_1 &= \cosh(s)\hat{a}_1 + \sinh(s)\hat{a}_2^\dagger, \\ \hat{b}_2 &= \cosh(s)\hat{a}_2 + \sinh(s)\hat{a}_1^\dagger. \end{aligned} \tag{2.25}$$

The output EM field will hence be defined by these operators, $\hat{b}$, which, by Equations 2.24 and 2.25, are correlated by the inputs, $\hat{a}$. This shared input dependency is also exhibited as correlations between the fields' fluctuations. In the context of our experiments, these inputs, $\hat{a}$, are referred to as seeds, while the outputs, $\hat{b}$, are referred to as signals. As this is amplification, we introduce the gain of the amplifier, G, for which $\sqrt{G} = \cosh(s)$ and $\sqrt{G-1} = \sinh(s)$.

As both the seeds and signals are defined in terms of these operators, they are thus quantised and have the properties of the annihilation operator. The resultant correlations in the aforementioned signals will thus be of a quantum nature. Subsequently, this can be exploited to achieve squeezing in our observables of interest, as will be discussed in the following section.

2.3.2 Intensity Difference Squeezing

Previously we established photon number and photon number squeezing as our observable of interest and means of reducing its fluctuation. In this section, we introduce intensity difference squeezing as a means of achieving such squeezing. As intensity is proportional to photon number, squeezing the intensity of a field will squeeze photon number. Thus, given two correlated intensities, we can reduce their fluctuation through cancellation by subtracting them, referred to as intensity difference squeezing. It is via this method we aim to achieve photon number squeezing.

As in Section 2.3.1, we direct two seed states into our amplifier. For our purposes, a coherent state, $|\alpha\rangle$, and a vacuum number state, $|0\rangle$ will suffice (which is to say, practically, only one

seed is directed into the amplifier). These states can thus be represented as a single product state, $|\alpha, 0\rangle$. We then utilise Equations 2.25 to obtain the signal photon numbers, $\hat{n}_1$ and $\hat{n}_2$:

$$\begin{aligned} \langle \alpha, 0|\hat{n}_1|\alpha, 0\rangle &= \langle \alpha, 0|\hat{b}_1^\dagger \hat{b}_1|\alpha, 0\rangle = |\alpha|^2 G + G - 1, \\ \langle \alpha, 0|\hat{n}_2|\alpha, 0\rangle &= \langle \alpha, 0|\hat{b}_2^\dagger \hat{b}_2|\alpha, 0\rangle = |\alpha|^2 (G-1) + G. \end{aligned} \tag{2.26}$$

Despite one of the seeds being vacuum, the signals are still clearly linked through the parameter, s, and the coherent seed, α. To observe this correlation between the signals, and subsequently squeezing, we first measure these states directly via their intensities :

$$\begin{aligned} \langle \hat{I}_1 \rangle \propto \langle \hat{n}_1 \rangle &= \langle \hat{b}_1^\dagger \hat{b}_1 \rangle = |\alpha|^2 G + G - 1, \\ \langle \hat{I}_2 \rangle \propto \langle \hat{n}_2 \rangle &= \langle \hat{b}_2^\dagger \hat{b}_2 \rangle = |\alpha|^2 (G-1) + G. \end{aligned} \tag{2.27}$$

These intensities are then subtracted, giving the intensity difference. This returns the value $|\alpha|^2$, or equivalently the seed's mean photon number $\bar{n}$:

$$\begin{aligned} \langle \hat{I}_- \rangle = \langle \hat{I}_1 - \hat{I}_2 \rangle &\propto \langle \hat{n}_1 \rangle - \langle \hat{n}_2 \rangle \\ &= |\alpha|^2 (G - (G-1)) + (G - 1 - G) \\ &= |\alpha|^2 - 1 = \bar{n} - 1. \end{aligned} \tag{2.28}$$

Here we assume that $\bar{n}$ is sufficiently large that we can ignore the -1 (which is to be expected of a bright state). These same operators and states can further be used to find the variance of this intensity difference:

$$\begin{aligned} \mathrm{Var}(\hat{I}_-) &\propto \mathrm{Var}(\hat{n}_1 - \hat{n}_2) \\ &= \langle (\hat{b}_1^\dagger \hat{b}_1 - \hat{b}_2^\dagger \hat{b}_2)^2 \rangle - \langle \hat{b}_1^\dagger \hat{b}_1 - \hat{b}_2^\dagger \hat{b}_2 \rangle^2 \\ &= |\alpha|^2 \end{aligned} \tag{2.29}$$

Equation 2.29 hence provides the variance of our signal, $\mathrm{Var}(\hat{\mathcal{O}})$, from the QNR expression in Equation 2.17 (the full derivation can be found in Appendix B). We then obtain the QNL by calculating a coherent state of equivalent brightness. For this, we take the mean photon number of both output intensities, $\hat{I}_1$ and $\hat{I}_2$, and sum them together:

$$\begin{aligned}\langle \hat{I} \rangle_{\mathcal{C}} &= \langle \hat{I}_1 \rangle + \langle \hat{I}_2 \rangle \propto \langle \hat{n}_1 \rangle + \langle \hat{n}_2 \rangle \\ &= |\alpha|^2 (G - 1 + G) \\ &= (2G - 1)|\alpha|^2 \end{aligned} \tag{2.30}$$

As this is a coherent state, we can note, recalling Equations 2.13 and 2.14, that its variance will equal its mean, yielding:

$$\mathrm{Var}(\hat{I})_{\mathcal{C}} \propto (2G - 1)|\alpha|^2. \tag{2.31}$$

The intensity difference variance from Equation 2.29 and the QNL from Equation 2.31 are then sufficient for us to substitute them into our original expression for QNR, Equation 2.17. Thus, we observe the reduction in fluctuations to be:

$$\mathrm{QNR} = \frac{\mathrm{Var}(\hat{n})}{(2G - 1)\mathrm{Var}(\hat{n})} = \frac{1}{2G - 1} \tag{2.32}$$

Equation 2.32 shows that for an amplifier gain larger than 1, $G > 1$, the QNR falls below 1, indicating squeezing. Hence the use of an amplifier in joint amplification of signal states correlates the signals such that the variance of their subtraction results in photon number squeezing.

2.3.3 Quadrature Squeezing

We now proceed to squeezing of our other observables, field quadratures. As we intend to squeeze our quadratures by amplification, we will utilize the same set-up used to obtain

intensity difference squeezing. Thus we consider two seed states, one coherent, $|\alpha\rangle$, and the other vacuum, $|0\rangle$. As such, we retain the same product seed state, $|\alpha, 0\rangle$, and direct it into our amplifier. We then calculate the seed and resultant signal quadratures like so:

$$\begin{aligned} \hat{X}_{j,seed} &= \frac{\hat{a}_j^\dagger + \hat{a}_j}{2}, \\ \hat{Y}_{j,seed} &= \frac{i(\hat{a}_j^\dagger - \hat{a}_j)}{2}, \\ \hat{X}_{j,signal} &= \frac{\hat{b}_j^\dagger + \hat{b}_j}{2}, \\ \hat{Y}_{j,signal} &= \frac{i(\hat{b}_j^\dagger - \hat{b}_j)}{2}. \end{aligned} \tag{2.33}$$

Here the operators $\hat{a}$ and $\hat{b}$ have the same meaning as before, and the subscript $j \in 1, 2$ refers to either of the two seed states. These equations, in combination with Equations 2.24, given $U_1 = U_2 = U$ and $V_1 = V_2 = V$, can relate the seed and signal quadrature operators, detailing the operation of the amplifier on them:

$$\begin{aligned} \hat{X}_{j,signal} &= \frac{U(\hat{a}_j^\dagger + \hat{a}_j) + V(\hat{a}_h^\dagger + \hat{a}_h)}{2}, \\ \hat{Y}_{j,signal} &= \frac{i\left(U(\hat{a}_j^\dagger - \hat{a}_j) + V(\hat{a}_h^\dagger - \hat{a}_h)\right)}{2}. \end{aligned} \tag{2.34}$$

Here $h \in 1, 2$, but $h \neq j$. These subscripts correspond to the frequencies associated with either state. While the previous section showed how intensity difference squeezing was achieved through subtraction, here we note that subtraction and addition result in different

noise behaviours depending on the quadrature:

$$\begin{aligned}
\hat{X}_{-,signal} &= \frac{\hat{X}_{1,signal} - \hat{X}_{2,signal}}{\sqrt{2}} = \frac{(U-V)(\hat{a}_1 - \hat{a}_2 + \hat{a}_1^\dagger - \hat{a}_2^\dagger)}{2\sqrt{2}}, \\
\hat{Y}_{-,signal} &= \frac{\hat{Y}_{1,signal} - \hat{Y}_{2,signal}}{\sqrt{2}} = \frac{i(U+V)(\hat{a}_1^\dagger - \hat{a}_2^\dagger - \hat{a}_1 + \hat{a}_2)}{2\sqrt{2}}, \\
\hat{X}_{+,signal} &= \frac{\hat{X}_{1,signal} + \hat{X}_{2,signal}}{\sqrt{2}} = \frac{(U+V)(\hat{a}_1 + \hat{a}_2 + \hat{a}_1^\dagger + \hat{a}_2^\dagger)}{2\sqrt{2}}, \\
\hat{Y}_{+,signal} &= \frac{\hat{Y}_{1,signal} + \hat{Y}_{2,signal}}{\sqrt{2}} = \frac{i(U-V)(\hat{a}_1 + \hat{a}_2 - \hat{a}_1^\dagger - \hat{a}_2^\dagger)}{2\sqrt{2}}.
\end{aligned} \tag{2.35}$$

Here the $-$ subscript represents a difference operator while $+$ represents a sum operator. Intuitively, given correlations between $\hat{X}_{1,signal}$ and $\hat{X}_{2,signal}$, $\hat{X}_{-,signal}$ results in a cancellation of fluctuations between the signals, leading to the signal difference having a reduced noise. This is due to the nature of U and V established in Section 2.3.1, where $U-V$ tends to 0 as G tends to ∞. Conversely, $\hat{Y}_{+,signal}$ results in the same phenomena despite being a summation, as evidenced by taking the variances of Equations 2.35:

$$\begin{aligned}
\mathrm{Var}(\hat{X}_{-,signal}) &= \langle \hat{X}_{-,signal}^2 \rangle - \langle \hat{X}_{-,signal} \rangle^2 = \frac{e^{-s}}{2}, \\
\mathrm{Var}(\hat{Y}_{-,signal}) &= \langle \hat{Y}_{-,signal}^2 \rangle - \langle \hat{Y}_{-,signal} \rangle^2 = \frac{e^{s}}{2}, \\
\mathrm{Var}(\hat{X}_{+,signal}) &= \langle \hat{X}_{+,signal}^2 \rangle - \langle \hat{X}_{+,signal} \rangle^2 = \frac{e^{s}}{2}, \\
\mathrm{Var}(\hat{Y}_{+,signal}) &= \langle \hat{Y}_{+,signal}^2 \rangle - \langle \hat{Y}_{+,signal} \rangle^2 = \frac{e^{-s}}{2}.
\end{aligned} \tag{2.36}$$

These equations hence show that we can achieve signals with correlated quadratures and subsequently combine them to reduce the variance of one of the quadratures, thereby squeezing that quadrature. The degree to which either quadrature is squeezed is thus given by the same squeezing parameter as before, s. As such, the larger this parameter, the greater the amplification, the better the squeezing.

Chapter 3

Photodetection & Homodyne Detection

In the previous chapters, we established that an amplifier jointly amplifying two seed states is capable of generating quantum correlated signal states. In this chapter, we now consider the detection methods used in the experiments detailed in Chapters 5 and 6. Previously we have seen that intensity is directly proportional to photon number. In the following section we explain how the photon number is obtained via measurements of the intensity of our light.

Conversely, the field quadratures $\hat{X}$ and $\hat{Y}$ are not so obviously detected, and so we require another detection system. To this end, we implement the use of beamsplitters and homodyne detection as a means of measuring a field's quadratures.

This chapter hence details the detection of the previous chapter's states, and provides a mathematical description for the more complicated detection of field quadratures. It also describes the impact of loss on detecting quantum states of light and how this resultantly degrades measured of QNR.

3.1 Photodetection & Intensity Difference

To observe intensity difference squeezing, we introduce photodiodes and CCDs. These two devices differ in their operation and results, where photodiode observes a field by measuring its power, while a CCD detects photons by way of energy measurements. As such, both can be utilized in detecting photons and thus obtain intensity difference squeezing. Obviously, as we are attempting to measure the photon number of our EM fields, these devices are good candidates for doing so. Implementation of these detectors is depicted in Figure 3.1.

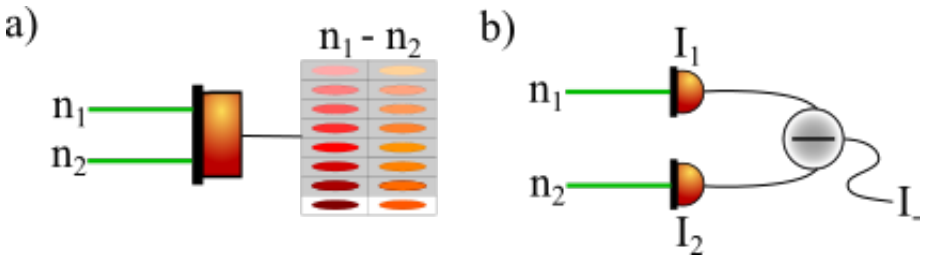

Figure 3.1: Photodetectors proposed in measuring the photon numbers of correlated EM fields. Diagram a) shows the use of a CCD, which captures images of the beams. After this, the intensities can be subtracted to obtain intensity difference squeezing. Diagram a) shows a balanced differential detector composed of two photodiodes, which converted the EM fields into photocurrents. These currents are then subtracted and fed into a spectrum analyser to observe intensity difference squeezing.

The operation of a CCD involves measuring light via capacitors, separated into "pixels", that detects photons when they cause that pixel to accumulate electrical charge. The charge on each capacitor is then read off via digitisation, converting the charges into digital data. As each pixel will detect a different part of the beam, the CCD provides spatial information on the transverse photon number distribution of each beam. Subtracting the beams allows correlated photons in similar locations of either beam to cancel out and results in a lower

noise for certain transverse modes of the beam profile, as will be seen in Chapter 6.

The operation of a photodiode converts intensities into photocurrents, using electrons to collect the intensity as a power. Detecting the signal fields with a photodiode each converts them into separate photocurrents. Arranged in a balanced differential detector, as in Figure 3.1, these photocurrents can then be subtracted, yielding an intensity difference photocurrent. Finally, this current can be fed into a spectrum analyser, where the noise of the intensity difference can be measured. Providing the fields of the detected intensities are correlated as in Section 2.3.3, the difference between the resultant photocurrents will be squeezed, measurable by the aforementioned spectrum analyser.

3.2 Homodyne Detection

To detect and observe quadrature squeezing, we need to realise the joint operators of Equations 2.36. To do so, we utilise beamsplitters, with correlated signals directed into either input. To this end, we return to EM field modes, specifically, longitudinal modes with either a single frequency, Single Mode states, or two frequencies, Two Mode states. Single and Two Mode states thus refers to the number of relevant wavevectors, $\mathbf{k}$, in such states. The correlated quadratures used in the above derivation, with subscripts $1, signal$ or $2, signal$, are Two Mode states with differing wavevectors. Conversely, the squeezed quadratures in Equations 2.36 (those achieving $e^{-s}/2$) are examples of Single Mode states, with wavevectors formed from a combination of input wavevectors.

Figure 3.2 shows how using a beamsplitter converts a Two Mode state into two Single Mode states. Specifically, four field quadratures, a pair for either wavevector of our signal fields, are transformed into two mixed fields, each containing some mixture of the signal field

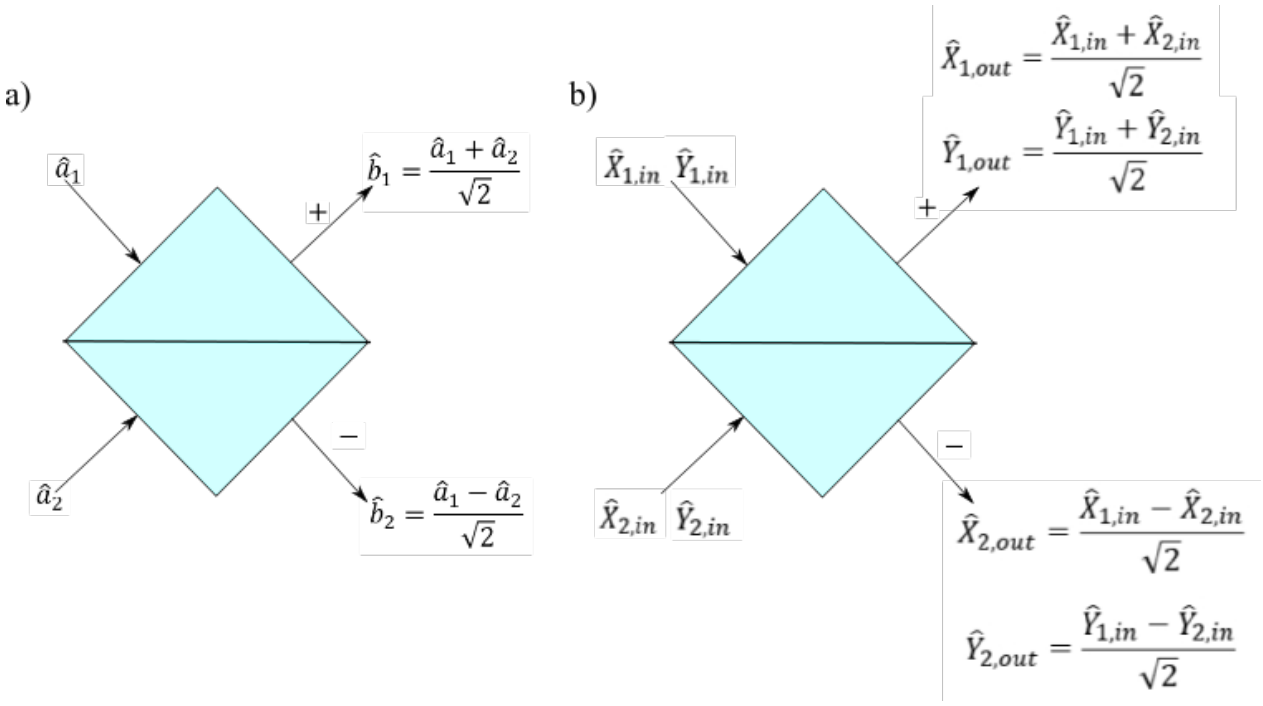

Figure 3.2: Input and output states from a 50:50 beamsplitter. Diagram a) shows the effect of the beamsplitter on the annihilation operator. Diagram b) shows the subsequent effect on the field quadrature operators.

quadratures. The resultant quadrature expressions are then as follows:

$$\begin{aligned} \hat{X}_{1,out} &= t\hat{X}_{1,in} + r\hat{X}_{2,in}, \\ \hat{Y}_{1,out} &= t\hat{Y}_{1,in} + r\hat{Y}_{2,in}, \\ \hat{X}_{2,out} &= t\hat{X}_{1,in} - r\hat{X}_{2,in}, \\ \hat{Y}_{2,out} &= t\hat{Y}_{1,in} - r\hat{Y}_{2,in}. \end{aligned} \tag{3.1}$$

Here r and t are the reflectivity and transmission coefficients of the beamsplitter. The change in sign between the two outputs, $1, out$ and $2, out$, occurs due to a phase change in reflected light, producing a phase difference of π between them. By conservation of energy, they can be seen to obey $t^2 + r^2 = 1$, with a 50:50 beamsplitter for example resulting in $r = t = 1/\sqrt{2}$. Directing the signal states output by our amplifier in the previous section into

this beamsplitter, and substituting $r = t = 1/\sqrt{2}$ into Equation 3.1, we find the following:

$$\begin{aligned}
\hat{X}_{1,out} &= \frac{\hat{X}_{1,in} + \hat{X}_{2,in}}{\sqrt{2}} \rightarrow \frac{\hat{X}_{1,signal} + \hat{X}_{2,signal}}{\sqrt{2}} = \hat{X}_{+,signal}, \\
\hat{Y}_{1,out} &= \frac{\hat{Y}_{1,in} + \hat{Y}_{2,in}}{\sqrt{2}} \rightarrow \frac{\hat{Y}_{1,signal} + \hat{Y}_{2,signal}}{\sqrt{2}} = \hat{Y}_{+,signal}, \\
\hat{X}_{2,out} &= \frac{\hat{X}_{1,in} - \hat{X}_{2,in}}{\sqrt{2}} \rightarrow \frac{\hat{X}_{1,signal} - \hat{X}_{2,signal}}{\sqrt{2}} = \hat{X}_{-,signal}, \\
\hat{Y}_{2,out} &= \frac{\hat{Y}_{1,in} - r\hat{Y}_{2,in}}{\sqrt{2}} \rightarrow \frac{\hat{Y}_{1,signal} - \hat{Y}_{2,signal}}{\sqrt{2}} = \hat{Y}_{-,signal}.
\end{aligned} \tag{3.2}$$

Thus directing the Two Mode state, $\hat{X}_{1,signal}$ and $\hat{X}_{2,signal}$, into two inputs of a beamsplitter results in new quadratures of two Single Mode states, $\hat{X}_{\pm}$. Moreover, Equations 3.2 also shows how the beamsplitter outputs are directly related to the sum and difference operators of Equations 2.35, and so shares the same noise properties, shown in Equation 2.36. Having defined how our theoretical method results in squeezing of our observables of interest, we now proceed to define how our detectors and optical system measure such squeezing.

To measure quadrature squeezing, we introduce homodyne detection, as a means of observing the quadratures. Homodyne detection requires a local oscillator (LO), a bright beam of similar frequency as the signal. This beam is mixed with the signal, with the phase between them determining which of the signal's quadratures is being measured and the beat frequency giving a measure of that quadrature's noise. For this detection scheme we utilize photodiodes and a beamsplitter, arranged into a balanced homodyne detector, as shown in Figure 3.3. This mixing results in a phase, ϕ_{LO}, being introduced on the LO, like so:

$$\begin{aligned}
\hat{X}_{\pm} &= \frac{\hat{X}_{-,out} \pm \hat{X}_{LO} e^{i\phi_{LO}}}{\sqrt{2}}, \\
\hat{Y}_{\pm} &= \frac{\hat{Y}_{-,out} \pm \hat{Y}_{LO} e^{i\phi_{LO}}}{\sqrt{2}}.
\end{aligned} \tag{3.3}$$

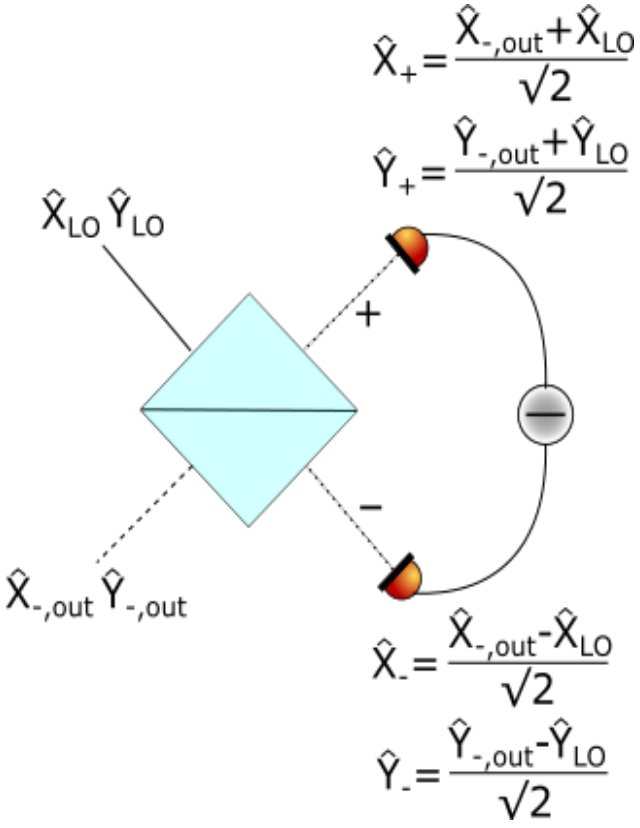

Figure 3.3: Balanced homodyne detection of mixed signal fields with field quadratures $\hat{X}_{-,out}$ and $\hat{Y}_{-,out}$ via a 50:50 beamsplitter.

Here $\hat{X}_\pm$ and $\hat{Y}_\pm$ are the quadratures exiting either output of the beamsplitter, $\hat{X}_{LO}$ and $\hat{Y}_{LO}$ are the LO quadratures and $\hat{X}_{-,out}$ and $\hat{Y}_{-,out}$ are field quadratures from the - output of a beamsplitter mixing two correlated signals. As these outputs are detected by photodiodes, they are converted to photocurrents, $\hat{\mathcal{I}}$, which is proportional to the intensity. This in turn is proportional to the electric field, which is dependent on X and Y, as shown in Equation 2.6. Thus, the photocurrent will depend on the quadratures:

$$\hat{\mathcal{I}}_\pm \propto \hat{I}_\pm \propto |\hat{E}_\pm|^2 \propto |\hat{X}_\pm + \hat{Y}_\pm|^2 \tag{3.4}$$

We then subtract these photocurrents and take the variance, substituting in Equations 3.3 to observe the fluctuation in quadrature, like so:

$$\begin{aligned}\mathrm{Var}(\hat{\mathcal{I}}_{\pm}-\hat{\mathcal{I}}_{\mp}) \propto \mathrm{Var}(|\hat{X}_{\pm}+\hat{Y}_{\pm}-\hat{X}_{\mp}-\hat{Y}_{\mp}|^2) \\ = \langle((|\hat{X}_{\pm}+\hat{Y}_{\pm}-\hat{X}_{\mp}-\hat{Y}_{\mp}|^2)^2\rangle - \langle|\hat{X}_{\pm}+\hat{Y}_{\pm}-\hat{X}_{\mp}-\hat{Y}_{\mp}|^2\rangle^2 \\ \approx|\beta|^2(e^{-2s}\cos^2(\phi_{LO})+e^{2s}\sin^2(\phi_{LO})) \\ \approx 4|\beta|^2(\mathrm{Var}(\hat{X}_{-,out})\cos^2(\phi_{LO})+\mathrm{Var}(\hat{Y}_{-,out})\sin^2(\phi_{LO}))\end{aligned} \tag{3.5}$$

Here β is the amplitude of the LO. Equation 3.5 is somewhat simplified, as we assume the square terms, $\hat{X}^2$, $\hat{Y}^2$, etc., are negligible due to their frequency being outside the bandwidth of the photodiode. Substituting the joint operators from Equations 2.35 into Equation 3.5, as in Equations 3.2, we can see that the photocurrent variance will clearly be determined by Equations 2.36, the variance of the joint operators. While the beamsplitter supplies both sum and subtraction joint operators, here the final result of Equation 3.5 is determined by our combination of the photocurrents, which in this case were subtracted.

This results in the variance of the subtraction joint operators appearing in Equation 3.5. Adding the photocurrents will change Equation 3.5 to depend on the sum joint operators $\hat{X}_{+,out}$ and $\hat{Y}_{+,out}$. Thus for non-zero squeezing parameter, $s > 0$, and an appropriate LO phase, $\cos(\phi_{LO}) = 1$ for $\hat{X}$ and $\sin(\phi_{LO}) = 1$ for $\hat{Y}$, we can see that the photocurrent variance in Equation 3.5 depends on the variance of the joint operators, which in turn determines the level of squeezing given the appropriate combination of photocurrents.

3.3 Losses in Detection Systems

As squeezing is dependent on the correlation between photons and fields within our amplified signals, losses in these signals intuitively results in loss of squeezing. To begin, we simplify our

initial state to a single squeezed state $|\xi\rangle$. We then consider the effect of detector efficiency on detecting a state, expressible by substituting $\sqrt{\eta_{det}}\hat{a}$ into Equations 2.27:

$$\langle \hat{I} \rangle \propto \eta_{det} \langle \hat{n} \rangle = \eta_{det} \langle \hat{a}^\dagger \hat{a} \rangle \tag{3.6}$$

This can be modelled as a combination of a beamsplitter with some efficiency, η_{det}, and a perfect detector. While a perfect detector will convert light into a photocurrent perfectly, an imperfect detector will fail to do so, losing some of the light. This loss is emulated by the beamsplitter, where one input is the desired light and the other is vacuum. This model is depicted in Figure 3.4.

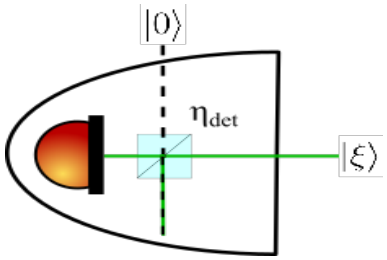

Figure 3.4: An imperfect detector (white) modelled as an ideal detector (orange) and a beamsplitter. The loss on the detector is emulated by the introduction of a beamsplitter. The solid green line represents the signal state, while the dashed black line represents the vacuum state.

Similarly we can use beamsplitters to model the effect of a lossy imaging system on the squeezed input state, $|\xi\rangle$. Such a system can be modelled as a series of beamsplitters (as adapted from [68]), where the jth component of the system has input states $|\xi_{j-1}\rangle$ and $|0\rangle$, an output state $|\xi_j\rangle$ and an output operator of the form $\hat{a}_j = \sqrt{\eta_j}\hat{a}_{j-1} + \sqrt{1-\eta_j}\hat{a}_v$. Here we have assumed that our beamsplitter model takes two inputs, one squeezed, $|\xi_{j-1}\rangle$, with eigenoperator $\hat{a}_{j-1}$, the other vacuum, $|0\rangle$, with eigenoperator $\hat{a}_v$ and the beamsplitter has

an efficiency η_j. This model is depicted in Figure 3.5.

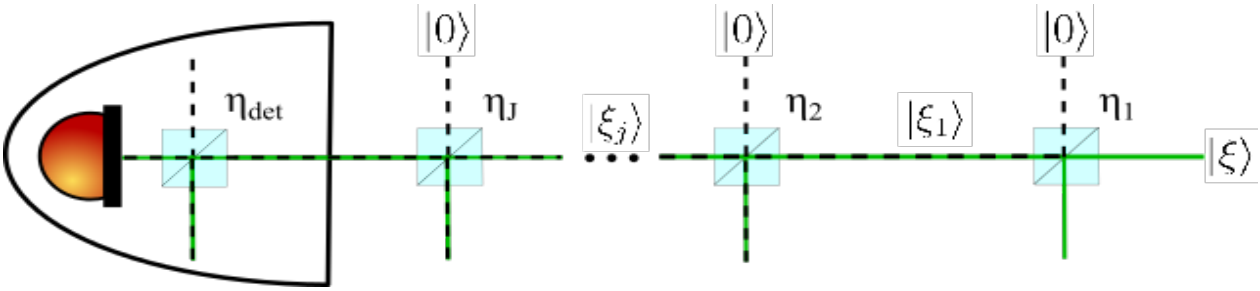

Figure 3.5: An imperfect optical system, with the loss at each component proportional to $1 - \eta_j$. The solid green line represents the signal state and the dashed black line represents the vacuum state.

Modelled as thus, for any system with J number of components, the jth component has efficiency, η_j. This induces loss in the input state of the jth component, $|\xi_{j-1}\rangle$, when the efficiency is less than ideal, $\eta_j < 1$. The resulting output is then a degraded squeezed state, $\hat{a}_j = \sqrt{\eta_j}\hat{a}_{j-1} + \sqrt{1-\eta_j}\hat{a}_v$. For simplicity, we assume there are no active components within our system, which allows us to combine the components' efficiencies into a single efficiency, $\eta_1 = \Pi_{j=1}^{J}\eta_j$. In doing so, we can also reduce our system to a single component, and the detected intensity becomes:

$$\langle \hat{I} \rangle \propto \eta_{det}\langle \hat{n}_1 \rangle = \eta_{det}\langle \hat{a}_1^\dagger \hat{a}_1 \rangle = \eta_{det}\eta_1 \langle \hat{a}_0^\dagger \hat{a}_0 \rangle. \tag{3.7}$$

Here $\hat{a}_0$ and $\hat{a}_1$ are the annihilation operators of the input state of the optical system and the output state of the optical system respectively. Thus $\langle \hat{a}_0^\dagger \hat{a}_0 \rangle = \langle \hat{n}_0 \rangle$ is the signal state's original average photon number, $\hat{n}_1$ is the signal's average photon number output from our system and η_1 represents the total efficiency of our system to retain light. The average of the

intensity, $\langle \hat{I} \rangle$, is obviously affected by this loss, as is the variance of the intensity, as follows:

$$\begin{aligned}
\langle \hat{n}_1 \rangle &= \langle \hat{a}_1^\dagger \hat{a}_1 \rangle = \eta_1 \langle \hat{a}_0^\dagger \hat{a}_0 \rangle = \eta_1 \langle \hat{n}_0 \rangle \\
\langle \hat{n}_1^2 \rangle &= \langle (\eta_1 \hat{a}_0^\dagger \hat{a}_0 + \sqrt{\eta_1(1-\eta_1)}(\hat{a}_0 \hat{a}_v + \hat{a}_v \hat{a}_0) + (1-\eta_1)\hat{a}_v^\dagger \hat{a}_v)^2 \rangle \\
&= \eta_1^2 \langle (\hat{a}_0^\dagger \hat{a}_0)^2 \rangle + \eta_1(1-\eta_1)\langle \hat{a}_0^\dagger \hat{a}_v \hat{a}_v^\dagger \hat{a}_0 + \hat{a}_v^\dagger \hat{a}_0 \hat{a}_0^\dagger \hat{a}_v \rangle \\
&= \eta_1^2 \langle (\hat{a}_0^\dagger \hat{a}_0)^2 \rangle + \eta_1(1-\eta_1)\langle \hat{a}_0^\dagger \hat{a}_0 \rangle
\end{aligned} \tag{3.8}$$

$$\begin{aligned}
\mathrm{Var}(\hat{I}_\mathcal{D}) \propto \mathrm{Var}(\hat{n}_1) &= \langle \hat{n}_1^2 \rangle - \langle \hat{n}_1 \rangle^2 = \\
&\eta_1^2 \langle (\hat{a}_0^\dagger \hat{a}_0)^2 \rangle + \eta_1(1-\eta_1)\langle \hat{a}_0^\dagger \hat{a}_0 \rangle - \eta_1^2 \langle \hat{a}_0^\dagger \hat{a}_0 \rangle^2 \\
&= \Delta \hat{n}_0^2 + \eta_1(1-\eta_1)\langle \hat{n}_0 \rangle.
\end{aligned} \tag{3.9}$$

Here $\hat{I}_\mathcal{D}$ is the degraded intensity, directed into our detector after passing through the optical system. Thus, referring back to our QNR expression, Equation 2.17, we can see that losses degrade the QNR of a squeezed state, resulting in the following:

$$\mathrm{QNR} = \frac{\mathrm{Var}(\hat{I}_\mathcal{D})}{\eta_1 \mathrm{Var}(\hat{I}_\mathcal{C})} = \frac{\mathrm{Var}(\hat{n}_0) + \eta_1(1-\eta_1)\langle \hat{n}_0 \rangle}{\eta_1 \Delta \hat{n}_0} = 1 + \eta_1 \left(\frac{\Delta \hat{n}_0^2}{\Delta \hat{n}_0} - 1 \right). \tag{3.10}$$

Compared to the QNR for a lossless system, where $\eta_1 = 1$ and Equation 3.10 becomes ${}^{\langle \mathrm{Var}(\hat{n}_0) \rangle}/_{\langle \Delta \hat{n}_0 \rangle}$, it becomes obvious that such losses introduce fluctuations that impairs the squeezed state and increases its noise. Though ideally we would want to reduce these losses to zero, it is not always possible, and in some cases unavoidable. For instance, in the case of coupling light into a waveguide with an efficiency $\eta < 1$, as in Section 5.

As such, we now observe the effect of loss on intensity difference squeezing by applying the results from Equation 3.9 to Equation 2.32. As shown in Figure 3.6, we take our two signal state outputs from our ideal amplifier, $\hat{n}_1$ and $\hat{n}_2$, and direct each through their own optical

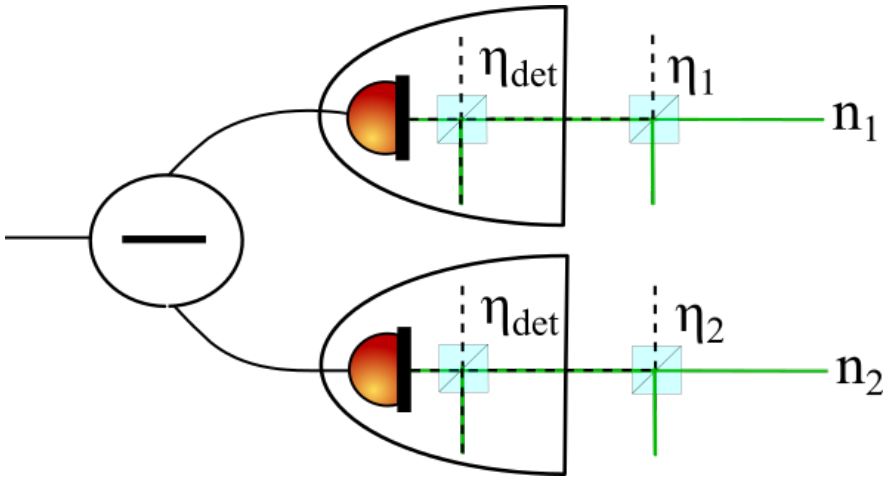

Figure 3.6: Simple optical system and differential detector system for the signals output from our ideal amplifier. The solid green lines represent the signal states, while the dashed black line represents the vacuum state.

system. Again, we simplify the efficiency of components in either beam path to the product of these efficiencies in said path. We then label them according to these beam paths, such that $\eta_1 = \Pi_{j=1}^{J}\eta_{1j}$ and $\eta_2 = \Pi_{j=1}^{J}\eta_{2j}$:

$$\mathrm{Var}(\hat{I}_{\mathcal{D}-}) \propto \mathrm{Var}(\hat{n}_1 - \hat{n}_2) =$$

$$\eta_1^2\mathrm{Var}(\hat{n}_1) + \eta_1(1-\eta_1)\langle\hat{n}_1\rangle + \eta_2^2\mathrm{Var}(\hat{n}_2) + \eta_2(1-\eta_2)\langle\hat{n}_2\rangle - 2\eta_1\eta_2\mathrm{cov}(\hat{n}_1, \hat{n}_2). \tag{3.11}$$

Here η_1 and η_2 are the efficiencies of the $\hat{n}_1$ and $\hat{n}_2$ signal paths respectively, and $\mathrm{cov}(\hat{n}_1, \hat{n}_2)$ is the covariance of these signals' photon number. The covariance is given as:

$$\mathrm{cov}(\hat{n}_1, \hat{n}_2) = \langle(\hat{n}_1 - \langle\hat{n}_1\rangle)(\hat{n}_2 - \langle\hat{n}_2\rangle)\rangle$$

From [68], we take the result of a derivation which can be found in Appendix C, which

re-expresses Equation 3.11 as a QNR value:

$$\frac{\mathrm{Var}(\hat{n}_1 - \hat{n}_2)}{\langle \hat{n} \rangle} = 2G^2(\eta_1 - \eta_2)^2 + G\eta_1(1 - 2\eta_1) + (G-1)\eta_2(1 - 2\eta_2) + 2G\eta_2(2\eta_1 - \eta_2) \quad (3.12)$$

Here G is the gain parameter of the intensity, as supplied by the amplifier generating the signal intensities in previous sections. Equation 3.12 thus shows how the resultant QNR clearly depends on the losses of either beam path. Given either of the efficiencies and the gain, the value of the other efficiency required to obtain a minimal QNR value is found by the following expressions (also from [68]):

$$\begin{aligned} \eta_1 &= \eta_2 - \frac{1}{4(G-1)}, \\ \eta_2 &= \eta_1 + \frac{1}{4(G-1)}. \end{aligned} \quad (3.13)$$

Equation 3.13 hence shows how the transmissions of these signals are not equivalent in their influence on the QNR. Thus minimising the QNR requires appropriate selection of the efficiencies of the signals' beam paths, while also considering the gain applied to both signals.

Thus, at the end of this chapter, we have established the expressions describing an EM field with specific longitudinal and transverse forms through the use of their wavevectors, $\mathbf{k}$. We have also covered how the amplification of these fields can lead to squeezing through correlations simultaneously attained from an appropriate amplifier. We have specified the our detector methodology and how it measures the squeezing, including the how losses can degrade such results. Having established these expressions, we now move on to observe how they can be physically achieved by an appropriate medium.

Chapter 4

Generation of Correlated Light via a Nonlinear Medium

In this chapter, we aim to realise the previously established squeezed EM fields via a physical medium. We begin with defining the specification required of a medium for it to be capable of amplifying and correlating such fields as laid out in the previous chapter. To achieve this, we introduce generic Nonlinear Optics, which pertains to the response of media to applied EM fields.

From there we will then tailor this description to the medium we have used in the experiments in Chapters 4 and 5, Rb85, and show how it provides the required amplification for the generation of squeezed states. Following this, we examine the specifics of using of Rb85 as an amplifying medium. This examination includes geometric properties of the set-up, which in turn influences the multimode character of amplified beams, as well as constraints on their interaction with the medium that introduces a phase-matching condition.

This chapter looks to derive an equation analogous to the ideal amplifier equation dervied from the previous section. In addition, it contains sections that detail expressions that

determine the optimal conditions under which this amplification work best. Here we will be utilising material adapted from [69], as well as [67] and [70].

4.1 Introductory Nonlinear Optics

Nonlinear optics encompasses phenomena caused by optical property changes in media due to the presence of light. How such changes affect the medium polarisation, that is, the dipole moment per unit volume, depends on electric permittivity, ϵ_0, the medium's susceptibility, $\chi^{(1)}$ and the form of the applied field, $E(t)$ as in [69]. It is expressed here as:

$$\boldsymbol{\mathcal{P}}(t) = \epsilon_0 \chi \mathbf{E}(t). \tag{4.1}$$

The exact form of the susceptibility also depends on both the medium's structure and the applied field(s), and in general is a tensor. For media with weak responses, the susceptibility is linear only, $\chi^{(1)}$, and for isotropic media it is reduced to a constant of proportionality. For stronger responses, the polarisation and susceptibility are expanded to a power series, resulting in:

$$\boldsymbol{\mathcal{P}}(t) = \epsilon_0 \left(\chi^{(1)} \mathbf{E}(t) + \chi^{(2)} \mathbf{E}^2(t) + \chi^{(3)} \mathbf{E}^3(t) ... \right). \tag{4.2}$$

This sum can also be written as:

$$\begin{aligned} \boldsymbol{\mathcal{P}} &= \boldsymbol{\mathcal{P}}^{(1)}(t) + \boldsymbol{\mathcal{P}}^{(2)}(t) + \boldsymbol{\mathcal{P}}^{(3)}(t) + ... \\ &= \boldsymbol{\mathcal{P}}^{(1)}(t) + \boldsymbol{\mathcal{P}}^{(NL)}(t) \end{aligned} \tag{4.3}$$

Here $\boldsymbol{\mathcal{P}}^{(NL)}(t)$ is the nonlinear response of the medium, though we reduce this sum further to $\boldsymbol{\mathcal{P}}^{(NL)}(t) = \boldsymbol{\mathcal{P}}^{(2)}(t) + \boldsymbol{\mathcal{P}}^{(3)}(t)$. This is because, in general, we are only concerned with $\boldsymbol{\mathcal{P}}^{(2)}(t)$ and $\boldsymbol{\mathcal{P}}^{(3)}(t)$, given that $\chi^{(2)}$ and $\chi^{(3)}$ bear special significance in describing a medium's

response to applied fields. Moreover, orders beyond these terms in the power series are negligible for the range of optical powers we intend to use. Verily, these first two nonlinear polarisations are zero or nonzero depending on the medium's structure. Second-order nonlinear optics only occurs in noncentrosymmetric media, which exhibit $\chi^{(2)}$ susceptibility, and so $\chi^{(2)}$ is non-zero only for those media. Conversely, third-order nonlinear optics, which involves media with $\chi^{(3)}$, applies regardless of the centrosymmetry.

4.1.1 Applied & Generated EM fields in Nonlinear Media

Both second- and third-order susceptibilities produce additional EM fields given conditions allowing for second- and third-order harmonic generation. In such conditions, the polarisation acts as a source of additional EM wave components, adding to applied fields, as can be seen when considering the wave equation:

$$\nabla^2\mathbf{E} - \frac{1}{c^2}\frac{\partial^2\mathbf{E}}{\partial t^2} = \frac{1}{\epsilon_0 c^2}\frac{\partial^2\boldsymbol{\mathcal{P}}}{\partial t^2}. \tag{4.4}$$

The polarisation, $\boldsymbol{\mathcal{P}}$, in Equation 4.4 can be substituted with Equation 4.3. The linear response of 4.3 can then be expressed as an index of refraction. Thus, in an isotropic medium, Equation 4.4 becomes:

$$\nabla^2\mathbf{E} - \frac{\varsigma^2}{c^2}\frac{\partial^2\mathbf{E}}{\partial t^2} = \frac{1}{\epsilon_0 c^2}\frac{\partial^2\boldsymbol{\mathcal{P}}^{NL}}{\partial t^2}. \tag{4.5}$$

Here ς is the refractive index and c is the speed of light. The term $\partial^2\boldsymbol{\mathcal{P}}^{NL}/\partial t^2$ is the acceleration of charges within the medium which generate EM radiation [69]. Thus the nonlinear polarisation term is capable of generating additional EM field components, which, under the right conditions, effectively act as an amplifier for applied EM fields. We intend to exploit this phenomenon as a realisation of the amplifier we introduced in Chapter 2.

As rubidium 85 (Rb85) was used in the experiments in this thesis, we note that such a medium is centrosymmetric, yielding $\chi^{(2)} = 0$. As such, we are left with a single non-negligible

nonlinear susceptibility, $\chi^{(3)}$, and its associated phenomena. The third-order polarisation is then given by:

$$\boldsymbol{\mathcal{P}}^{(3)}(t) = \epsilon_0 \chi^{(3)} \mathbf{E}^3 \tag{4.6}$$

Here the $\mathbf{E}^3$ term in Equation 4.6 is the cube of the summation of the applied EM fields, $\mathbf{E} = \sum_j \mathbf{E}_j$. When substituted into Equation 4.5, these fields should provide the form of the additional EM components generated by the rubidium as the applied fields pass through it, referred to as third-order harmonic generation.

In general, the forms of this third-order harmonic generation involves four frequencies, ν_1,ν_2,ν_3,ν_4, which combine in different ways to achieve differing phenomena. The typical combinations are $\nu_4 = \nu_1 + \nu_2 + \nu_3$ or $\nu_4 = \nu_1 + \nu_2 - \nu_3$, the distinction being the absorption of three frequencies and emission of the final frequency in the former, and the absorption of two frequencies and emission of the other two frequencies in the latter. These two phenomena are presented as simplified diagrams in Figure 4.1, in a) and b) respectively. Of the two $\chi^{(3)}$ phenomena in Figure 4.1, diagram b) has a transitions arrangement with two outputs. As such, this diagram is most similar to our ideal amplifier in Section 2.3. Obviously this phenomenon is idealised given its simplicity, but it suggests the appropriate kind of medium response for generating our desired correlated EM fields.

Here we specify the form of the EM fields comprising $\mathbf{E}$, recalling the seeds from Section 2.3, with fields E_1 and E_2, and introducing a third field, E_0. This third field is the pump, which supplies the amplifier medium with power to amplify the seeds. Our field $\mathbf{E}$ is then the summation of these fields and our nonlinear polarisation in Equation 4.3 is thus given by:

$$P^{(NL)}(t) = \epsilon_0 \chi^{(3)} (E_0 + E_1 + E_2)^3 \tag{4.7}$$

As E_0 powers the medium, we note that its field will be far larger than E_1 and E_2. Thus we consider only the terms in Equation 4.7 that include E_0^2. Additionally, we specify the forms

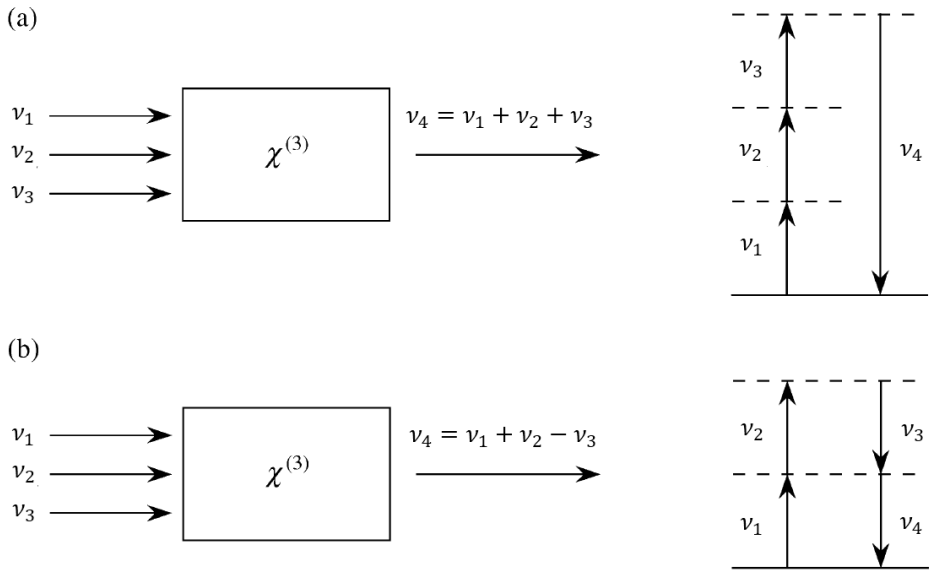

Figure 4.1: Two examples of third order harmonic generation. Diagram a) shows three fields interacting with a medium to produce a fourth field via absorption. Diagram b) shows three fields interacting with a medium to produce two fields of similar frequency via absorption and stimulated emission. Adapted from [69].

of these fields with complex notation, thus $E_j(t) = \underline{E}_j e^{-\nu_j t} + c.c.$, where $\underline{E}_j$ is a complex field amplitude. Expanding Equation 4.7, we find terms proportional to:

$$\underline{E}_0^2 \underline{E}_1^* e^{-i(2\nu_0 - \nu_1)t} + c.c., \tag{4.8}$$

$$\underline{E}_0^2 \underline{E}_2^* e^{-i(2\nu_0 - \nu_2)t} + c.c., \tag{4.9}$$

$$|\underline{E}_0|^2 \underline{E}_1^* e^{-i\nu_1 t} + c.c., \tag{4.10}$$

$$|\underline{E}_0|^2 \underline{E}_2^* e^{-i\nu_2 t} + c.c., \tag{4.11}$$

$$\underline{E}_0^2 \underline{E}_1 e^{-i(2\nu_0 + \nu_1)t} + c.c., \tag{4.12}$$

$$\underline{E}_0^2 \underline{E}_2 e^{-i(2\nu_0 + \nu_2)t} + c.c.. \tag{4.13}$$

Here Equations 4.8 and 4.9 refer to the process in Figure 4.1b), 4.10 and 4.11 are the cross-Kerr effects experienced by the seeds due to the pump while 4.12 and 4.13 are associated with the process shown in Figure 4.1a). As Figure 4.1b) corresponds to our process, Equations 4.8 and 4.9 give the form of the polarisation that acts as a source of EM fields.

Here we relabel the frequency subscripts of Figure 4.1b), setting ν_1 and ν_2 to the pump frequency, ν_0, ν_2 to ν_1 and ν_4 to ν_2. In doing this, the process described by Equations 4.8 and 4.9 now emits fields of the seed frequencies, with $2\nu_0 = \nu_1 + \nu_2$. Specifically, 4.8 produces EM fields of ν_2 and 4.9 produces EM fields of ν_1. Furthermore, this process produces these fields simultaneously, correlating them and fulfilling the requirements of the amplifier in Section 2.3.

4.1.2 Propagation & Correlation of EM fields via Polarisation

To observe the exact form of these generated fields, we now proceed to consider their spatial dependence by examining their propagation along z in Rb85. To do so, we use the slowly-varying envelope approximation, where $|{}^{\partial^2\underline{E}}/_{\partial z^2}| \ll |\mathbf{k}\cdot\underline{E}|$ and $|{}^{\partial^2\underline{E}}/_{\partial z^2}| \ll |\mathbf{k}\cdot{}^{\partial\underline{E}}/_{\partial z}|$, in steady state and a quasi-monochromatic field, $E(z,t) = \underline{E}(z)e^{ikz-\omega t}$. Thus, Equation 4.4 becomes:

$$\begin{aligned}
&\frac{\partial^2\underline{E}(z)e^{ikz-\omega t}}{\partial z^2} - \frac{1}{c^2}\frac{\partial^2\underline{E}(z)e^{ikz-\omega t}}{\partial t^2} = \frac{1}{\epsilon_0 c^2}\frac{\partial^2\underline{\mathcal{P}}(z)e^{-i\omega t}}{\partial t^2} \\
&\Rightarrow \frac{\partial}{\partial z}\left[\frac{\partial\underline{E}(z)}{\partial z}e^{ikz} + ik\underline{E}(z)e^{ikz}\right] + \frac{\omega^2}{c^2}\underline{E}(z) = -\frac{\omega^2}{\epsilon_0 c^2}\underline{\mathcal{P}}(z) \\
&\Rightarrow \frac{\partial^2\underline{E}(z)}{\partial z^2}e^{ikz} + 2ik\frac{\partial\underline{E}(z)e^{ikz}}{\partial z} - k^2\underline{E}(z)e^{-ikz} + \frac{\omega^2}{c^2}\underline{E}(z) = -\frac{\omega^2}{\epsilon_0 c^2}\underline{\mathcal{P}}(z) \\
&\Rightarrow \frac{\partial\underline{E}(z)}{\partial z} = -\frac{k^2}{2\epsilon_0}\underline{\mathcal{P}}(z)e^{-ikz}.
\end{aligned} \tag{4.14}$$

As stated, here we have used the slowly-varying envelope approximation and considered $\partial^2\underline{E}/\partial z^2$ to be negligible, and used $k = \omega c$ to simplify our derivation. Equation 4.14 hence

describes how the seed fields change as they propagate through our Rb85 medium. We can thus apply Equations 4.8 and 4.9 to observe how their propagation in nonlinear medium changes their fields:

$$\begin{aligned}\frac{\partial \underline{E}_1(z)}{\partial z} &= -\frac{k_1^2}{2}\chi^{(3)}\underline{E}_0^2\underline{E}_2^*(z)e^{-i(2k_0-k_2-k_1)z},\\ \frac{\partial \underline{E}_2(z)}{\partial z} &= -\frac{k_2^2}{2}\chi^{(3)}\underline{E}_0^2\underline{E}_1^*(z)e^{-i(2k_0-k_1-k_2)z}.\end{aligned} \tag{4.15}$$

We then assume that, given the strength of the pump, any depletion is negligible and it does not vary over the length of the medium. Addtionally, to maintain uniform amplification throughout the medium, the exponential term $e^{-i(2k_0-k_2-k_1)z}$ must be constant for all z. This can only be achieved through the phase-matching condition where $2k_0 - k_1 - k_2 = 0$. Taking $k \approx k_1 \approx k_2$ we then have solutions:

$$\begin{aligned}E_1(L) &= E_1(0)\cosh(s) + E_2^*(0)\sinh(s) = \sqrt{G}E_1(0) + \sqrt{G-1}E_2^*(0),\\ E_2(L) &= E_2(0)\cosh(s) + E_1^*(0)\sinh(s) = \sqrt{G}E_2(0) + \sqrt{G-1}E_1^*(0).\end{aligned} \tag{4.16}$$

Here the EM fields are entering the medium, at 0, and exiting it, at L, while s is the squeezing parameter from Chapter 2. Equations 4.16 have the same form as the correlated annihilation operators that were amplified by our ideal amplifier in Chapter 2. Quantising our applied fields will yield quantised versions of Equations 4.16, thus fully achieving the squeezing expressions from Chapter 2.

4.2 Rubidium Vapour as a Nonlinear Medium & Amplifier

In the previous section we established the use of nonlinear optics in our pursuit of correlated amplification of applied EM fields. In particular, we derived polarisations as medium responses

that generated EM fields of the same frequency as those applied to the medium. As we have specified Rb85 as our medium of choice, these expressions require adaptation to properly express both Rb85's response and the EM fields it generates. In this section, we will re-examine these expressions and show how Rb85 alters them, providing us with a more realistic result.

4.2.1 Generation of EM fields in Rubidium Vapour

Given that our proposed medium is a Rb85 gas, the polarisation will be given by an atomic transition that shares a frequency ν with an applied field of the same frequency. For this we refer to a methods by Lukin et al [71] and Turnbull et al [72]. This method involves solving the optical Bloch equation for a similar set-up as Figure 4.1b), although this approach considers the application of all four frequencies. Hence we consider a nonlinear medium with four fields applied to it. These fields include a strong pump and two weaker fields, referred to as probe, E_p, and conjugate, E_c, co-propagating along the z direction. The resultant polarisations are given as:

$$\begin{aligned} P(\omega_p) &= \epsilon_0(\chi_{pp}(\omega_p)E_p e^{ik_p z} + \chi_{pc}(\omega_p)E_c^* e^{i(2k_0-k_c)z}), \\ P(\omega_c) &= \epsilon_0(\chi_{cc}(\omega_c)E_c e^{ik_c z} + \chi_{cp}(\omega_c)E_p^* e^{i(2k_0-k_p)z}). \end{aligned} \tag{4.17}$$

Here the susceptibilities are labelled with respect to the relevant applied fields. The quantities χ_{pp} and χ_{cc} are the direct susceptibilities for the probe and conjugate, respectively. The quantities χ_{pc} and χ_{cp} are the cross susceptibilities for the probe and conjugate, and the conjugate and probe respectively. As before, our pump, E_0, is still significantly larger than our seeds, E_p and E_c. As such, the terms are expanded to all orders in E_0, but we have retained only the terms linear in E_p and E_c. Thus Equations 4.17 generalise Equations 4.8 and 4.9. Reporting them in Equations 4.14 now gives a more accurate pair of amplification

equations, which we will show still provide the amplifying behaviour we require to obtain squeezed light.

To proceed, we can simplify our derivation by an appropriate choice of frequency, which will remove the conjugate direct term $\chi_{cc}(\omega_c)$ from Equations 4.17. This choice of frequency, ω_c, can make the conjugate off-resonant with the medium, and so negate its direct term. We can also neglect $\Im(\chi_{pp})$ through the same selection, as this gives the optical absorption of the probe. However we cannot neglect its real component, which acts as a refractive index for the probe, $\varsigma_p = \Re(\chi_{pp}(\omega_p))$. Due to this, our equations are altered further, as the probe's wavevector is altered by this refractive index. Thus we must now consider effect of this refractive index on our equations for the generated fields.

4.2.2 Phase-Matching Condition of 4WM in Rubidium

As we have stated, most of the direct terms in Equation 4.17 can be neglected. However, due to the resonance of the probe with the medium, $\Re(\chi_{pp}(\omega_p))$ persists and must be factored into our expression to achieve amplification. As such, the refractive index experienced by the probe, $\varsigma_p = \Re(\chi_{pp}(\omega_p))$, induces a change in the probe wavevector, giving $\varsigma_p \mathbf{k}_p$. This resultantly alters the transitions within Rb85, with the resultant double-Λ transition shown in Figure 4.2.

In the previous section, we considered the probe and conjugate co-propagating, allowing us to assume they travelled along z. However, due to this change in probe refractive index, ς_p, and conservation of momentum, the probe and pump must co-propagate in slightly different directions. Taking this into account, we can factor this change into Equation 4.17, producing wave equations as follows:

$$\begin{aligned} \frac{\partial E_p(z)}{\partial z} &= \frac{ik_p}{2}\chi_{pc}(\omega_p)E_c^* e^{i\Delta\mathbf{k}\cdot\mathbf{r}}, \\ \frac{\partial E_c(z)}{\partial z} &= \frac{ik_c}{2}\chi_{cp}(\omega_c)E_p^* e^{i\Delta\mathbf{k}\cdot\mathbf{r}} \end{aligned} \tag{4.18}$$

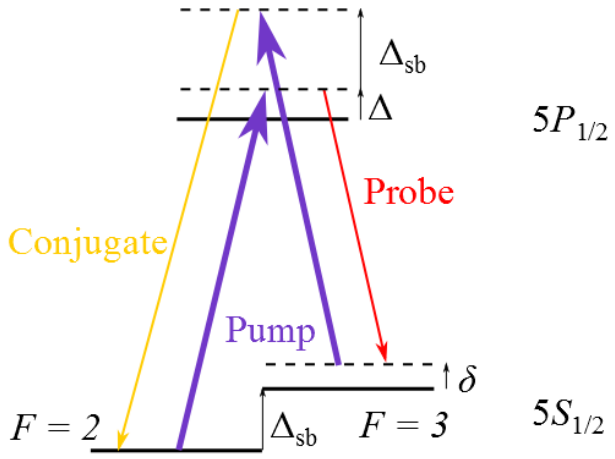

Figure 4.2: A detailed diagram of the 4WM double-Λ transition. Exact transitions frequencies can be found in [73]. The difference in probe and conjugate frequencies is of the order of 6GHz. Image taken from [67].

Here $\Delta\mathbf{k}$ is the geometric phase mismatch, given by $2\mathbf{k}_0 - \varsigma_p\mathbf{k}_p - \mathbf{k}_c$. This resultantly changes the nature of the amplification, as now the wavevectors must "match" in order for Equations 4.18 to exhibit amplification. The resulting change to the wavevectors is shown in Figure 4.3. Thus to achieve optimal amplification, we must reduce the phase mismatch between the wavevectors to 0, $\Delta\mathbf{k} = 0$. This reduces Equations 4.18 to:

$$\begin{aligned} \frac{\partial E_p(z)}{\partial z} &= \frac{ik_p}{2}\chi_{pc}(\omega_p)E_c^*, \\ \frac{\partial E_c(z)}{\partial z} &= \frac{ik_c}{2}\chi_{cp}(\omega_c)E_p^* \end{aligned} \tag{4.19}$$

Taking into account the 4WM process, Equations 4.19 can then be simplified by $\chi_{cp}(\omega_c) = \chi_{pc}(\omega_p)^\dagger$. Additionally, we can make the substitution $s/L = \chi_{pc}(\omega_p)ik_p/2 = \chi_{cp}^\dagger(\omega_c)ik_c/2$, where s is the squeezing parameter from Chapter 2, and L is the length of the medium. As such, our equations for applied fields propagation through our Rb85 medium become:

$$\begin{aligned} \frac{\partial E_p}{\partial z} &= \frac{s}{L}E_c^*, \\ \frac{\partial E_c}{\partial z} &= \frac{s}{L}E_p^* \end{aligned} \tag{4.20}$$

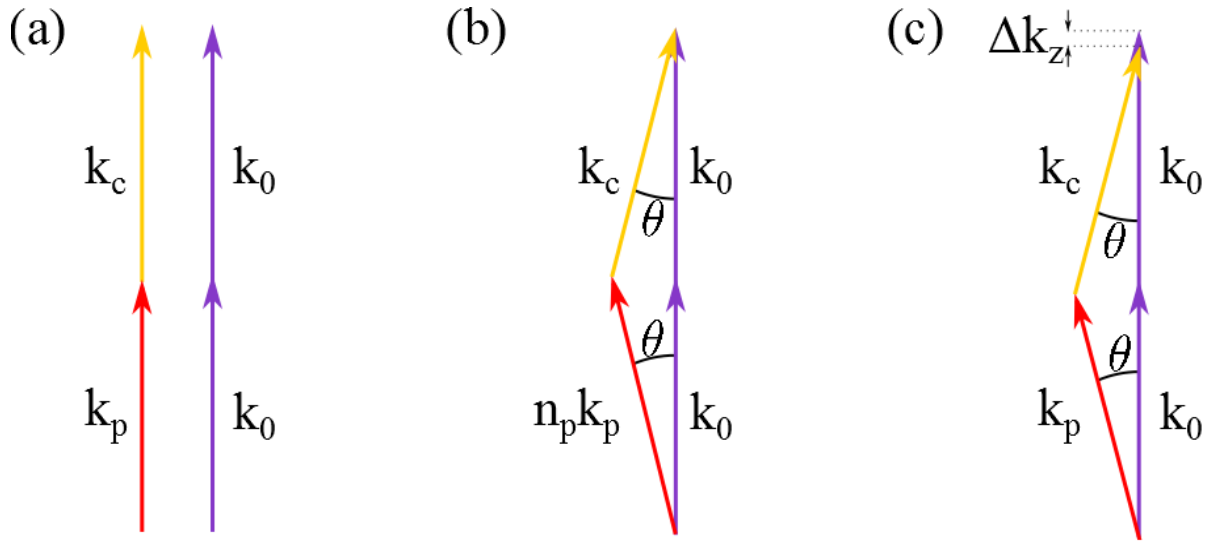

Figure 4.3: Instances of phase-matching in a) free space, b) Rb85 and c) Rb85 while considering the geometric phase mismatch. Taken from [67].

Given input EM fields, $E_p(\mathbf{r}_0)$ and $E_c(\mathbf{r}_0)$, at the start of the cell, $\mathbf{r}_0 = (x, y, 0)$, Equations 4.20 are then solved as follows:

$$\begin{aligned} E_p(\mathbf{r}_L) &= \cosh(s)E_p(\mathbf{r}_0) + \sinh(s)E_c^*(\mathbf{r}_0), \\ E_c(\mathbf{r}_L) &= \cosh(s)E_c(\mathbf{r}_0) + \sinh(s)E_p^*(\mathbf{r}_0). \end{aligned} \tag{4.21}$$

Here $\mathbf{r}_L = (x, y, L)$, denoting the output of the cell. Thus for a zero phase mismtach, Equations 4.21 resemble the equations of optical amplification we derived in Section 2.3.1. As such it governs the behaviour of this amplification and correlates the two fields. This corresponds to the same behaviour we established in Chapter 2, which implies that these same equations are capable of yielding squeezing.

4.3 Propagation of Correlated EM fields

Though the derivation of the EM fields in Section 4.2 provides the desired correlated behaviour, there are a number of additional related phenomena that influence the 4WM process. These include the coherence area arising from imaging limitations and correlation locations within the transverse beam profile in the near and far fields. These pertain to the nature of the beams' propagation throughout and out of the Rb85 medium, and how the correlations are resultantly affected.

4.3.1 Beam Propagation & Coherence Length

In addition to the phase-matching condition, the beams also encounters further issues propagating the length of the cell, stemming from diffraction limitations and mode overlap. The issue of mode overlap occurs when considering propagation of a Gaussian beam. Gaussian beams are beams of light with a 2D intensity profile proportional to a Gaussian function:

$$I(x,y) = Ae^{-\left(\frac{(x-x_0)^2}{2\sigma_x^2}+\frac{(y-y_0)^2}{2\sigma_y^2}\right)}.$$

Here x and y are the coordinates spanning the beam profile, x_0 and y_0 are the coordinates of the centre of the beam and σ_x and σ_y are the standard deviations of the beam profile in the x and y directions respectively. Conventionally, the propagation of a Gaussian beam is observed by tracing the $1/e^2$ radius. In particular, we refer to the smallest radius of the beam along its propagation as its beam waist, w_0. This waist is given by the following expression:

$$w_0 = \sqrt{\frac{z_R\lambda}{\varsigma\pi}}. \tag{4.22}$$

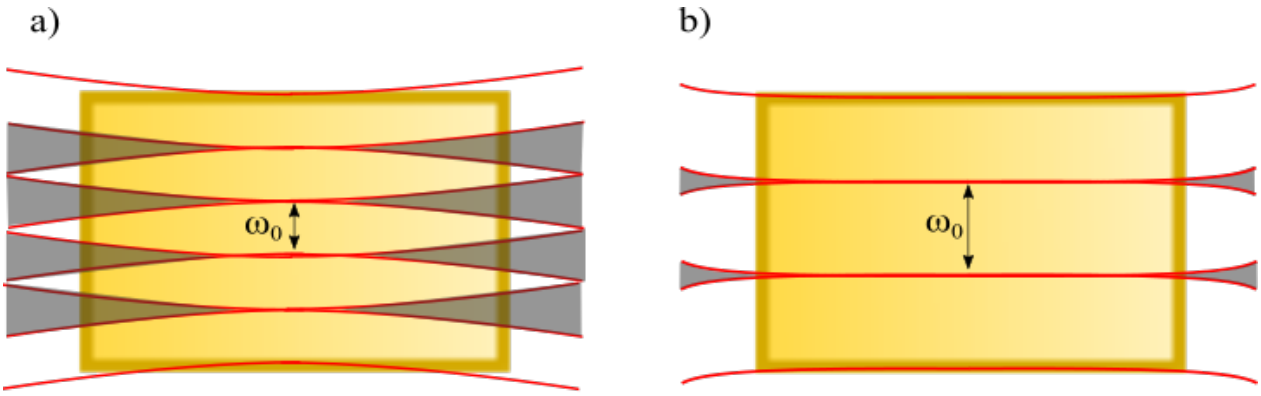

Figure 4.4: Mode overlapping in the Rb85 cell, with the mode overlap shown as shaded areas. Diagram a) shows the issues of having a small beam waist, as the beams will expand quicker and increase the size of the shaded areas. Diagram b) shows how larger beam waists suffer less of this problem.

Here z_R is the Rayleigh length of the beam, ς is the refractive index and λ is the light's wavelength in vacuum. The Rayleigh length is the propagation distance from the beam waist to where the beam radius, w, expands to $\sqrt{2}w_0$. This is evident from the expression for the $1/e^2$ radius of a Gaussian beam during propagation:

$$w(z) = w_0\sqrt{1 + \left(\frac{z}{z_R}\right)^2}. \tag{4.23}$$

When substituting in the Rayleigh length, z_R for the propagation from the beam waist, z, we observe how the beam expands to a width of $\sqrt{2}w_0$, as stated previously. Hence Equation 4.22 shows that a smaller beam waist requires a shorter Rayleigh length. Additionally, Equation 4.23 shows that smaller Rayleigh lengths result in larger beam radii when propagating away from the waist. This causes issues with mode overlap within the Rb85 medium as the beam passes through, which is worsened with smaller waists, as shown in Figure 4.4.
This figure shows how the same modes within the beams' decomposition can couple together.

Hence we note this behaviour and use it to impose a criterion on our beam: to avoid mode overlap as much as possible, we set the Rayleigh length of our beam equal to length of our cell, such as in Figure 4.5.

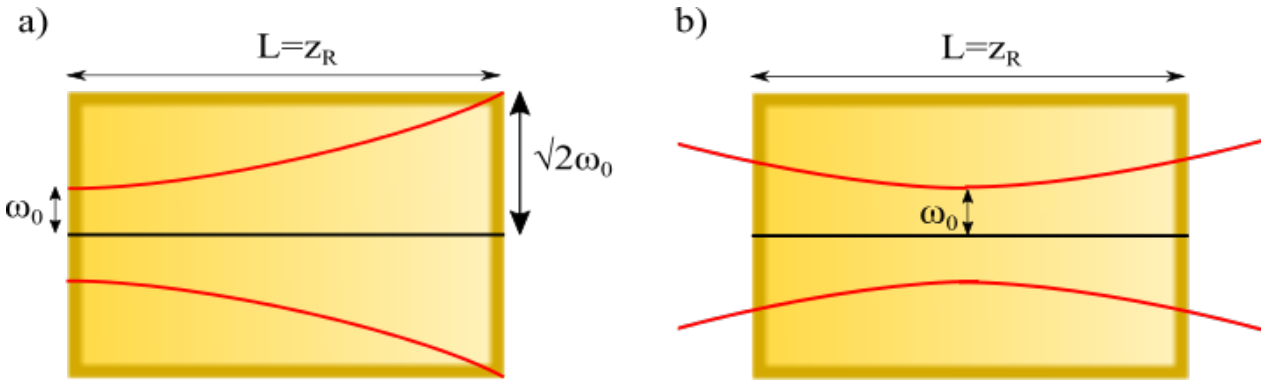

Figure 4.5: Propagation of a Gaussian beam through a vapour cell of length L. The smallest feasible mode without excess diffraction is then considered to be the waist of a Gaussian beam with a Rayleigh length, z_R, equivalent to the length of the cell. Diagram a) shows this imposed on the system. Diagram b) shows how, moving the waist to the center of the cell, this criteria approximately collimates the beam throughout the cell.

Given this condition, placing the beam waist at the centre of our cell will ensure that the beam width will not exceed $\sqrt{2}w_0$ over the length of the cell. This will ensure that the beam remains fairly collimated throughout the cell, and avoid mode coupling. Returning to Equation 4.22 and substituting L for z_R and rearranging, we obtain:

$$w_0 = \sqrt{\frac{z_R\lambda}{\varsigma\pi}} \rightarrow \sqrt{\frac{L\lambda}{\varsigma\pi}} = l_{coh}$$

$$l_{coh} = \sqrt{\frac{L\lambda}{\varsigma\pi}} \tag{4.24}$$

This result is referred to as the coherence length, l_{coh}, and sets a minimum area of uncertainty in turn referred to as the coherence area. Hence the correlated photons in our beams cannot be

resolved beneath this limit, thus randomly distributing them within this area. In addition, Lopez et al. also theoretically derived this limit [74]. Further to this, we can obtain the number of spatial modes the cell can support by considering the size of the pump:

$$N = \frac{w_{P0}^2}{l_{coh}^2} \tag{4.25}$$

Here N is the number of modes and w_{P0} is the pump waist size. This places a physical limit on how we can decompose the transverse profile of our beams. This in turn dictates how the resolution of our correlations depends on the waist size of the pump. For our purposes, this will affect the size of the region we can squeeze, and where in our decomposition of the beam we will find it.

4.3.2 Near & Far Field Correlations

After examining the propagation of light through our medium, we now look at its propagation out of our medium. As shown in previous sections, the use of Rb85 amplifies our signals such that they display correlations, which are spatially localised subject to diffraction. The position of these correlations is significant, as our method of squeezing requires subtracting them to cancel their noise and achieve noise reduction.

To consider the effect of diffraction on the propagation out of the medium, we consider two main locations: the near field (located inside the medium) and the far field (located approximately an infinite distance away from the medium). We then proceed by introducing the Fresnel diffraction integral, adapted from [75] as:

$$E(\mathcal{X},\mathcal{Y},z+\Delta z) = -i\frac{e^{ik\frac{\Delta z+(\mathcal{X}^2+\mathcal{Y}^2)}{2\Delta z}}}{\lambda\Delta z}\iint_{-\infty}^{\infty}\left\{E(x,y,z)e^{ik\frac{x^2+y^2}{2\Delta z}}\right\}e^{-ik\frac{x\mathcal{X}+y\mathcal{Y}}{\Delta z}}dxdy. \tag{4.26}$$

Here $E(x, y, z)$ is the field of a beam with transverse profile in the plane xy at point z along its propagation. For simplicity, we place this z axis through the centre of the xy plane, which is placed at the centre of the medium such that z then runs the length of the medium. We then consider the transverse beam profile at two planes, xy at a point z within the medium and $\mathcal{X}\mathcal{Y}$ at another point $z + \Delta z$, a distance Δz away from the xy plane. By changing Δz, we can observe the beam in the near or far field, depending on how large Δz is. As we are concerned with observing the propagation out of the medium, we are interested in the far field. For this, we consider the Fraunhofer approximation:

$$\Delta z \gg \frac{W(x, y)k}{2}. \tag{4.27}$$

Here $W(x, y)$ is the area of the beam in the near field, whatever its shape, and k its wavenumber. This approximation is the requirement for the beam to enter a region of Fraunhofer diffraction, which is considered to be the far field. Thus taking z to sufficiently large values, we find that the phase factor, $e^{ik\frac{\Delta z+(\mathcal{X}^2+\mathcal{Y}^2)}{2\Delta z}}/\lambda\Delta z$, in Equation 4.26 reduces to unity over the xy plane. This reduces Equation 4.26 to:

$$E(\mathcal{X}, \mathcal{Y}, z + \Delta z) = -i \iint_{-\infty}^{\infty} E(x, y, z) e^{-ik\frac{x\mathcal{X}+y\mathcal{Y}}{\Delta z}} dxdy. \tag{4.28}$$

Equation 4.28 hence shows that the far field is a Fourier Transform of the near field. This is the classical result however, and to make it relevant to our discussion, we instead observe how the near and far field affects our observables of interest, $\hat{a}$, $\hat{X}$ and $\hat{Y}$, as shown in [76]. More specifically, we use near and far field quadrature operators, $\hat{X}$ and $\hat{Y}$, to derive a Fourier transform for their joint operators, $\hat{X}_-$ and $\hat{Y}_+$, to show how the joint operators differ between the near and far field. We firstly consider the near field, recalling Equations 2.6 and its relevant operators of similar form to Equations 2.11, while also considering their

frequency dependency as derived in Appendix A:

$$\begin{aligned} \hat{X}(\boldsymbol{\rho}, \Omega) &= \frac{\hat{a}^\dagger(\boldsymbol{\rho}, \Omega) + \hat{a}(\boldsymbol{\rho}, \Omega)}{2}, \\ \hat{Y}(\boldsymbol{\rho}, \Omega) &= \frac{i(\hat{a}^\dagger(\boldsymbol{\rho}, \Omega) - \hat{a}(\boldsymbol{\rho}, \Omega))}{2}. \end{aligned} \tag{4.29}$$

Here $\boldsymbol{\rho}$= (x, y) is a point in the near field, which we have defined as the xy plane located in the medium, while Ω is the half the difference between the probe and conjugate frequencies. Thus $\pm\Omega$ is the midpoint plus or minus half of the frequency difference between probe and conjugate, referring to either the probe or conjugate frequency depending on the sign. We then consider the EM field in the far field, as in Equation 4.29, and its quadrature operators:

$$\begin{aligned} \hat{X}(\mathbf{k}, \Omega) &= \frac{\hat{a}^\dagger(\mathbf{k}, \Omega) + \hat{a}(\mathbf{k}, \Omega)}{2}, \\ \hat{Y}(\mathbf{k}, \Omega) &= \frac{i(\hat{a}^\dagger(\mathbf{k}, \Omega) - \hat{a}(\mathbf{k}, \Omega))}{2}. \end{aligned} \tag{4.30}$$

Here $\mathbf{k}$= $(\mathcal{X}, \mathcal{Y})$ is a point in the far field, which we have defined as the $\mathcal{XY}$ plane located Δz away from the near field. Unsurprisingly, we note that $\hat{a}(\mathbf{k}, \Omega)$ is the Fourier transform of $\hat{a}(\boldsymbol{\rho}, \Omega)$, and in addition, $\hat{a}^\dagger(\mathbf{k}, \Omega)$ can also be seen to be the Fourier transform of $\hat{a}(-\boldsymbol{\rho}, \Omega)$. However, due to this, $\hat{X}(\mathbf{k}, \Omega)$ is not the Fourier transform of $\hat{X}(\boldsymbol{\rho}, \Omega)$, which means that our joint operators from Equations 2.35, $\hat{X}_-$, $\hat{Y}_+$, cannot be directly transformed from near to far field. To establish this transformation properly, we first consider the joint operators in the near field:

$$\begin{aligned} \hat{X}_-(\boldsymbol{\rho}, \Omega) &= \frac{\hat{X}(\boldsymbol{\rho}, \Omega) - \hat{X}(\boldsymbol{\rho}, -\Omega)}{\sqrt{2}}, \\ \hat{Y}_+(\boldsymbol{\rho}, \Omega) &= \frac{\hat{Y}(\boldsymbol{\rho}, \Omega) + \hat{Y}(\boldsymbol{\rho}, -\Omega)}{\sqrt{2}}. \end{aligned} \tag{4.31}$$

Here Equations 4.31 are the two joint operators from Equations 2.35 that produce squeezing. The notation has been changed from subscripts to frequencies, with Ω and $-\Omega$ denoting

probe and conjugate frequency respectively. To find the relation between the near and far field operators, and thus observe the behaviour of the correlations, we consider the far field operators, $\hat{X}_-(\mathbf{k},\Omega)$ and $\hat{Y}_+(\mathbf{k},\Omega)$, and work backwards to derive to find their dependence on the near field joint operators, $\hat{X}_-(\boldsymbol{\rho},\Omega)$ and $\hat{Y}_+(\boldsymbol{\rho},\Omega)$:

$$\begin{aligned}
\hat{X}_-(\mathbf{k},\Omega) &= \frac{\hat{X}(\mathbf{k},\Omega) - \hat{X}(-\mathbf{k},-\Omega)}{\sqrt{2}} \\
&= \frac{\hat{a}^\dagger(\mathbf{k},\Omega) + \hat{a}(\mathbf{k},\Omega) - \hat{a}^\dagger(-\mathbf{k},-\Omega) + \hat{a}(-\mathbf{k},-\Omega)}{2\sqrt{2}} \\
&= \frac{\mathcal{F}(\hat{a}^\dagger(-\boldsymbol{\rho},\Omega) + \hat{a}(\boldsymbol{\rho},\Omega) - \hat{a}^\dagger(\boldsymbol{\rho},-\Omega) - \hat{a}(-\boldsymbol{\rho},-\Omega))}{2\sqrt{2}} \\
&= \frac{\mathcal{F}(\hat{X}_-(\boldsymbol{\rho},\Omega) + \hat{X}_-(-\boldsymbol{\rho},\Omega))}{2\sqrt{2}},
\end{aligned} \tag{4.32}$$

$$\begin{aligned}
\hat{Y}_+(\mathbf{k},\Omega) &= \frac{\hat{Y}(\mathbf{k},\Omega) + \hat{Y}(-\mathbf{k},-\Omega)}{\sqrt{2}} \\
&= \frac{i(\hat{a}^\dagger(\mathbf{k},\Omega) - \hat{a}(\mathbf{k},\Omega) + \hat{a}^\dagger(-\mathbf{k},-\Omega) - \hat{a}(-\mathbf{k},-\Omega))}{2\sqrt{2}} \\
&= \frac{\mathcal{F}(i(\hat{a}^\dagger(-\boldsymbol{\rho},\Omega) - \hat{a}(\boldsymbol{\rho},\Omega) + \hat{a}^\dagger(\boldsymbol{\rho},-\Omega) - \hat{a}(-\boldsymbol{\rho},-\Omega)))}{2\sqrt{2}} \\
&= \frac{\mathcal{F}(\hat{Y}_+(\boldsymbol{\rho},\Omega) - \hat{Y}_+(-\boldsymbol{\rho},\Omega))}{2\sqrt{2}}.
\end{aligned} \tag{4.33}$$

Equations 4.32 and 4.33 show that a joint quadrature, i.e. $\hat{X}_-(\mathbf{k},\Omega)$, of symmetric locations in the far field, $\mathbf{k}$ and $-\mathbf{k}$, is given by the Fourier transform of two joint quadratures, i.e. $\hat{X}_-(\boldsymbol{\rho},\Omega) + \hat{X}_-(-\boldsymbol{\rho},\Omega)$, taken at identical locations, $\boldsymbol{\rho}$ or $-\boldsymbol{\rho}$, in the near field. Resultantly, if the near field joint operators, i.e. $\hat{X}_-(\boldsymbol{\rho},\Omega)$, are squeezed for all $\boldsymbol{\rho}$, then the far field joint operators must be squeezed for all $\mathbf{k}$. As such, the probe and conjugate beams must be correlated across all $\boldsymbol{\rho}$ in the near field, and be entangled between $\mathbf{k}$ in the probe and $-\mathbf{k}$ in the conjugate for all $\mathbf{k}$ in the far field.

This same phenomena corresponds to the conservation of momentum, which stems from

the phase-matching condition. From Section 4.3, we saw that avoiding mode overlap in the medium would require compromise on the resolution of our beam. This results in our correlated points, $\boldsymbol{\rho}$ and $\mathbf{k}$, representing areas as opposed to positions. Thus, Equations 4.32 and 4.33 express the shared noise behaviour between certain regions in the far field. This is shown diagrammatically in Figure 4.6.

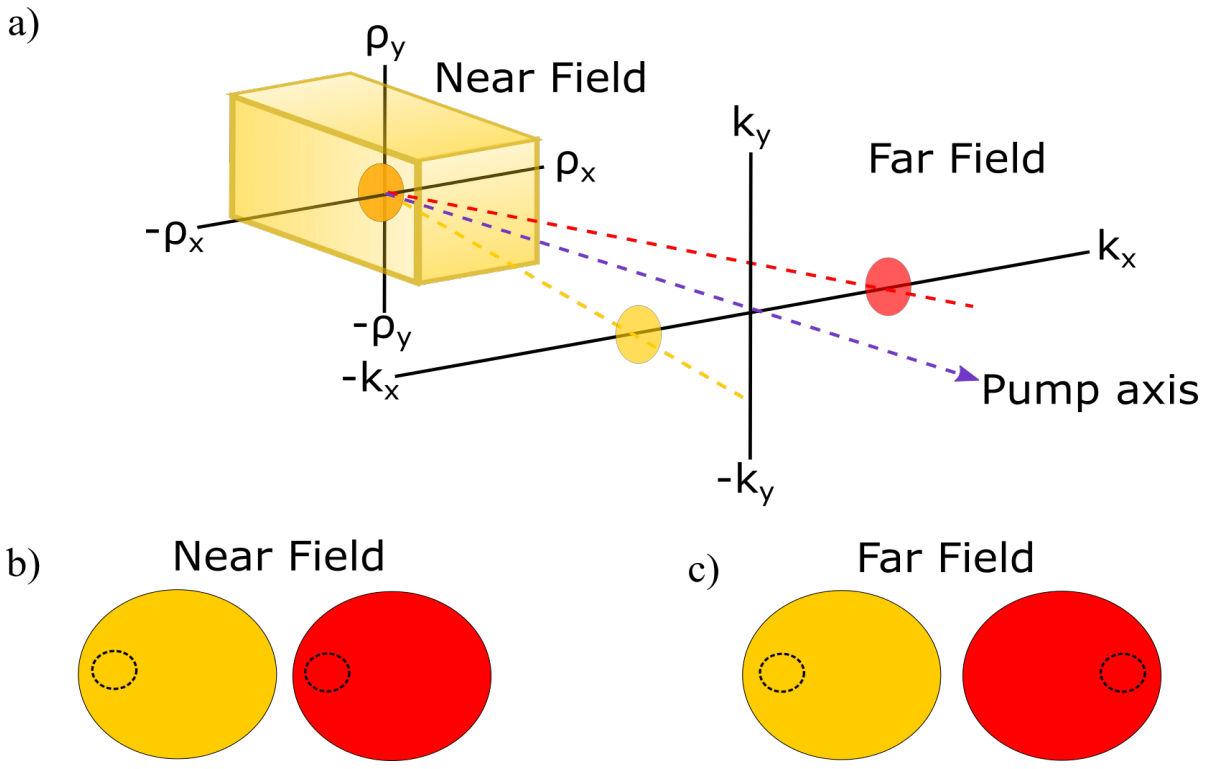

Figure 4.6: A set of diagrams displaying the near and far field and the difference in location of correlations between near and far field beams, where red denotes probe and orange denotes conjugate. Diagram a) shows the overlapped beams in the centre of the medium, where correlated photons are generated, and the separated beams in the far field. The $\boldsymbol{\rho}$ and $\mathbf{k}$ axes are coordinate systems for the near and far field respectively. Diagram b) shows how the photon correlations would be confined to the same area in either beam when in the near field. Diagram c) shows how the photon correlations are located in regions that are conjugate to each other when in the far field.

In general, when detecting the beams, this minimum area of uncertainty is not too much of an issue, given that integrating the beam profiles and subsequent subtraction will still yield squeezing. However, in MSM intensity difference measurements, the location of photons and their correlations is important and imaging becomes paramount. Hence the beams must be in the same field and the relevant regions must be subtracted to observe MSM squeezing. Additionally, these signal beams are not the only correlated fields to exit the cell. Just as we showed that vacuum can be squeezed in Section 2.3.2, any and all vacuum modes that satisfy the phase-matching condition will consequently be correlated in a similar manner. This results in a cone of correlation exiting the cell, as shown in Figure 4.7.

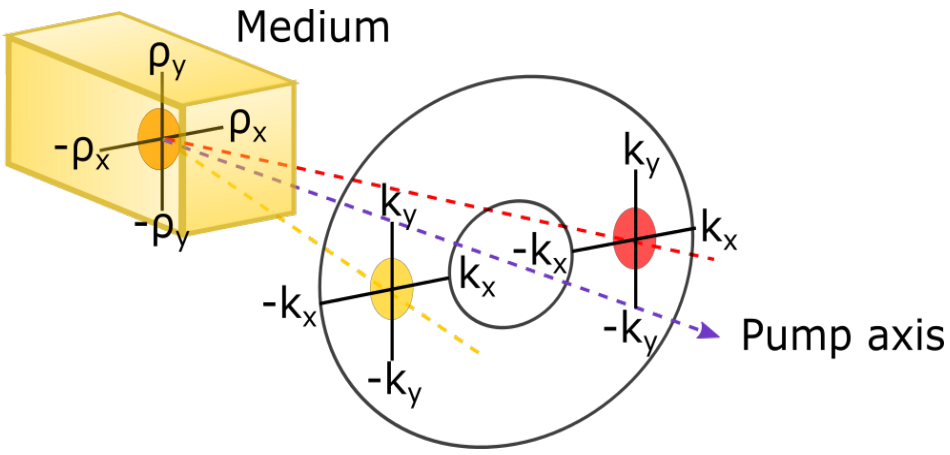

Figure 4.7: The correlated fields output from the Rb85 Medium, which results in an annulus of correlated vacuum modes, including the two signal beams. Here we consider the local position of correlations in the far field of either signal beam. In the far field, we also consider the spatial frequencies of the beams separately.

This is of particular relevance to the vacuum surrounding the signal beams in MSM measurements, as in the far field these squeezed vacuum states are associated with the high-spatial-frequency fluctuations of the beam in the near field. For this reason, it is optimal to angle the signals such that they are halfway between the outer and inner boundaries of

this annulus, ensuring an equal and corresponding amount of near field spatial frequencies on either side of each beam. As such, preserving this vacuum is paramount to ensuring that the correlations between the signal beams is maintained in both the near and far field.

Chapter 5

Experimental Set-up and Preliminary Experiments

In this chapter we examine the basic structure of the experimental set-up, and consider results from the first two of the three experiments presented in this thesis, the BLO and conduit experiments. This basic structure of all three experiments is based on the prior chapters' theory, using probe and conjugate signal beams amplified by a Rb85 atomic vapour to obtain squeezing.

The detection of these probe and conjugate signals in each experiment differed however. The first experiment used homodyne detection with an LO composed of two colours, called the BLO, to solve solve detection issues caused by the frequency difference between the probe and conjugate when observing quadrature squeezing (the BLO experiment). The second experiment used continuous photodetection via a balanced photodetector to observe conservation of spatial quantum correlations after passing the probe though a multimode waveguide (the conduit experiment). The third and final experiment used pulsed photodetection to measure intensity difference squeezing via CCD camera (the camera experiment).

The following section examines the similarities between the three experiments, mainly the fundamental system used in 4WM and common components in it's operation.
This chapter contains the results of the BLO experiment in Section 5.2 and the results of the conduit experiment in Section 5.3. The BLO results show that squeezing persists across a considerable bandwidth when altering the frequency of the probe seed. This indicates that the double-Λ transition accepts and spans a range of probe and conjugate frequencies. The results of the conduit experiment show that multi-spatial mode squeezing in the near field can be detected, even when transmitted through a waveguide.

5.1 Overview of Experiments

The laser used in these experiments was a M-Squared Titanium-Sapphire (Ti:Sapph) laser, emitting around $\sim$3W in each of the experiments, itself pumped by a 532nm Coherent V12 (Verdi) laser powered at 11W. The Ti:Sapph was controlled and monitored through a laptop using M-Squared SolsTis software with a M-Squared ICE Bloc connecting the two. It was locked to a wavelength of 794.974nm.
Both lasers required temperature cooling and stabilisation, which was achieved using a Coherent laser cooling system set to cool to and stabilise at 18.00°C, via a closed loop system. This closed loop involved malleable plastic piping and was first fed into a port on the side of the Ti:Sapph. A second port then allowed the coolant to pass out of the Ti:Sapph and into the Verdi, which also had two ports, the second of which was an output that fed the coolant back into the cooler. The coolant itself was originally distilled water mixed with pipe cleanser, though later changed to a mix of $\sim$95% distilled water and $\sim$5% alcohol.
The Ti:Sapph output laser beam was then divided between two preparation areas using a polarising beamsplitter, with one output used as the probe beam and the other for the pump beam, as shown in Figure 5.1. The probe preparation area contained an AOM double-pass

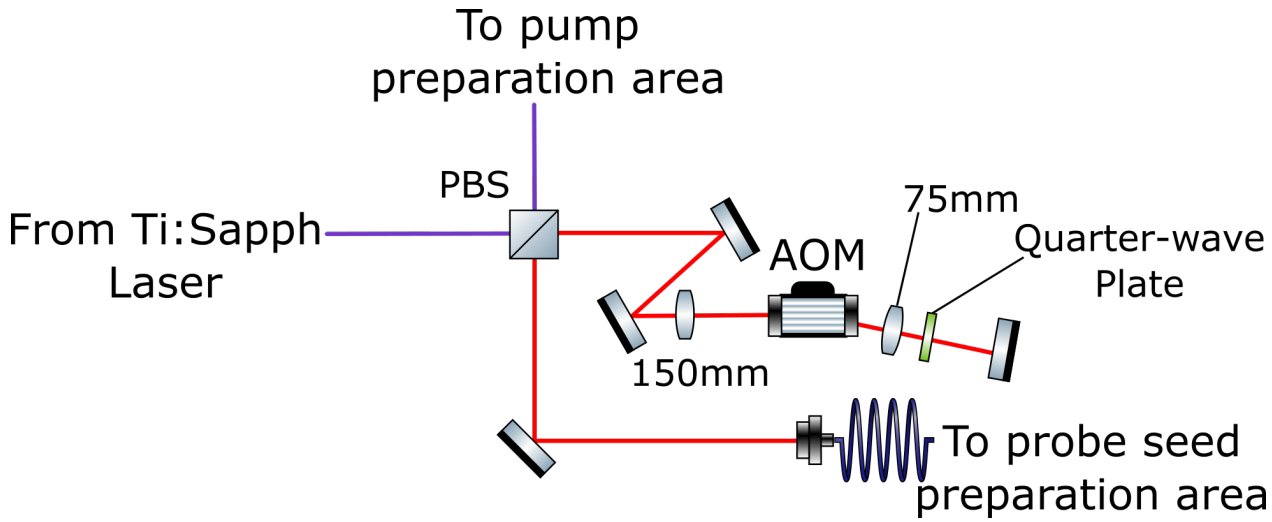

Figure 5.1: AOM double-pass set-up. The type of AOM can be found in Appendix D, the last component at the bottom of diagram a).

with an efficiency of 1% in total, with ∼30mW entering the AOM from the beamsplitter. Next the probe is coupled into an optical fibre and directed to the probe seed preparation area, before being directed into the rubidium vapour cell. The pump preparation area and all other details of the set-ups however, varied between experiments and so are detailed in later sections.

The rubidium utilized for 4WM was Rb85, heated to a vapour at ∼112°C, contained within a 12.5mm glass cell (Triad Technologies, >98% purity guaranteed), all contained within a vacuum chamber. The cell was heated via copper wire, itself heated by a power supply. In addition, a thermo-electric cooler (TEC) and a thermistor was utilized to help stabilise the temperature within the cell.

The cell was placed in a vacuum chamber to reduce atmospheric fluctuations due to convection from the heated cell. This prevented such atmospheric disturbances from interfering with the beam propagation out of the cell. The chamber, cell and TEC are shown in Figure 5.2. The pressure in the cell was lowered to the order of 10^{-3}Torr, using a roughing vacuum.

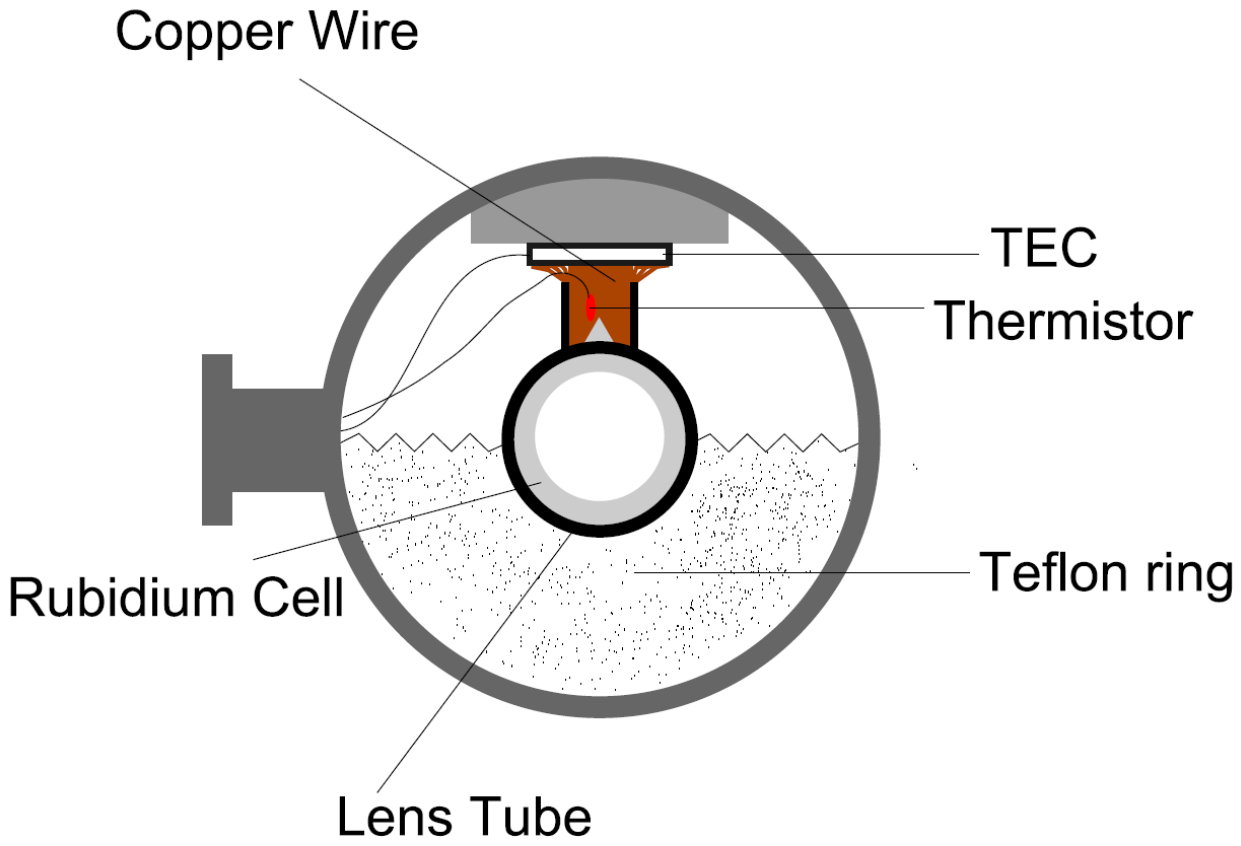

Figure 5.2: Cross-section of the vacuum chamber housing the Rb85 cell with appropriate parts labelled. Taken from [70].

Each of the experiments' set-ups are split into two main sub-systems, pre-cell and post-cell, labelled on the basis of whether the relevant system handles the laser beam before it enters the cell or after, respectively.

Additionally, steps were taken to block as much pump light as possible from following signal beams to the detectors. Due to the 4WM phase-matching condition, as detailed in Section 4.2.2, the angle between the probe and pump are on the order of mrad, making it difficult to discern the signals from the pump without adequate propagation to allow for their divergence. The issue in this case is that our QNR measurements from Chapter 2 would be altered, and uncorrelated photons would be included in and disrupt our measurements.

As these experiments intended to measure the correlation between the signal beams, residual pump photons need to be removed from the collected results, means of which were required in all three experiments. While these means were of the same nature, namely attenuation and blocking of the pump, the difference in post-cell set-ups required different placements of such attenuation/blocking. To ensure that propagation would not expand the beams quicker than they separated, and also in accordance with the diffraction criteria in Section 4.3.1, the probe and pump were always collimated through the cell.

There were also multiple maintenance issues with the set up including error-prone laser locking, atmospheric disturbance issues, gradual laser power loss, considered related to laser temperature stabilisation, gradual tainting of the coolant within the cooler and optical component alignment decay. These required careful conduct and upkeep around the lab to solve, including floating the table, deactivating air conditioners and flowboxes, periodic maintenance of the laser cooler and readjustment of optical components.

5.2 Homodyne Detection of Broadband Quadrature Squeezing

We begin with the first of the three experiments, the BLO experiment, which measured the squeezing of signal beams across a frequency range spanning the bandwidth of the 4WM process in Rb85, the squeezing bandwidth, using BLO homodyne detection. As such, the squeezing measurements made were on the field quadratures of signals via beat frequencies between said signals and local oscillators, and observed their noise using a spectrum analyser. This experiment was performed as a means of verifying the squeezing bandwidth of these quadratures, and to show that the generated beams thus carried multi-temporal mode correlations.

5.2.1 Experimental Technique & System

In Section 3.2 we considered homodyne detection using a single LO. This arrangement measured the noise of a signal by measuring the noise of the beat frequency said signal made with the LO. In this experiment, we measure two signals with differing frequencies via homodyne detection, which requires a more complicated set-up. This is due to the fact that our two signals have a large difference in frequency, of the order of 6GHz, and our detector has a limited bandwidth.

As such, it is difficult to select a single LO frequency that can mix with either signal and produce a beat frequency for each that both fall within our detector's bandwidth. If the LO frequency is too similar to one signal, the beat frequency with the dissimilar signal will be outside the detector bandwidth. If the LO frequency is too far from either signal, neither beat frequency will be detectable.

This problem can be solved through the use of a bichromatic local oscillator (BLO). Simply, rather than struggle to beat two signals with one LO, we generate two LOs with frequencies comparable to our signals, and mix them into a BLO. This ensures both beat frequencies will be within our detector's bandwidth. Figure 5.3 shows a general diagram of how homodyne detection with a BLO is achieved using 50:50 beamsplitters. This set-up yields the following quadrature operators:

$$\begin{aligned} \hat{X}_{HD\pm} &= \frac{\hat{X}_{+} \pm \hat{X}_{BLO} e^{i\frac{\phi_1+\phi_2}{2}}}{\sqrt{2}}, \\ \hat{Y}_{HD\pm} &= \frac{\hat{Y}_{+} \pm \hat{Y}_{BLO} e^{i\frac{\phi_1+\phi_2}{2}}}{\sqrt{2}}. \end{aligned} \tag{5.1}$$

Here $\hat{X}_{HD\pm}$ and $\hat{Y}_{HD\pm}$ are the quadratures leaving either the $+$ or $-$ output of the final beamsplitter, after which they are detected by the balanced photodetector. The phases ϕ_1 and ϕ_2 are the phases of the LOs with respect to the corresponding signal fields.

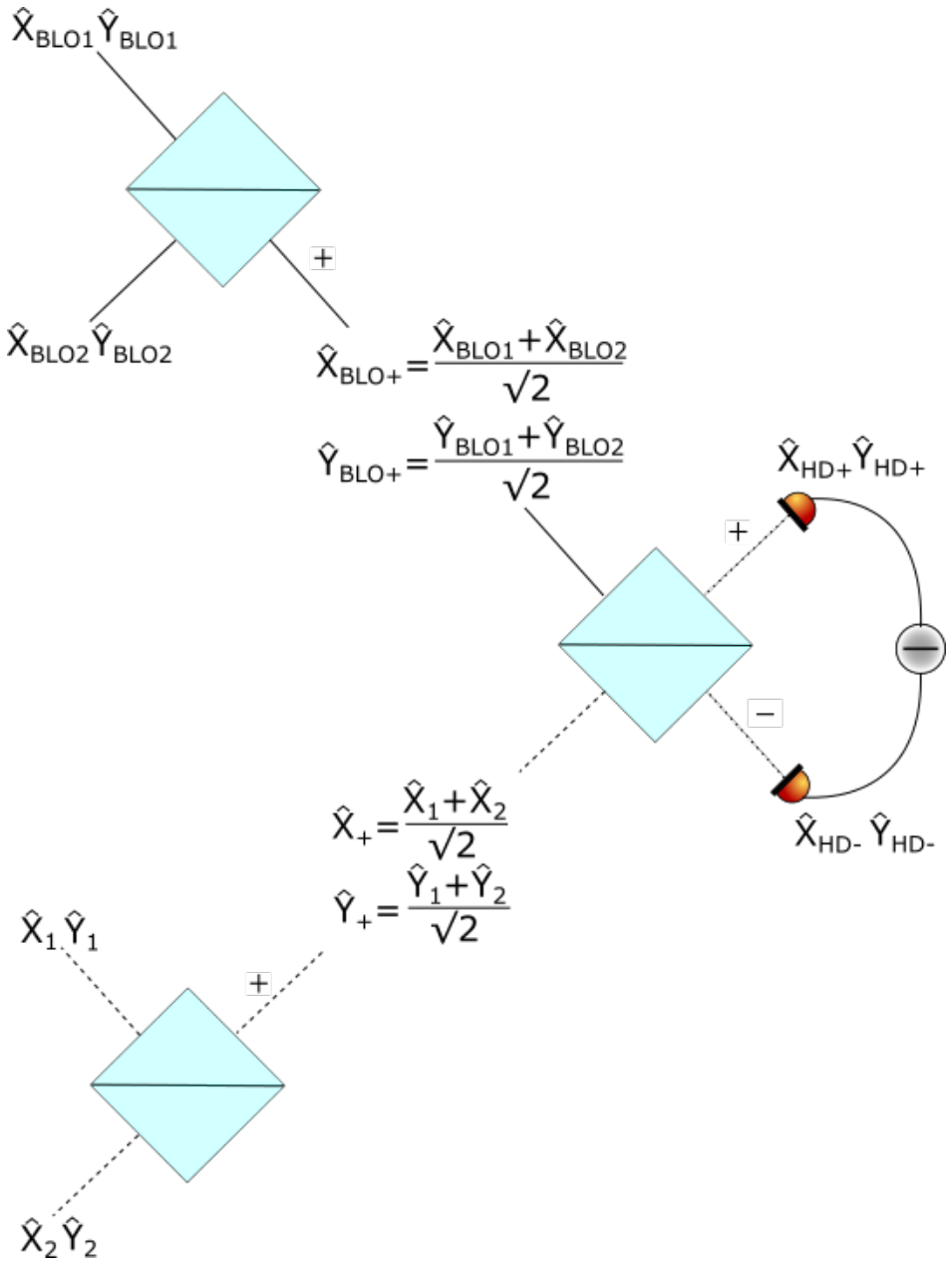

Figure 5.3: Balanced homodyne detection of two signal fields with field quadratures $\hat{X}_1$, $\hat{Y}_1$ and $\hat{X}_2$, $\hat{Y}_2$, mixed together to form $\hat{X}_+$, $\hat{Y}_+$ (for convenient beam path direction). These in turn are mixed with a BLO with quadratures, $\hat{X}_{BLO+}$, $\hat{Y}_{BLO+}$, and the resultant beams, $\hat{X}_{HD\pm}$ and $\hat{Y}_{HD\pm}$, are detected. The equations for these operators are given in Equations 5.1.

Thus, for a BLO field with LO amplitudes $\beta_1 = \beta_2 = \beta$, the photocurrents measured by this detector and the variance of the difference between them are as follows:

$$\begin{aligned}
\hat{\mathcal{I}}_{HD\pm} \propto \hat{I}_{HD\pm} \propto & |\hat{E}_{HD\pm}|^2 \propto |\hat{X}_{HD\pm} + \hat{Y}_{HD\pm}|^2, \\
\mathrm{Var}(\hat{\mathcal{I}}_{HD\pm} - \hat{\mathcal{I}}_{HD\mp}) \propto & \mathrm{Var}(|\hat{X}_{HD\pm} + \hat{Y}_{HD\pm}|^2 - |\hat{X}_{HD\mp} + \hat{Y}_{HD\mp}|^2) \\
\approx & |\beta|^2 \left(e^{2s} \cos^2 \left(\frac{\phi_1 + \phi_2}{2} \right) + e^{-2s} \sin^2 \left(\frac{\phi_1 + \phi_2}{2} \right) \right)
\end{aligned} \tag{5.2}$$

Again, here we assume that all direct terms such as $\hat{X}_+\hat{X}_+$ are of a frequency beyond the bandwidth of the detector. Thus, the quadrature noise measured by the photodetector is determined by the phase of the BLO. This effectively determines where the amplitude of the BLO is with respect to the amplitude of the signal, and how the BLO and signal interfere. In addition, realistically, the contribution of either input into the mixing beamsplitters of Figure 5.3 is determined by the phase of the field entering the beamsplitter. Thus, for a non-zero or non-$\pi/2$ phase on either or both inputs, the outputs will not be strictly $\hat{X}_1 + \hat{X}_2$, $\hat{Y}_1 + \hat{Y}_2$, etc. Instead either output will be a mixture of the two quadratures, giving in a far more complicated result when beating with the BLO.

Hence, depending on this BLO phase, sending the photocurrent $\hat{\mathcal{I}}$ to a spectrum analyser should allow us to measure the noise on the signal quadrature. Given signal quadratures of the form in Equations 2.36 and 3.2, we are then able to observe squeezed quadratures.

This experiment was intended to measure the squeezing on these quadratures when the frequency of the probe seed was changed. This change was to observe the frequency bandwidth of the squeezing, to observe whether it spanned the same bandwidth as the 4WM process. It supplements and continues the work done on BLOs in homodyne detection [67] showing that the 4WM process has ample gain and correlations across its frequency bandwidth. Measurements of squeezed quadrature noise across this bandwidth would thus prove this, as well as the multi-temporal mode nature of the 4WM process and its generated signals.

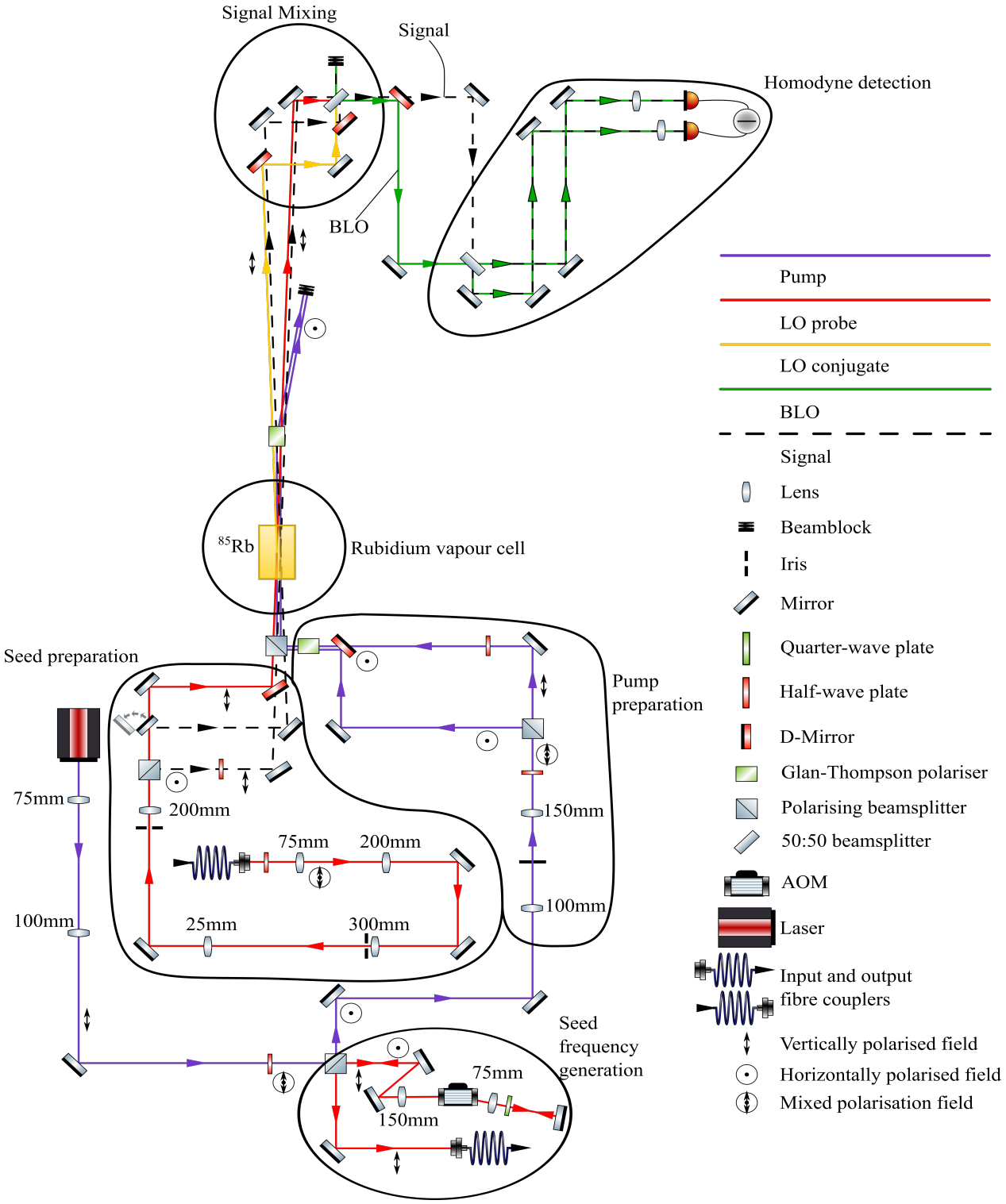

Figure 5.4: Full experimental set up with homodyne detection system for BLO measurements. Taken and adapted from [67].

The set-up used to conduct these measurements is shown in Figure 5.4. This set-up sends a pump beam of wavelength ∼794.974nm and power ∼3W into a beamsplitter, dividing it between the seed frequency generation area and the pump preparation area, as stated in the overview in Section 5.1. The AOM double-pass in the probe preparation area is set to 1520MHz, detuning the probe by 3040MHz in total, with ∼30mW entering the AOM from the beamsplitter.

After the seed frequency generation area, the probe is coupled into an optical fibre, after which it is resized to a 1mm diameter, collimated and directed to the seed preparation area. This area is designed to provide a seed for the signals whose quadratures we intend to squeeze and measure with homodyne detection, and the BLO that facilitates that detection.

As described in Section 2.3, correlated signals can be obtained from a vacuum seed and in Section 4.3.2, this behaviour extends to all vacuum states that satisfy the phase-matching condition. As such, we can leave the probe and conjugate seeds into the Rb85 cell as vacuum when taking measurements. For convenience, we then also generated our LOs by 4WM in the same Rb85 vapour cell but vertically displaced from the signals, as shown in Figure 5.5.

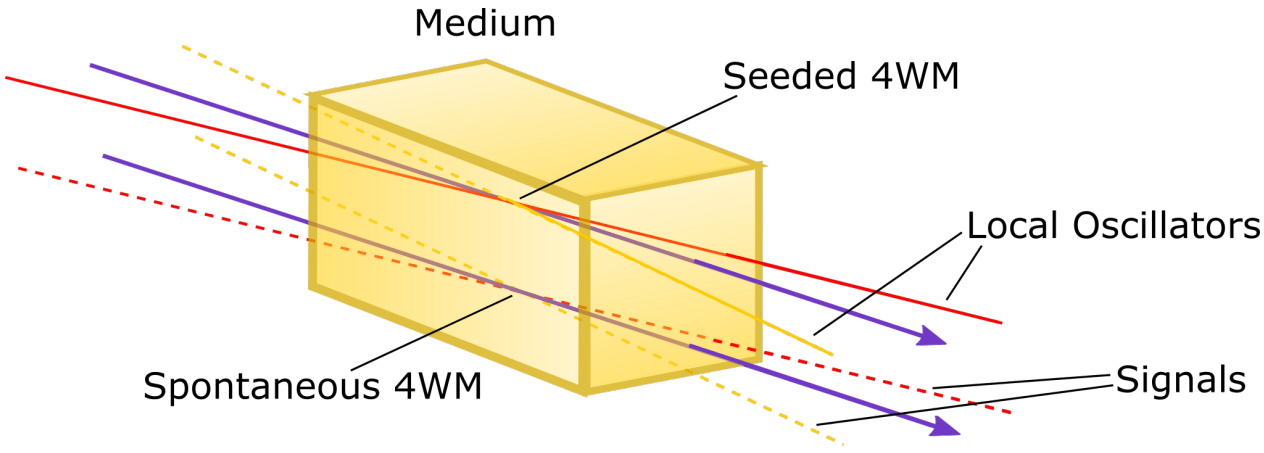

Figure 5.5: Arrangement/state of probe, conjugate and pump beams for the seeded (solid lines) and unseeded (dashed lines) case. The red lines denote probe beams, the orange lines denote conjugate beams and the purple lines denote the pump beams.

Thus we generate two LOs with different frequencies, each equivalent to the frequencies in the probe and conjugate signals. Overlapping these LOs with the probe and conjugate signals in the same fashion as the BLO homodyne detection scheme in Figure 5.3 should allow for measurement of quadrature squeezing.

To facilitate this double instance of 4WM, the initial pump of ∼1.5W was firstly resized to 2mm diameter, collimated, and then split into two pump beams in the pump preparation area. These two beam paths were vertically separated during their course, providing one pump for the vacuum signal generation and another pump for the LO amplification. The LO seed beam and both pump beams are finally directed into the cell together, with ∼6mrad between the LO seed and its pump, along with the vacuum seeds.

Having arranged our seeds, the resultant signals and LOs needed overlapping in order to observe squeezing. To verify that the signals and the LOs were properly overlapped, a waveplate before the seed preparation area was turned, with a later beamsplitter then increasing the otherwise vacuum probe seed's brightness. Doing so shines bright signals along the beam paths of the squeezed vacuum fields we intend to measure. The bright signals are then directed through the post-cell homodyne detection system, shown in Figure 5.6. This method was implemented in [67].

The overlap of the beams in the BLO homodyne detection set-up is shown in Figure 5.6. This required the use of two magnet-mounted mirrors, which diverted the two beams directed toward the differential detector before it reached them. These beams were then mixes of the probe signal and its corresponding LO component of the BLO, and the conjugate signal and its corresponding LO component of the BLO.

To ensure good overlap between the signals and the BLO in either of these beams, they were diverted to a screen, at which an infrared camera was pointed. The overlap of the beams was thus judged by interferometric fringes induced via the beams' propagation through this system at two different points. Adequate overlap was considered achieved with the

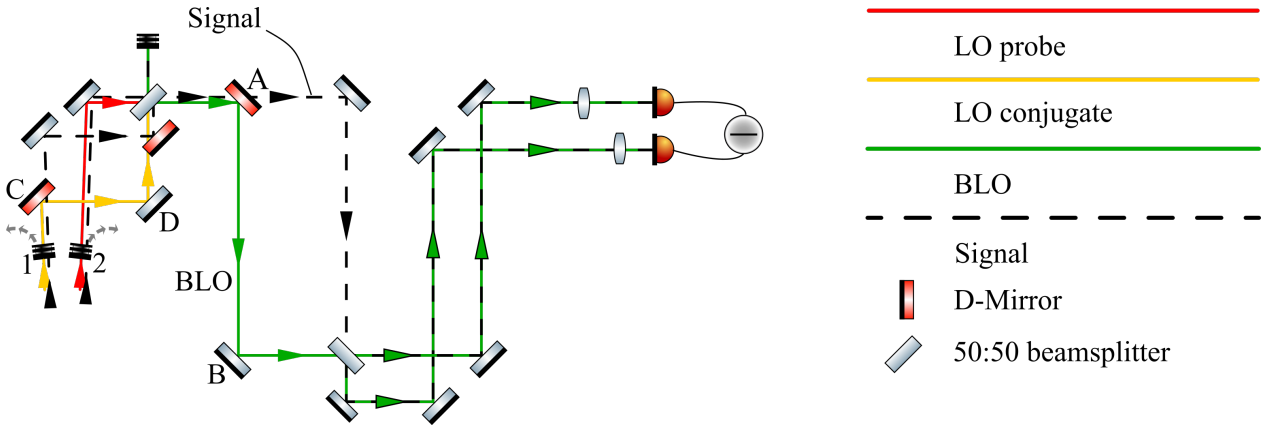

Figure 5.6: The homodyne detection stage. The BLO is aligned to the signal field using visibility of interferometers independently for the probe (using mirrors A and B, and a beam block at position 1) and conjugate frequencies (using mirrors C and D, and a beam block at position 2). Where, on the diagram, the signal and LO fields are slightly separated, they are split vertically in the experiment. Taken from [67].

observation of radial fringes, indicating no angle between the beams.

After this optimisation, the waveplate was turned back to reduce the probe seed back to vacuum. The LOs and squeezed vacuum signals then progressed through this aligned set-up before reaching the balanced differential detector. The photocurrent difference from this detector was then sent to a spectrum analyser set to zero span mode and an oscilloscope. The oscilloscope was used to measure the power going into either photodetector, giving a measure of the QNL of the photocurrents for normalisation of the noise measurements.

This gave a clearer indication of whether the noise was squeezed, corresponding to the coherent state variance in the QNR expression of Equation 2.35. This spectrum analyser was set to a analysing frequency of ∼1MHz, with resolution bandwidth of 100kHz, video bandwidth of 30Hz and sweep time of 0.9s. Three results were taken at a time and then averaged, before changing the BLO frequency by intervals of 2MHz. The double-pass AOM RF is thus changed by intervals of 1MHz from 1518 to 1528MHz.

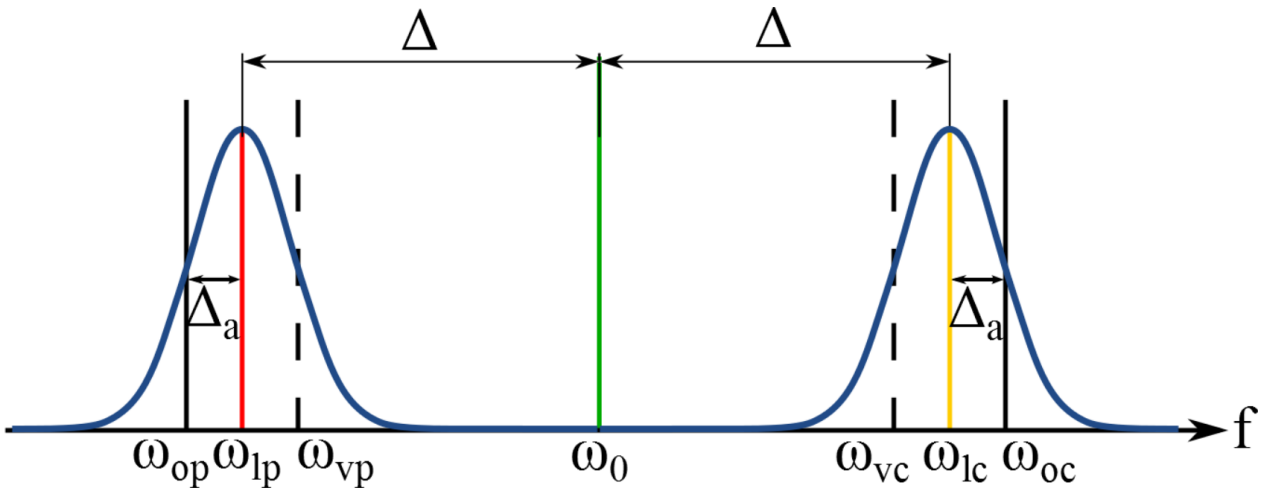

Figure 5.7: The frequencies, and resultant beat frequencies, present in BLO homodyne detection. The blue Gaussians represent the bandwidth of the squeezed vacuum field, a mixture of probe and conjugate, with ω_{lp} and ω_{lc} being the frequencies of the probe and conjugate LOs, in red and orange respectively. Δ_a is the analysing frequency of the spectrum analyser, and so observes a particular beat frequency between the LOs and the squeezed field. This Δ_a hence selects particular beat frequencies between the LOs and the signals, referred to as sidebands, ω_{op} and ω_{oc}. The spectrum analyser makes no distinction between positive and negative differences however, which yields a second pair of frequencies, called image bands, ω_{vp} and ω_{vc}, shown by dotted lines. Taken from [67].

This detuning amounts to a scanning of the squeezing spectrum, as evidenced in Figure 5.7. The analysing frequency, Δ_a, is that of the spectrum analyser when set to zero-span mode. As the LO frequencies, ω_{lp} and ω_{lc}, will beat within the entire bandwidth, one particular beat frequency can be observed through selection of this analysing frequency, referred to as a sideband. Thus changing the RF on the probe AOM changes the LO frequencies, moving it across the signals' bandwidths.

As these sidebands are the beat frequencies between the signals and their LOs, they are correlated according to the nature of the 4WM process. Referring back to Section 3.2, the

phase of the LOs and the signal will thus determine which of the quadratures is measured, and so determine the fluctuation of these sidebands. In Section 2.3.3, it was shown that the X and Y quadratures show squeezing when subtracted and summed respectively. As these measurements are taken with differential detector, squeezing will be observed for the X quadrature only. Thus the LOs must be in phase with this quadrature in order for the BLO homodyne detection scheme to detect squeezing.

5.2.2 Results & Analysis

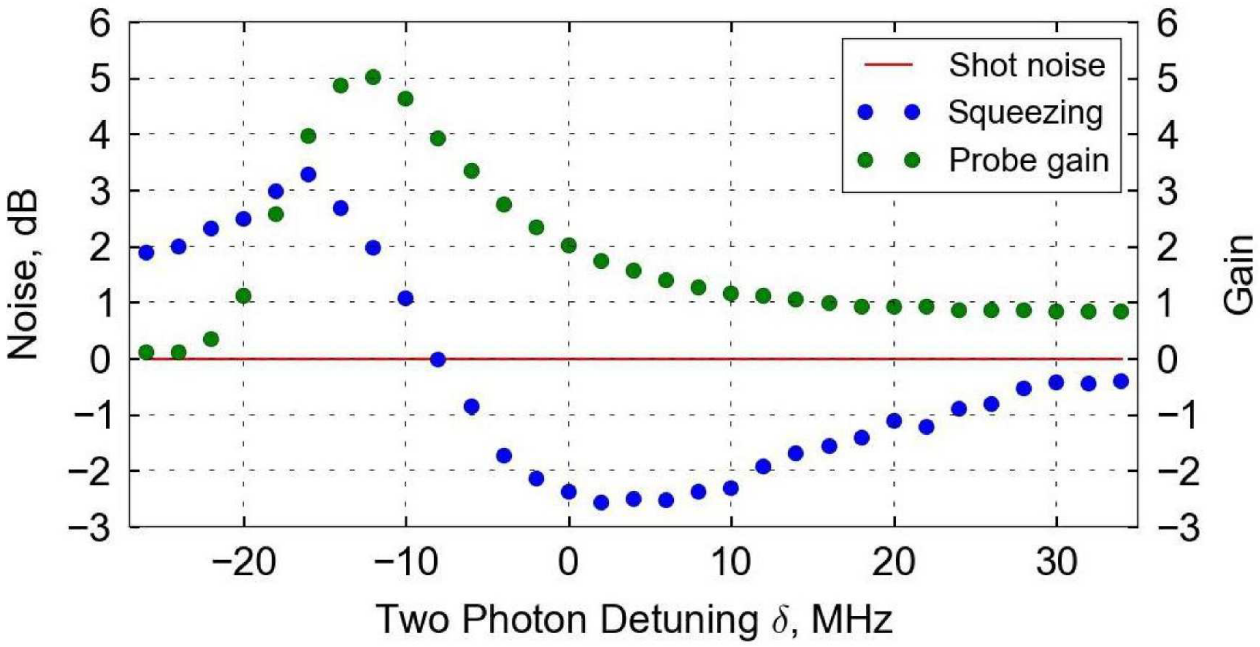

Figure 5.8: Results from the BLO experiment, using homodyne detection to measure the quadrature squeezing. The squeezing was found by normalising with respect to the shot noise, shown as the red line, and the detuning was normalised to 1518MHz. Taken from [65]

The results for this experiment are shown in Figure 5.8. The extension of this squeezing across a range of frequencies either side of this shows the clear broadband nature of the 4WM,

extending across a bandwidth of ∼40MHz. As such, these results indicate the multi-temporal mode nature of the 4WM process. That is, there are a number of different frequencies that can participate in the 4WM process and produce correlated signals, which in turn can be subtracted to produce squeezing. Each different frequency is effectively a different temporal mode of the kind described in Section 2.2.1. As multiple pairs of frequencies still produce squeezed light when subtracted, the process is multi-temporal in nature, spanning many different longitudinal modes of light, each corresponding to a different frequency.

Additionally, there is some concern as to the capability of the set-up in maintaining alignment when changing the detuning. Given that parts of the set up are frequency sensitive, detuning the LO seed may cause issues with alignment and subsequently impair the detection of quadrature squeezing. To verify that the results in Figure 5.8 are accurate, we conducted an ID squeezing experiment where the detuning of the probe seed was changed over the same bandwidth. The results are in Figure 5.9.

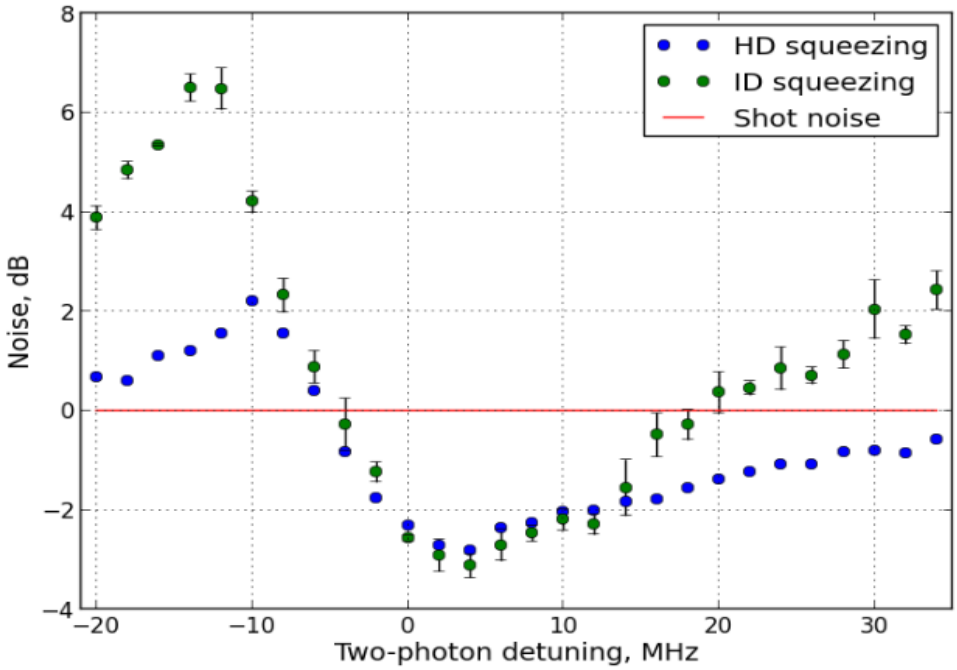

Figure 5.9: Intensity difference squeezing measurements for a range of two photon detunings.

As these results follow the same trend as those in Figure 5.8, the detuning thus has little effect on the alignment of the homodyne detection set up and Figure 5.8 shows accurate results. These results thus show the multi-temporal mode quality of the signals generated by the 4WM.

5.3 Photodetection of Guided Intensity Difference Squeezing

The purpose of this experiment was partly to verify that detection of squeezing within the near field of a MSM beam was possible. Additionally, it was also a collaboration within the group to attempt to transmit squeezed light through an optical waveguide and to observe whether the correlations could be preserved.

This experiment was hence conducted partly to evaluate whether the camera experiment would be able to observe near field squeezing at all. This was due to it being uncertain as to whether the near field of the signal beams would express correlations as theory predicts or if our set-up even reproduced such theory correctly.

To do so, we intended to show that local intensity correlations were present across the probe and conjugate beam profiles. In addition, an additional component was added, the conduit, to observe whether these same correlations were retained after passing through a waveguide. This experiment yielded a positive result, where several regions across the probe and conjugate beams were isolated using slits then detected via balanced photodetectors. The subtraction of the resultant photocurrents was fed into a spectrum analyser, which yielded squeezing. This was conducted first without the waveguide, then with the waveguide to compare. The slits were also moved horizontally and vertically across the beams, to observe the range of squeezed ranges in either direction.

5.3.1 Experimental Technique & System

For this experiment, a similar set-up as past tests of these correlations was used, such as [60]. A slit scheme was implemented to selectively cover the beams in the near field and expose a range of regions of each beam to a balanced photodetector. This would verify whether the correlations were definitely present in the near field and behaving as expected, as correlated regions would give squeezing. As mentioned, the conduit was added to observe whether these same MSM correlations persist after passing through a conduit, the aforementioned regional comparison via slits also being a test of this.

Figure 5.10 shows the complete set up used to collect the results in this section. This arrangement is similar to the set-up in section 5.2, however, there are significant differences. Before the cell, the probe seed and pump preparation areas both had their imaging systems changed, so that only one pump and probe were directed into the cell. The system was also changed to adjust the sizes of the probe and pump in the cell image plane, to improve gain. The addition of an AOM in the pump preparation is also noted, though it serves no real function here. It was added as attempts at the camera experiment had been ongoing before this experiment. As such, in order to separate the orders output from this added pump AOM within given distances, the detuning was set to -80MHz. To compensate for this and re-establish the double-Λ transition, the probe was also detuned by approximately -80MHz by decreasing frequency of the double-pass AOM by $\sim$-40MHz from its previous value of 1520MHz, down to 1482MHz.

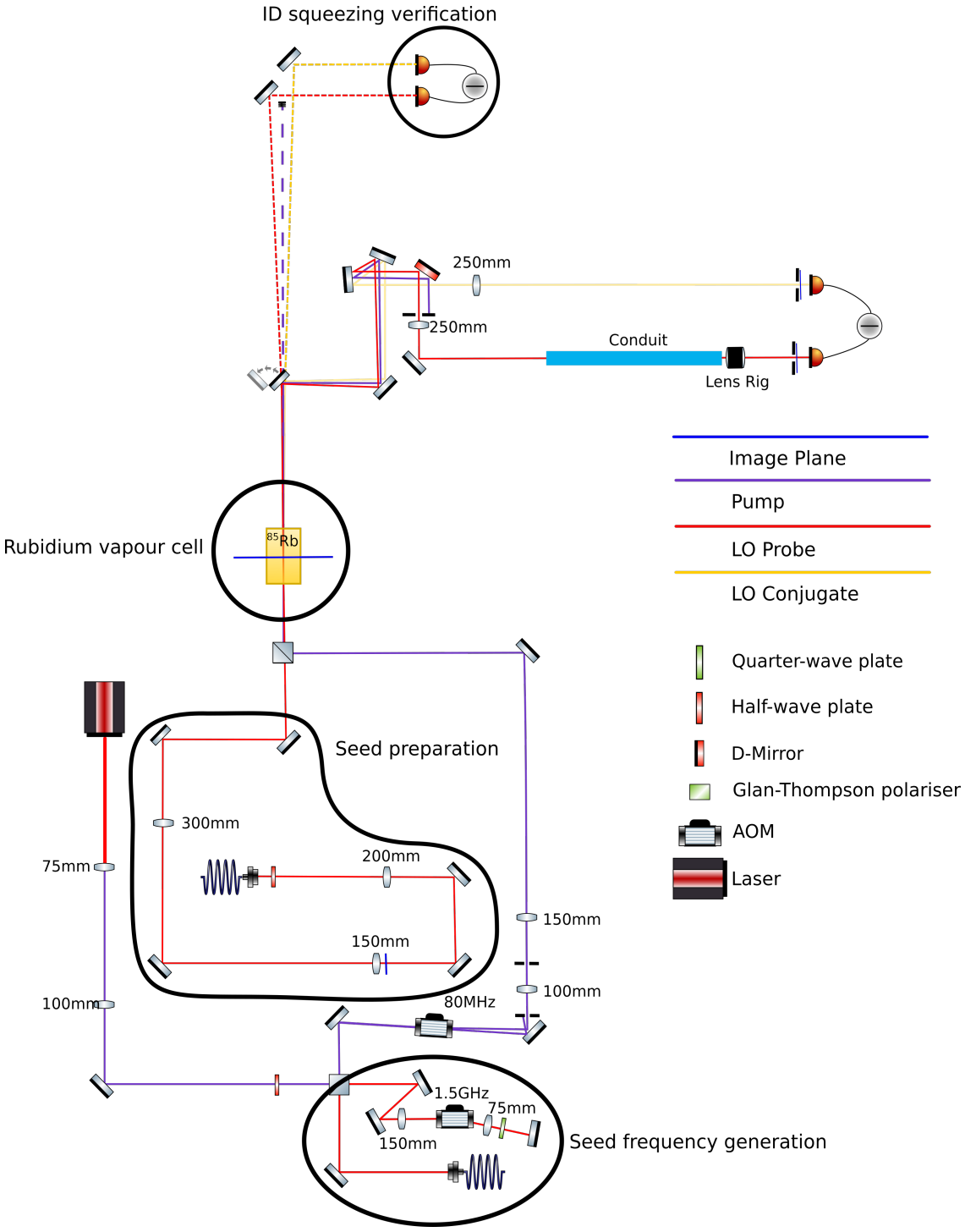

Figure 5.10: Full setup for the conduit experiment. The Lens Rig was comprised of two lenses, f=0.8mm and f=1.6mm, used to counteract the divergence from the conduit.

In the post-cell, the homodyne detection system was no longer necessary and hence removed. Instead, two f=250mm lenses, one for the probe, the other for the conjugate, were placed to image the centre of the cell and point of generation of the correlations. This was done to image the centre of the cell, and thus the correlated regions, onto the conduit to allow the image to be transmitted. As such, the conduit should preserve these regions and so preserves the correlations. The exact imaging system is shown in Figure 5.11:

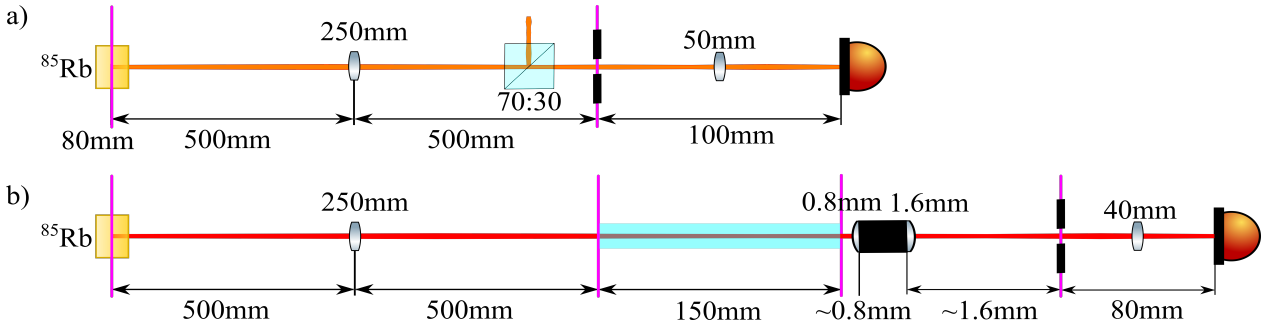

Figure 5.11: Specific imaging system used for the conduit experiment. Diagram a) is the imaging system for the conjugate beam. Diagram b) is the imaging system for the probe beam, including the conduit. The purple lines represent the imaging planes.

As seen in Figures 5.10 and 5.11, the probe and conjugate underwent different imaging systems, to compensate for the introduction of the conduit into the probe path. After the f=250mm lenses, the probe travels 500mm and is imaged onto the conduit's entrance, while the conjugate travels 500mm and is imaged onto its slit. The probe propagates through the conduit, before emerging, collected by a lens rig to counteract its large divergence, before it is imaged onto its slit. The length of the conduit was 152.4mm with an outer diameter of 3.2mm, with 12µm fibres and packing fraction of 50%, given a 1:1 ratio between core and cladding.

The choice of f=250mm lenses in this experiment also ensured that the beam profile of the probe image would retain a coherence length larger than this inter-fibre spacing. This was to ensure that loss on the probe would not prevent the observation of squeezing, and that

the resolution would not degrade the regions the slits were intended to select.

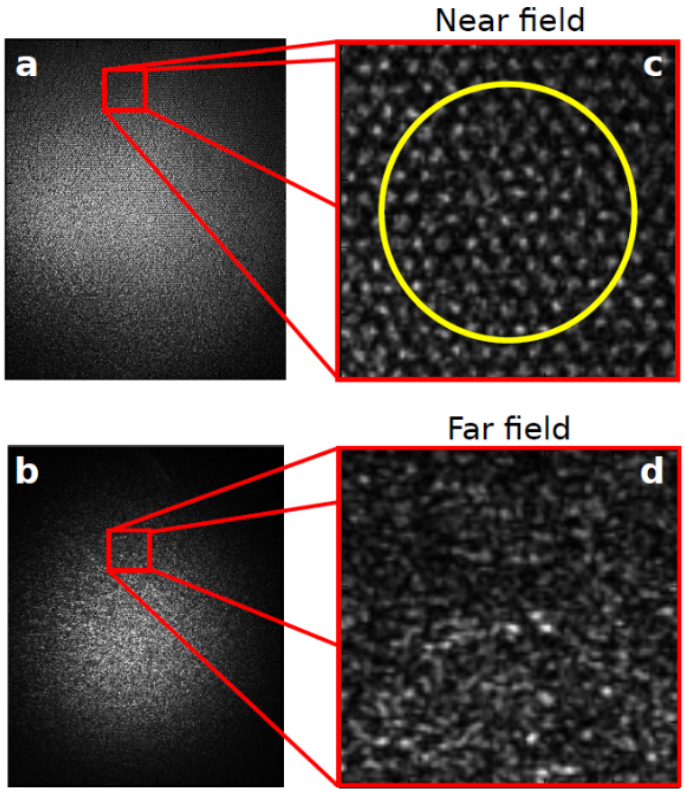

Figure 5.12: Near and far field images of the probe after passing through the conduit. Diagram a) shows the near field, which emphasizes the arrangement of fibres within the conduit. Diagram b) shows the far field, which emphasizes the speckle pattern resulting from randomisation of phase each fibre induces in light it transmits. Diagram c) then shows a magnified section of diagram a), for clarity, with a yellow circle showing the estimated size of the coherence area. Diagram d) shows a magnified section of diagram c), also for clarity. Taken from [66].

These qualities would allow the conduit to resolve the beam to a resolution capable of preserving the coherence area. The imaging of the near and far field of the probe after the conduit is shown in Figure 5.12, showing the packing and arrangement of the fibres in the

near field image, and how the far field results in a speckle pattern due to randomised phase of the light exiting the conduit.

Post-conduit, the probe was directed into a pair of lenses that mitigated the large divergence of the beam, though increased its diameter to twice that of the conjugate. Collecting light from the probe beam thus required additional lenses. For this, a lens rig containing a f=0.8mm lens and a f=1.6mm lens was used. These lenses collected and collimated light out of the conduit (the f=0.8mm lens) before imaging it onto the slit plane (the f=1.6mm lens).

As an aside, it should be noted that this exact set-up results in correlated regions being in unexpected positions within their beams. Indeed, these positions are contradictory to the propagation of correlations as seen in Section 4.3.2. This is due to inversion from reflection on the mirrors and the focussing of the lenses. The number of mirrors thus give number of horizontal inversions, while the number of lenses that focus the light to a waist gives the number of radial inversions. The difference between the number of waists and mirrors either beam encounters will determine whether the correlated regions in the near field will be found in the same location within their beams, or symmetrically inverted.

Furthermore, due to the 30% efficiency of the conduit, losses incurred to the probe intensity by the conduit had to be compensated for on the conjugate. In accordance with Equations 3.13 in Section 3.3, a beamsplitter was included in its beam path, and attenuated the conjugate to $\sim$70%, for a gain of $\sim$1.5 and probe efficiency of 30%.

This gain was a result of changing the pre-cell probe seed preparation alignment, which changed the angle between the probe and pump within the cell. This was done in order to maximise the separation between the signal beams and the pump. As contamination from the pump would add extra noise to the measurements and the set-up had limited space, this increased separation allowed for greater clearance between the pump and the signals for a pump block to be placed without clipping the signals in the far field. The angle between probe and pump was slightly larger than 6mrad.

This is shown in Figure 5.13. If the darkened region, the pump block, encroaches on the squeezed vacuum around the probe and conjugate in the far field, the near field images of these beams will be degraded. As detailed in Section 3.3, any loss in a squeezed state results in a loss of squeezing.

In this case, this loss of squeezing occurs at the high spatial frequencies of the image, as the pump block encroaches on the correlated vacuum surrounding the signal beams in the far field. This loss then lowers the overall squeezing detected by removing correlated vacuum from the images, which leaves uncorrelated vacuum with fluctuations that do not cancel upon subtraction.

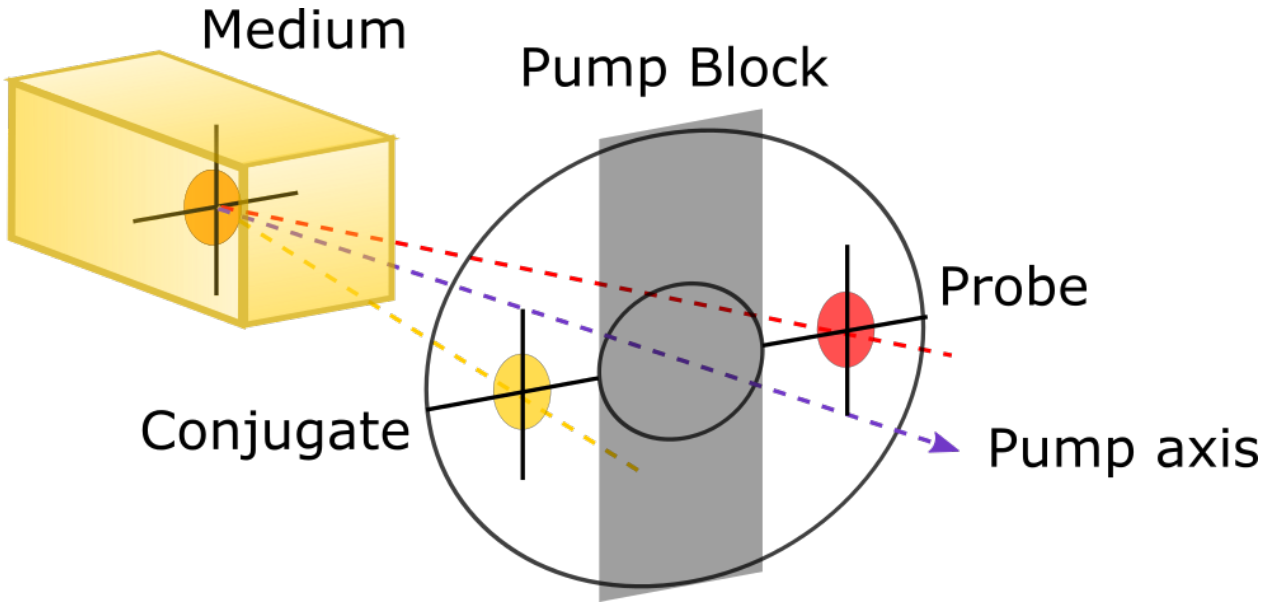

Figure 5.13: Diagram of ideal blockage of pump in the far field, where the pump, probe and conjugate diverge enough to avoid clipping the correlated vacuum around the probe and conjugate beams.

To conduct the experiment, each slit was closed to the point where intensity difference squeezing began to vanish, which was ∼15% of the beam's diameter. The positions of the slits were noted, and the squeezing recorded three times before moving the slits by set amounts.

Each position on the probe was measured against a series of positions on the conjugate. Once the conjugate slit had spanned the conjugate beam profile, the probe slit was moved, and the conjugate slit spanned the same positions again.

Near relatively good levels of squeezing, the conjugate slit was moved by smaller intervals, to ensure good resolution of the squeezing profile. These movements were conducted four times, twice with the conduit, once vertical, once horizontal, then twice without the conduit, again once vertical, once horizontal, for comparison.

All squeezing measurements were intensity difference, using a balanced differential photodetector to detect and subtract the beams, and a spectrum analyser and an oscilloscope to analyse the results. The analyser was set to a zero frequency span at 2.25MHz and a sweep rate of 2.1s, with resolution bandwidth of 30kHz, video bandwidth of 30Hz and sweep time of 2s. The oscilloscope was used to measure the intensity of the signals detected by the photodiodes of the detector, blocking one beam to measure the other, giving a measure of their combined power in order to acquire a QNL.

5.3.2 Results & Analysis

The results of this experiment are shown in Figure 5.14. These show ∼-1dB of squeezing at their most optimal, that is, where the slits isolate corresponding regions in either beam. For clarity, the slit positions producing the troughs in Figure 5.14 are depicted in the same colours in Figure 5.15, where the motion of the slits is also explained.

The vertical and horizontal slit scannings show a difference in the number of regions correlated, regardless of whether the conduit was implemented. This difference arises due to the beam block, which stands vertically and clips the sides of the beams. This results in the far field of the probe and conjugate being clipped, removing high spatial frequencies and resulting in less squeezing, or rather, additional presence of unsqueezed vacuum.

Further to this, a) and c) show similar dips to b) and d), with only a slight reduction in

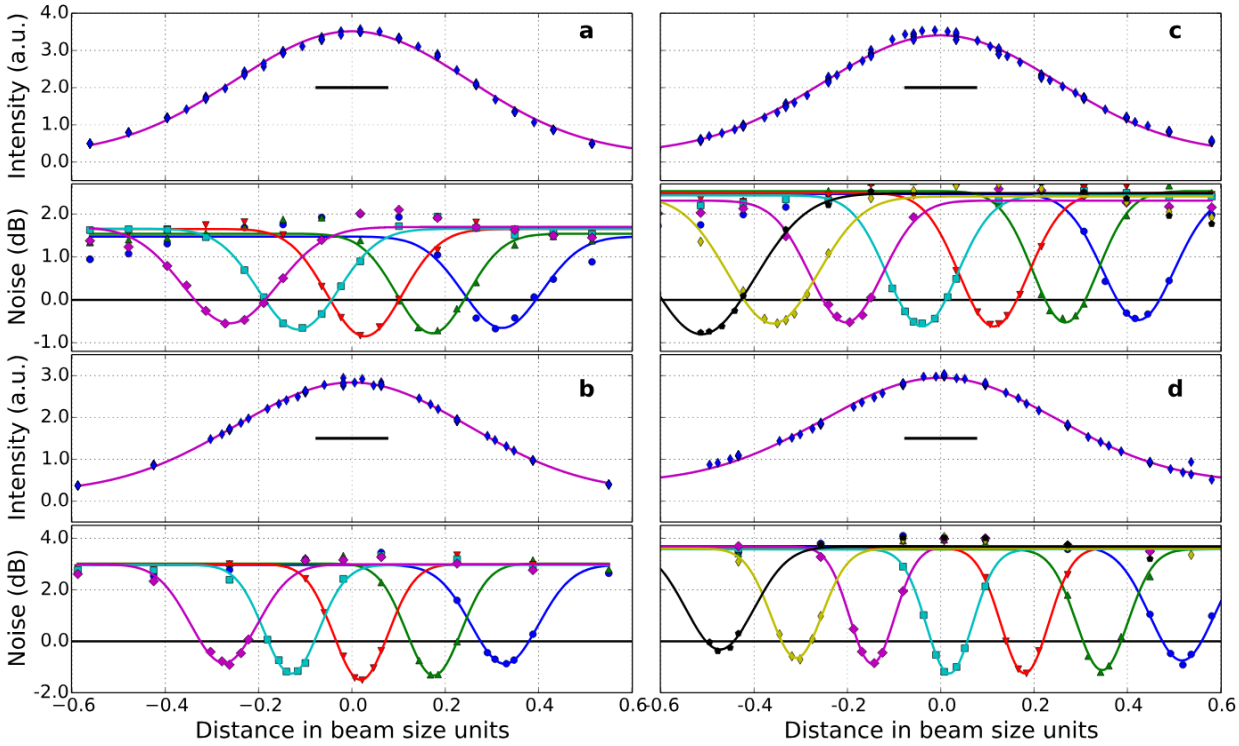

Figure 5.14: The results of scanning slits across correlated probe and conjugate beams after transmitting the probe through the conduit and attenuating the conjugate to compensate for losses. a) and c) are the horizontal and vertical slit scanning results with the conduit, respectively, and b) and d) are the same scanning directions without a conduit, respectively. The beams were squeezed to ∼-3dB without the slits. The black lines show the slit sizes on the probe and conjugate. Taken from [66].

squeezing. This indicates that the conduit preserves the correlations. The shapes of these dips are largely a combination of the slit transfer function and the coherence area profile. To a lesser extent, they are also shaped by losses from the conduit and the imaging system, as well as spherical aberrations. Due to this, the dips can be considered estimates of the coherence area. These dips are of the order of 100µm is size, making them at least 10 times larger than the conduit's fibres, making the conduit's resolution sufficient for preserving the coherence area.

To obtain an estimate of the effect of the conduit on the spatial bandwidth of the correlations, a $\mathcal{R}$ parameter was then formulated as the ratio of width of the troughs to the Gaussian beam

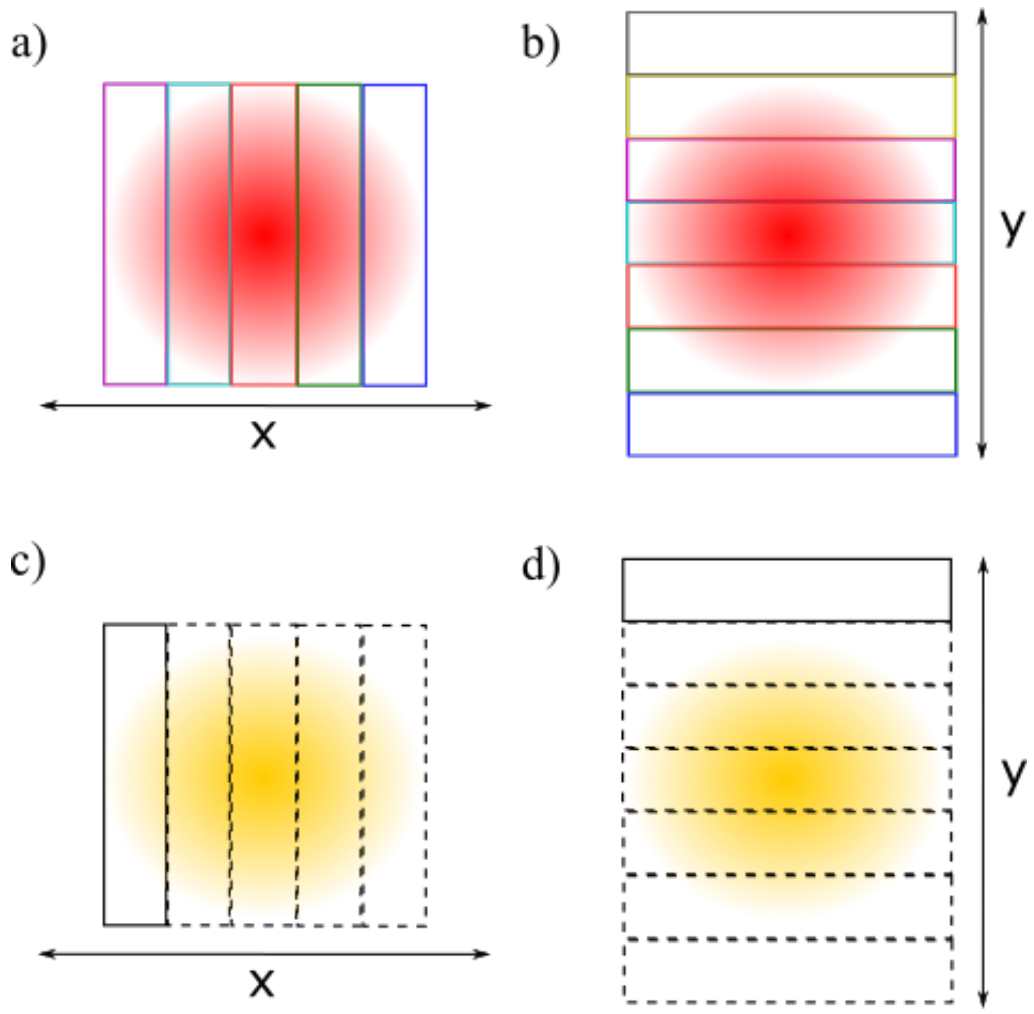

Figure 5.15: Positions of the slits across the various beam profiles. The probe slit would be placed at one of the coloured slit positions, as in diagrams a) and b), and the conjugate slit would be moved from the solid slit position to each dashed slit position, as in diagrams c) and d). At each conjugate slit position, an intensity difference measurement was taken and the squeezing calculated, until the conjugate slit reached the other side. Once it had, the collected data was used to plot the trough of the colour corresponding to the probe slit colour in diagram a) or b). Then the probe slit was then moved to another coloured slit position, and the conjugate slit movements were repeated, until the probe slit had been placed at each coloured slit position. Each beam profile represents the e^{-2} radius.

diameter. This parameter gives an idea of the percentage of the beam profile that the troughs, or selected spatial mode, covers. In the case of the conduit, the vertical and horizontal results yield 0.29 and 0.32 respectively. In the case of without, the $\mathcal{R}$ is 0.20 and 0.27 respectively. This parameter, $\mathcal{R}$ is thus linked to the spatial frequency pertaining to the region isolated by the slits. As this region is clearly smaller than the beam itself, and that the total entire beam were squeezed to $\sim$-3dB, all intermediate regions between the slit sizes and the size of the beam were also squeezed, to varying degrees. As such, the conduit has been shown to successfully transport and preserve multi-spatial mode correlations, and proves it is possible, if not likely, for similar waveguides.

Chapter 6

Photodetection of MSM Intensity Difference Squeezing

We now introduce the last of our results in this thesis, collected from the camera experiment. The purpose of this experiment was to acquire near field image data from a CCD camera. Through analysis, correlations within these images could be seen to yield intensity difference squeezing across multiple spatial frequencies.

As discussed in Chapter 2 and 4, and elaborated on in Chapter 5, this is achieved by 4WM within a Rb85 vapour cell that correlates two nondegenerate states by amplification. This results in the beams having correlated intensity fluctuations within corresponding regions of their transverse profile, which under subtraction cancel out and lower the noise of those regions. Due to technical and low spatial frequency noise, this phenomena is most easily observed by transforming the images to Fourier space.

As this transform expresses the image as a function of spatial frequencies, calculating the noise of a transformed image allows for observation of noise beyond its spatial DC component. This approach thus realises a spatial frequency spectrum analyser that processes and displays

the noise of the spatial frequencies of the images. This is analogous to the typical spectrum analysis, which gives the spectral noise density as a function of temporal frequency.

Through this method, we find results of this thesis yield 8 spatial modes that exhibit squeezing, as presented in Section 6.2. In addition, we examine these results further through various algorithms examining the noise of the spectra and images to observe if there are any obvious changes that could be made to improve the squeezing.

6.1 Experimental Technique & System

To capture images capable of exhibiting squeezing via spatial frequency spectrum analysis, the experiment had to capture a series of images using a CCD camera. Specifically, the CCD would simultaneously capture the near-field intensities of the probe and conjugate signal beams in a series of snapshots. Each set of images captured this way thus correspond to a temporal integration of the signal beams' intensity spanning a given period of time.

This series of images thus constitutes a set of sequential temporal integrations of the beams' intensities which, when simultaneous intensity measurements are Fourier transformed and subtracted, can be seen to be squeezed. This squeezing is made apparent by calculating the variance between the sequence, providing us with spatial frequency noise spectrum. For improved statistics, we then repeat this process multiple times and average the resulting noise spectra.

The CCD camera used for image acquisition was a Princeton Instruments PIXIS-1024BR eXcelon (with a 98% quantum efficiency), and for our purposes it was run in Kinetics mode, as shown in Figure 6.1. This divided its CCD in a set of smaller slices, the bottommost of which would expose for a given period, shift the data up into an empty slice then expose again until all slices held data.

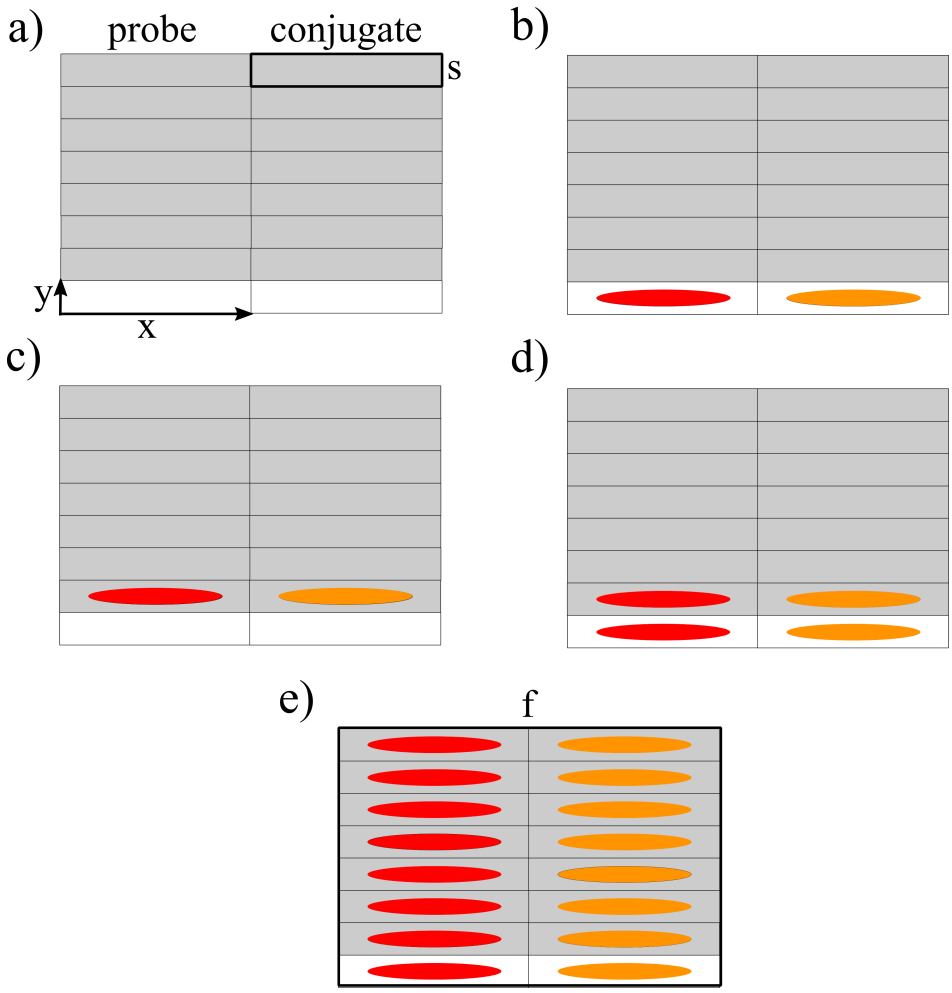

Figure 6.1: The camera shifting process. Diagram a) is the empty CCD, showing the entire frame split into slices, s, and divided down the centre in probe and conjugate sides, with the dimensions y and x labelled, b) the CCD after exposure, c) after shifting, d) after second exposure and e) after repeating this until the frame, f, is filled with beam data.

Thus the intensity data was arranged according to the image dimensions/slice size, x and y, the number of slices the CCD was divided into, s, and the number of times this process was repeated, yielding the frames f. As the slices are filled by the end of this process, repeating it thus requires the CCD to be read out, obtaining the data and clearing the CCD for the next frame to be taken.

Given these dimensions, our intensity distributions are arranged as $I(f, s, y, x)$, with the probe situated on one side of the frame, and the conjugate on the other. The intensities I_p and I_c are thus either side of the intensity distribution $I(f, s, y, x)$, splitting the CCD down the centre to separate the two beams apart and allowing for subtraction. To observe squeezing, the aforementioned spatial frequency spectrum analysis is implemented like so:

$$\mathrm{QNR}_{dB}(k_y, k_x) = 10 \log_{10} \left(\left\langle \frac{\mathrm{Var}_s(\mathcal{F}_{xy}(I_p) - \mathcal{F}_{xy}(I_c))}{\langle \sum_{xy} I_p \rangle_s + \langle \sum_{xy} I_c \rangle_s} \right\rangle_f \right). \tag{6.1}$$

Here f, s, y and x have their established meanings and the operators' subscripts refer to which of these dimensions the operations are conducted on. As such, $\mathrm{Var}_s()$ is the variance over the slices, $\mathcal{F}_{xy}()$ is a Fourier transform over the xy dimensions of the intensity, $\langle \rangle_s$ is the average over the slices and $\langle \rangle_f$ is the average over the frames. The variance of the Fourier transform is then calculated using $\mathrm{Var}_s(\mathcal{F}) = \mathrm{Var}_s(\Re(\mathcal{F})) + \mathrm{Var}_s(\Im(\mathcal{F}))$.

The terms in the QNL in Equation 6.1 expression are the QNL of each frame, $\mathrm{Var}_s(I)_{\mathcal{C}} = \langle \sum_{xy} I(f, s, y, x) \rangle_s$, which in turn is composed of the QNL of the probe and conjugate in each frame, $\langle \sum_{xy} I(f, s, y, x) \rangle_s = \langle \sum_{xy} I_p \rangle_s + \langle \sum_{xy} I_c \rangle_s$. As expected of such an analysis, the values of $\mathrm{QNR}_{dB}(k_y, k_x)$ give the various QNR_{dB} values of spatial frequencies within the intensity difference Fourier spectrum. These values then indicate the squeezing of various spatial modes within the image data when they fall below 0.

This spatial frequency spectrum analysis is further supplemented with an algorithm analysing the content of the spectrum, referred to as radial averaging. This method operates in two ways, either averaging the noise values present on a circular path of some given radius or all the values enclosed within said circular path. These two approaches are depicted diagrammatically in Figure 6.2.

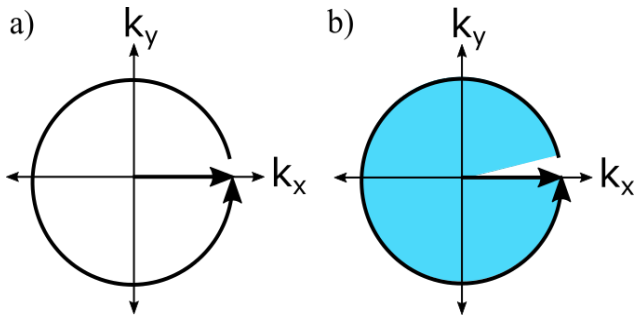

Figure 6.2: Different applications of radial averaging algorithm. Diagram a) shows the circular path algorithm, useful in considering a set of noise values with specific spatial frequencies. Diagram b) shows the circular region algorithm, useful in ascertaining the general noise of a range of spatial frequencies.

This radial averaging method was conducted to make observations of noise spectra clearer. The first, the average noise on a circular path, was designed to compare the noise on regions within the image that have the same area. By applying this algorithm multiple times while increasing the circular path's radius, this method builds up a 1D spectrum that depends on the spatial frequency, or equivalently the magnitude of the transverse wave vector. The second method, an average of the spatial frequencies enclosed within the circle, provides a metric for the noise within a certain range of frequencies, which can be used to gauge the presence of excess noise.

This set-up was designed and implemented to avoid, and where possible lower, non-signal noise sources in the images, including noise from laser drift and excess pump light. Firstly, the choice of using Kinetics mode was made in order to avoid low frequency noise due to laser drift/noise. While the exposure time could be set to any desired value, the data shifting rate of the camera was 3.2µs per row. Proceeding to the means of data acquisition, this experiment used a similar set-up to the previous experiments, as shown in Figure 6.3.

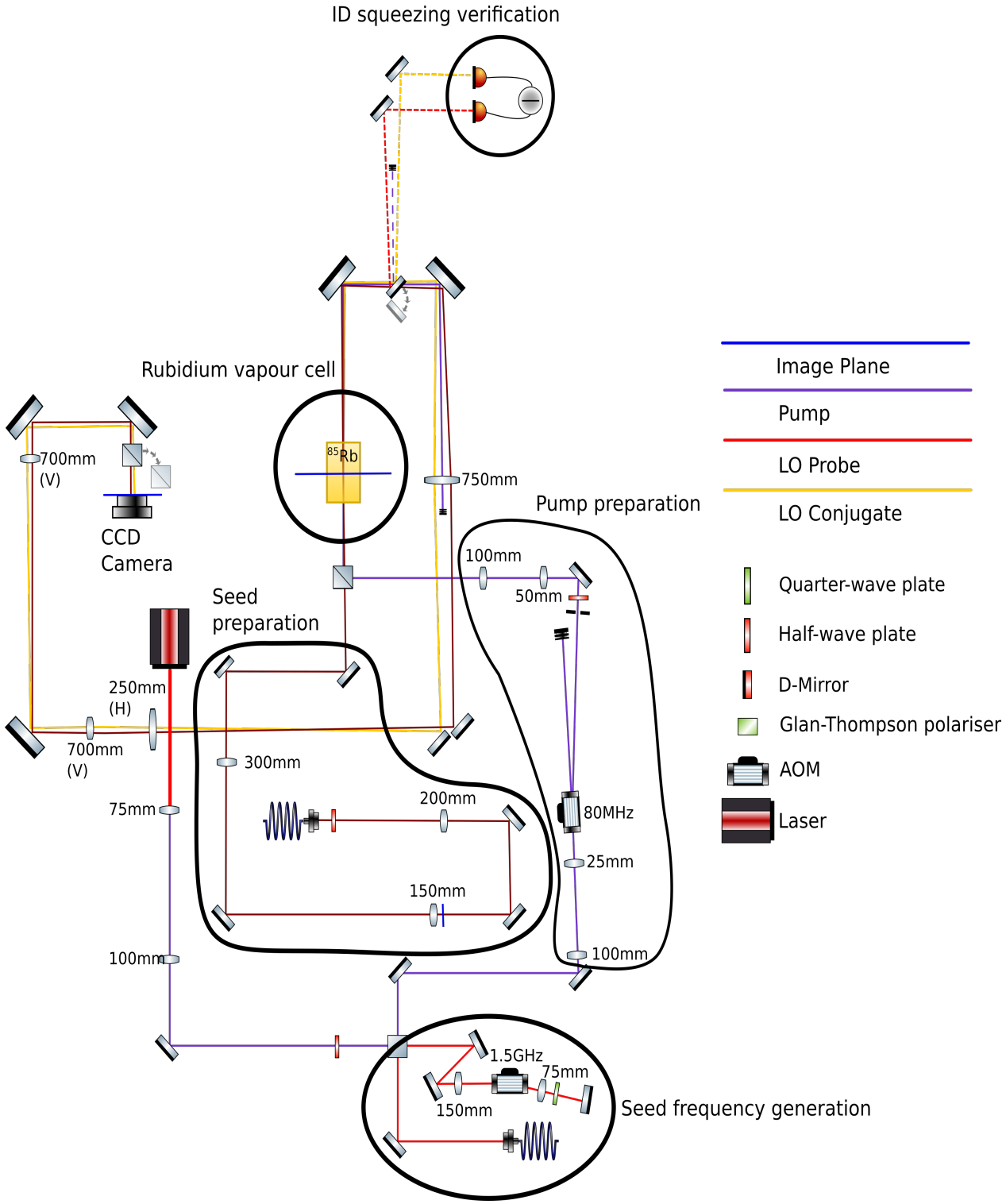

Figure 6.3: Experimental set up for measuring MSM squeezing.

As the CCD was 1024 by 1024 pixels, dividing this into 16 slices gives each slice a y dimension of 64 pixels, and a resultant shifting time of ∼200µs. This provided a ∼5kHz frequency of images acquisition, a rate clearly adequate for avoiding low temporal frequency noise in our images. The exposure time was then set to 7µs, reasons for which are discussed later. Further to this, the CCD was also be split down its centre, separating each slice into smaller slices with a x dimension of 512 pixels. The beams were then directed onto either side of this central divide, allowing their intensities to be easily distinguished and separated. Though this avoids the low temporal frequency intensity noise affecting each frame, differing frames will display differing noise as it takes time to digitise each frame and read it out. This is shown in Figure 6.4, when reading out the frame after filling it with data.

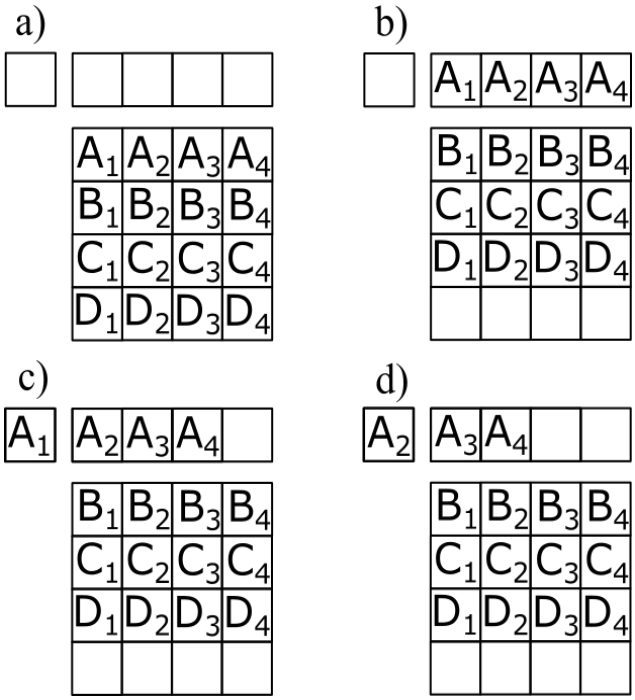

Figure 6.4: The read out process of the camera. Diagram a) shows the full CCD, while diagram b) shows the first line of lines being loaded out of the CCD. Diagrams c) and d) then show how the loaded row of charges are digitised individually.

Repeating the entire process is thus delayed somewhat by the camera's operation, as the digitisation process must occur before the next frame can be taken. Furthermore, the camera had options for slow and fast readout, the former of which provided a digitisation time of $\sim$5s with a 3 electron reading error, and the latter of which provided a digitisation time of $\sim$1s with a 9 electron reading error.

Given that the beams are typically quite bright (in excess of 40000 photons), a 9 electron error is considered negligible. Hence the fast readout speed was chosen to lessen the time between frames, though these delays were still of the order of 1s. As such, each frame of data was taken $\sim$1s apart, which would introduce low frequency noise from laser drifting and similar. This issue is avoided by the QNR equation however, which normalises the noise in each frame with respect to the QNL. This normalisation ensures that only the relative noise in each frame is considered, allowing averaging across the frames without the variation between frames being influenced by low frequency noise.

Despite these efforts however, other noise sources persist within the image data, such as the issue of spatial DC noise. In Section 5.3 the use of a spectrum analyser with a zero span mode at high enough frequency avoided temporal DC noise. In contrast, here we forgo the luxury of a zero span mode and defer to the usual operation of a spectrum analyser, displaying the intensity difference noise as a function of spatial frequency across some spatial bandwidth (the Spectral Power Distribution, albeit in space).

This approach is implemented in our equation for the $\mathrm{QNR}_{dB}(k_y, k_x)$, and allows observation of squeezing beyond the lower spatial frequencies associated with the DC noise. As such, the $\mathrm{QNR}_{dB}(k_y, k_x)$ will exhibit sub-zero noise at spatial frequencies that are squeezed, indicating the experiment's success.

As mentioned at the end of Section 4.1.1, though the pump beam is an essential part of the 4WM process and generation of correlated signal beams, without adequate blocking, residual pump can easily ruin measurements of squeezing. To show this, a set of data was taken with

the probe beam blocked and just the pump passing through the cell and optical system. A single frame of data was then captured by the camera for a range of different pump powers, with each frame being analysed by the QNR_{dB} equation. One such frame and its noise spectrum is presented in Figure 6.5.

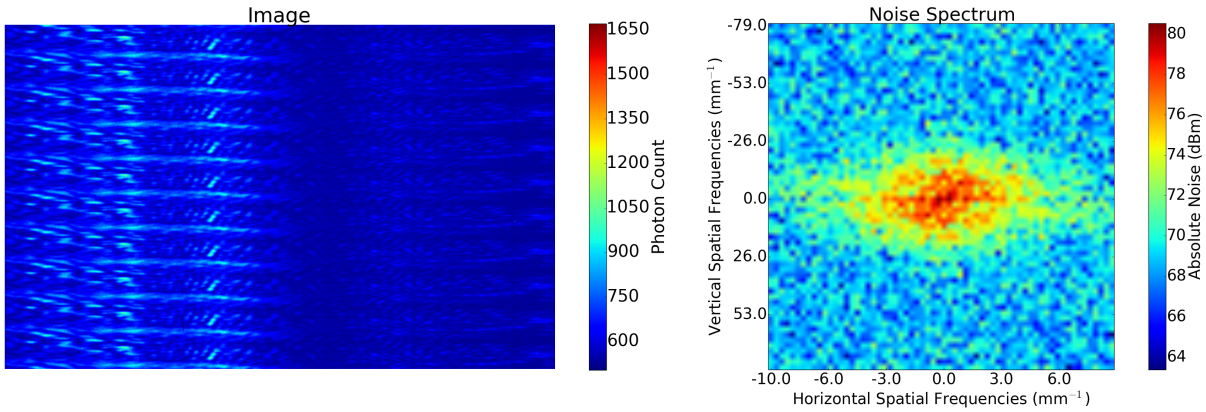

Figure 6.5: A single CCD frame of pump data (left) and the centre of its noise spectrum (right). This frame was captured by exposing for 3µs.

Referring back to the radial averaging algorithm, these frames of data were analysed using the radial average of circular regions at the centre of their noise spectrum and at the bottom right of their noise spectrum. These radial averages thus give a measure of the low spatial frequency noise and the shot noise of the pump in these frames, respectively. These averages can then be plotted against the pump power, giving a measure of how the DC and shot noise of the pump varies with its power, as in Figure 6.6.

Given the logarithmic nature of these results, it is clear that the variance of the pump scales exponentially with pump power. As such, the pump does not need to be as bright as the signal beams to begin to drown out the signals' noise. Previously the pump's intensity was asserted to be brighter than the probe and conjugate, to the point where it affected the polarisation equations in Chapter 4 and in order to maximise the generation of probe/conjugate correlations. Clearly its noise must be removed from the results in order to observe the signals' noise clearly,

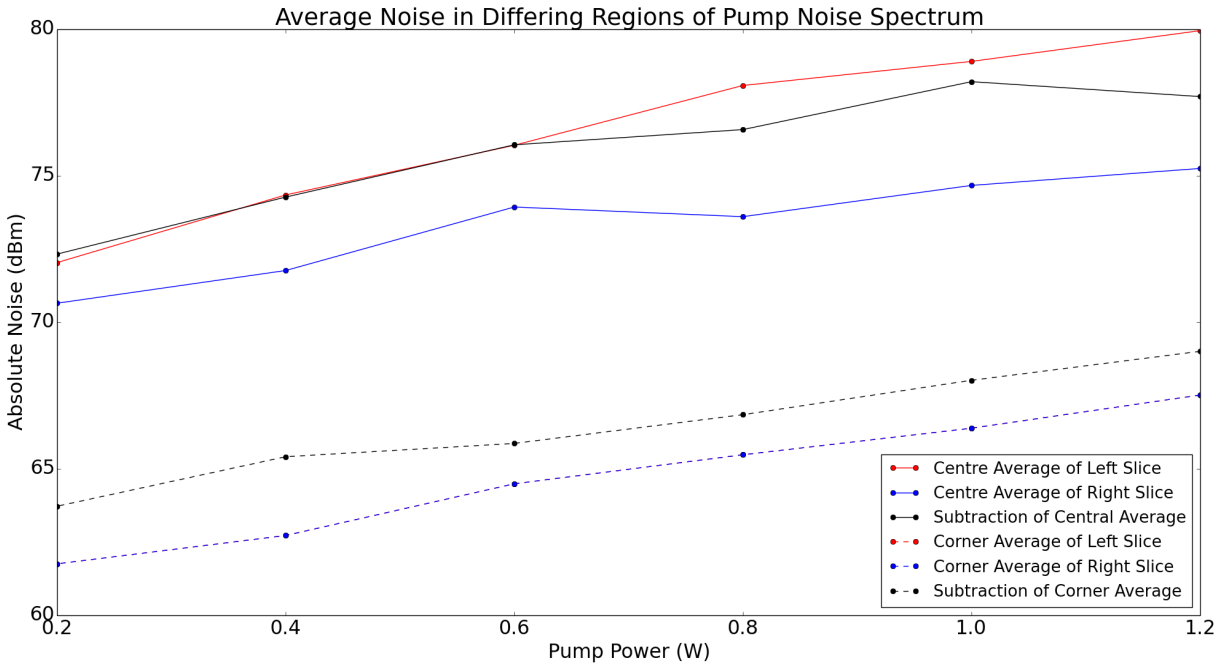

Figure 6.6: Average of circular regions of noise values encompassing the DC frequency (solid lines) and encompassing a point at the bottom right (dotted lines) of the noise spectrum in Figure 6.5. These circular regions had a radius of 5 pixels. Given the logarithmic scaling, this plot shows that pump noise varies exponentially with pump power.

especially as its noise is seen to increase exponentially with its power.

To begin solving the pump issues, a beam block was placed in the pump's post-cell beam path. This is one of the factors influencing the post-cell imaging system, as shown in Figure 6.7. We first note the astigmatic imaging system. This was implemented to reshape the beams to cover a larger portion of the slices on the CCD. The beams were magnified by a factor of $\sim$7 in the horizontal direction. This is to increase the number of photons capable of being detected, increasing the signal and shot noise as much as possible in an attempt to lift these noises away from the pump noise. Additionally, focussing the such large numbers of photons onto smaller areas of the slice hits the saturation limit of the CCD. Furthermore, this magnification also improves the spatial frequency resolution in our analysis in Equation 6.1, and further improving the statistics of our measurements.

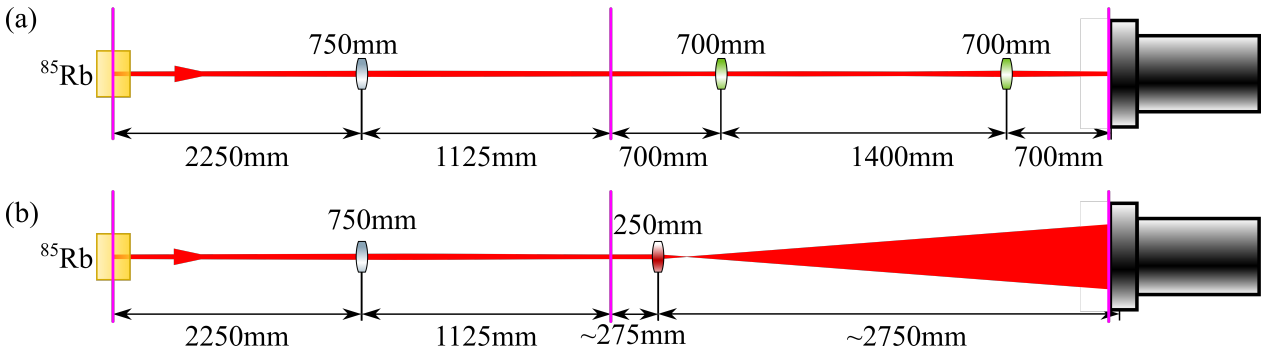

Figure 6.7: Post-cell Imaging System, showing focal lengths and distances, including image planes in pink. Diagram a) shows the optical components for the vertical imaging, diagram b) shows the optical components for the horizontal imaging. The shared f=750mm lens was plano-convex lens. The horizontal cylindrical lens was 6cm by 6cm, the vertical cylindrical lenses were 3cm high by 3.2cm wide. This diagram is somewhat simplified as in the set-up in Figure 6.3, the beams do not pass through the centre of the optical components. Adapted from [67].

Further to this, the size of the majority of the optical components and the distance between them were all chosen to preserve the signal beams' correlations while allowing the pump to be more effectively. As the diameter of the probe is 1.8mm and the diameter of the pump is 2mm in the cell, and the angle between them ∼6mrad, an extended beam path was required to separate the probe and conjugate from the pump.

Blocking the pump with insufficient separation results in infringement on the probe and conjugate given their size and angular divergence, and as this block is placed in the far field, any clipping of the beams at this point removes spatial frequencies from the probe and conjugate. Intuitively, this directly affects and impairs the squeezing measured by the spatial frequency spectrum analysis, and so must be avoided when blocking the pump. For this reason, the pump block was introduced at the first post-cell lens, allowing the beams 2.25m in which to separate to a maximum of 6mrad × 2250mm ≈ 13mm between pump and either signal. Blocking after this lens would be inefficient, given that it is plano-convex and would converge the beams, decreasing this separation.

This issue of clipping spatial frequencies is also the reason for the large optical components,

with all mirrors, the f=750mm lens and f=250mm horizontal cylindrical lens being 2"Ø (50.8mm) in diameter. Given the 26mm distance between the probe and conjugate, this allowed for adequate collection of the far field probe and conjugate fields, preserving their Fourier frequencies.

As previously mentioned, the first post-cell lens is plano-convex, and results in the convergence of the probe and conjugate when imaging their near field. As this near field is located in the centre of the cell, where they are amplified at the same points and so are overlapped, this presents a problem for the imaging system.

Any attempt to image the beams using only lenses will result in the convergence of the beams into their original overlapped state, making subtraction impossible. To remedy this, a pair of "twin mirrors" are introduced after the first post-cell lens, close to the near field. These mirrors are used to adjust the signals' beam paths and separate them in the near field, allowing them to be measured separately, and so subtracted.

To capture these beams on the camera, they must be appropriately pulsed to coincide with the camera's exposure time. For this, the pre-cell AOMs in the probe and pump preparation areas of Figure 6.3 are used. Pulsing the RF supplied to these respective AOMs thus pulses either beam, and so provides pulsed signals.

While correct in theory, these implementation requires some modification in order to function as required. To begin the pulsing, the RFs supplied to the AOMs must saturate their output power. If unsaturated, amplitude noise on the RF will be transferred onto the intensity of the deflected beams. As such, two RF chains are implemented to ensure that the supplied RF satisfies this criteria, as shown in Figure 6.8.

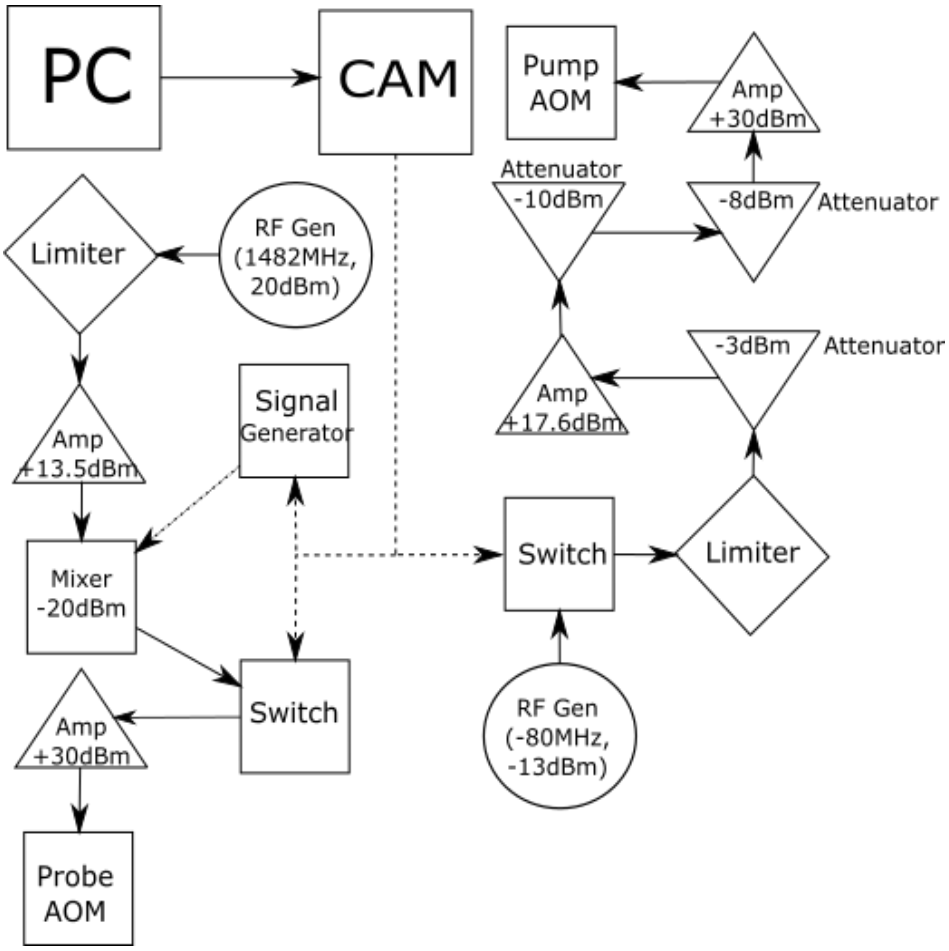

Figure 6.8: RF component chains used in pulsing and saturating the AOMs. The gains and attenuations of the RF are given in their respective components. The solid lines are RF, the dashed lines are TTL and the spotted line is a Gaussian-shaped voltage signal. The component details are specified in Appendix D.

As can be seen from Figure 6.8, the set-up utilised a PC to command the camera, which in turn gave a TTL signal, the timing of which was user specified. In this experiment, the camera was set to output this signal whenever it was exposing. This logic signal would then simultaneously activate switches in either RF component chain, allowing the RF through to the AOMs, effectively pulsing the beams. There is a major discrepancy between the two

chains however, as the probe chain includes a signal generator and a mixer component. These components are introduced as there are constraints on the exposure time and durations of the pump and probe, due to the nature of the 4WM process and its transient effect, shown in Figure 6.9.

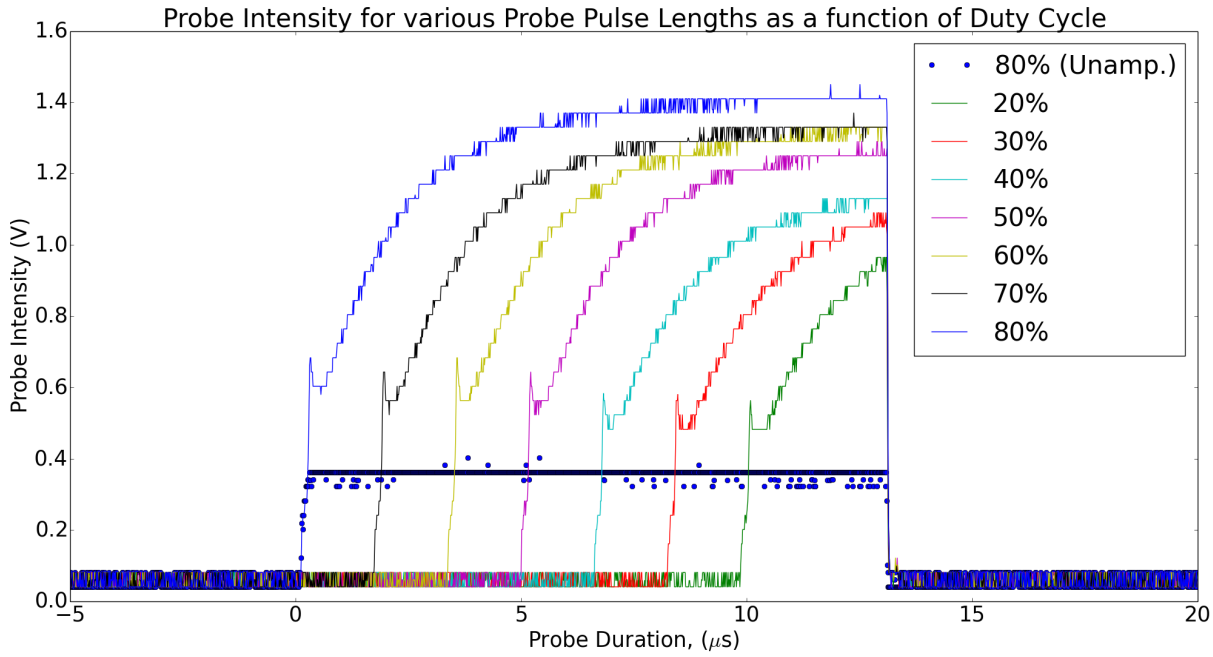

Figure 6.9: Transient effects on the probe's amplified intensity over a 7µs period with the probe duration being changed as a function of duty cycle.

The transient effect is the result of an insufficient number of pre-pumped Rb85 atoms within the cross-section of the pump and probe, resulting in a lower, and even time dependent, gain on the signal beams. To resume with the intended measurements, it is clear that this effect is to be avoided.

As such, compromises are required on both the exposure time and the probe duration. Given the varying gain, the probe is required to be confined toward the end of the exposure time. This is the main reason for the inclusion of the signal generator and mixer in the probe RF

chain. Concurrently, the exposure is required to be long enough to allow for pumping of the Rb85 atoms, while still short enough to avoid additional, and unnecessary, technical noise. This is amended by observing that the transient effect appears to cease given an adequate pumping time, which from Figure 6.9 is ∼7µs, hence its previous specification as the exposure time.

In addition, a signal generator was included to shape the RF pulse into a Gaussian, and was thought to improve results as in [77]. Given that a top hat RF pulse would introduce additional frequencies into the signal beams' bandwidth, as the Fourier transform of the pulse in time would convolve the signals with a sinc function. Alternatively, using the signal generator to provide a Gaussian RF signal would thus preserve the probe pulse's shape in Fourier space and so retain its original bandwidth.

The signal generator used in this experiment is detailed in Appendix D. It is capable of generating a custom signal given a .csv file with a length of some multiple of 128 elements long. This file was generated with a Python script by considering 128 elements to be a µs, taking values from zero to seven multiples of 128 and generating a Gaussian approximately half way into the seventh multiple.

This Gaussian was then raised to the power of 4, to narrow its width to less than 128 elements, making the final pulse generation ∼1µs. The final signal would hence be 6µs of zero, and 1µs of Gaussian. The narrowing of the Gaussian was considered necessary, to ensure the signal was confined to the end of the camera's signal. As such, the pulse sent to the probe AOM would not be too long as to outlast the pump duration and suddenly terminate nor start too early as to suffer gain variation due to transient effects at the beginning of the pulsed pump. As the AOM deflects pump light by an angle dependent on the RF supplied to it, an RF of -80MHz was selected as being adequate in deflecting pump light such that it was separable from other orders over not too long a distance (in this case, this distance was ∼40cm). To compensate for this and re-establish the double-Λ transition in the Rb85 atoms, as in Section

5.3.1, the probe RF was set to 1482MHz in this experiment.

Having specified the experiment and its set-up, we now consider its typical operation. With all relevant equipment and lasers turned on, an independent measurement of intensity difference squeezing was taken using the verification area as shown in Figure 6.3. Once squeezing was confirmed, all extraneous light sources were either extinguished or covered, and the experiment was curtained off. All air conditioning, flow boxes and other atmospheric disturbances were shut off or shielded. These precautions were taken to avoid adding unnecessary noise and instability to the signal beams.

The camera was then prompted by PC commands to begin its cooling procedure. This would allow the camera to reach its advertised qauntum efficiency, achievable at a temperature of -70°C. After this, the PC would initiate the camera's Kinetics mode procedure: the camera shutter would open, taking ∼8ms, and the exposure/shifting process cycle would begin. During each exposure, the camera output a TTL signal to the AOMs' RF switches. This would effectively pulse the beams in time with the exposure periods.

Once the CCD was filled with image data, the camera would close its shutter and digitise the data, then pass it to the PC. This set-up was continuously ran via a loop in the Python script on the PC. When left to continuously collect data, it was found that additional optimisation was required. Due to the lengthy nature of the beams propagation, the twin mirrors required manual adjustment to place the beams at the exact same points in their respective slices. The centre of their slices were considered the most obvious place to shine them. This would also minimalise losses from the edge of the CCD, and spillage of either beam onto the other's slice.

This adjustment took the form of running the camera and plotting the results to the PC screen, adjusting one of the twin mirrors and observing the change in radially averaged noise. This noise improved the closer the beams were to the centres of their respective slices, as they were more overlapped when subtracted and less of each beam contaminated

the other slices. Finally, a magnet-mounted polarising beamsplitter was placed just before the camera as a final attempt to remove residual/undesired light from the results. As it is magnet-mounted, this beamplitter was easily removed and allowed for additional collection of results for comparison quickly.

6.2 Results & Analysis

After conducting the experiment, obtaining the data for either beam from the camera and dividing the probe and conjugate intensities into separate arrays, the first 4 and last 2 slices were discarded from both. This was due to the 8ms shutter opening and closing time, which contaminated the results. More slices were discarded from the first slices as these slices were the first to be taken, and so are on the CCD for longer, resulting in longer background and residual pump exposure leading to unwanted noise. After this, the spatial frequency spectrum analysis from Equation 6.1 was then applied.

Using this analysis, the data from the camera could be examined through its spatial frequencies. Where squeezing was present, a clear sub-zero region would be found. To ensure that squeezing would be detectable, a set of results were taken where the probe was blocked to observe unavoidable excess light from the pump. To compare to the probe noise, a number of excess light noise spectra were also calculated by spatial frequency spectrum analysis, as shown in Figure 6.10.

The noise in the subtracted spectrum of this frame is low, with a peak noise of ∼84dBm at the DC frequency, falling to around ∼80dBm in surrounding frequencies before fading to below that further out. By comparison, the camera results, an example of which are shown in Figure 6.11, show an absolute shot noise of ∼88dBm.

This allows for ∼8dB of clearance below the subtracted probe and conjugate's shot noise in which to detect squeezing. The results in Figure 6.11 are the most extensive set of data taken

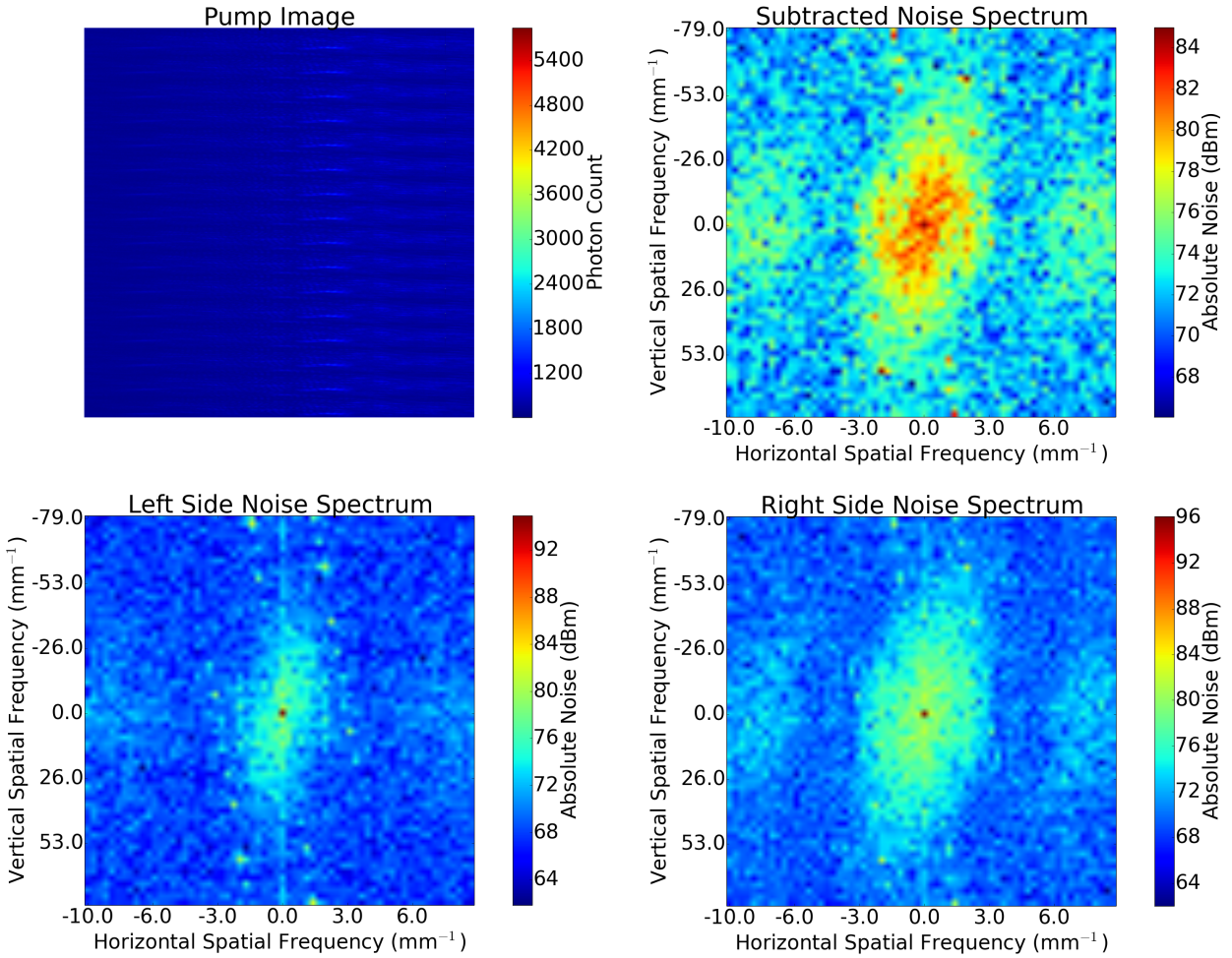

Figure 6.10: A single frame of camera data, with the probe beam blocked. The spectra here are calculated through spatial frequency spectrum analysis. The subtracted spectrum (upper right) is presented as a display of how much noise the excess light contributes to the subtracted probe and conjugate spectrum. This sets a limit to how much squeezing can be detected, as it cannot be detected below this subtracted spectrum's noise. The lower two are to show the noise of excess light in the probe and conjugate slices separately. This data was taken with no beamsplitter in front of the CCD.

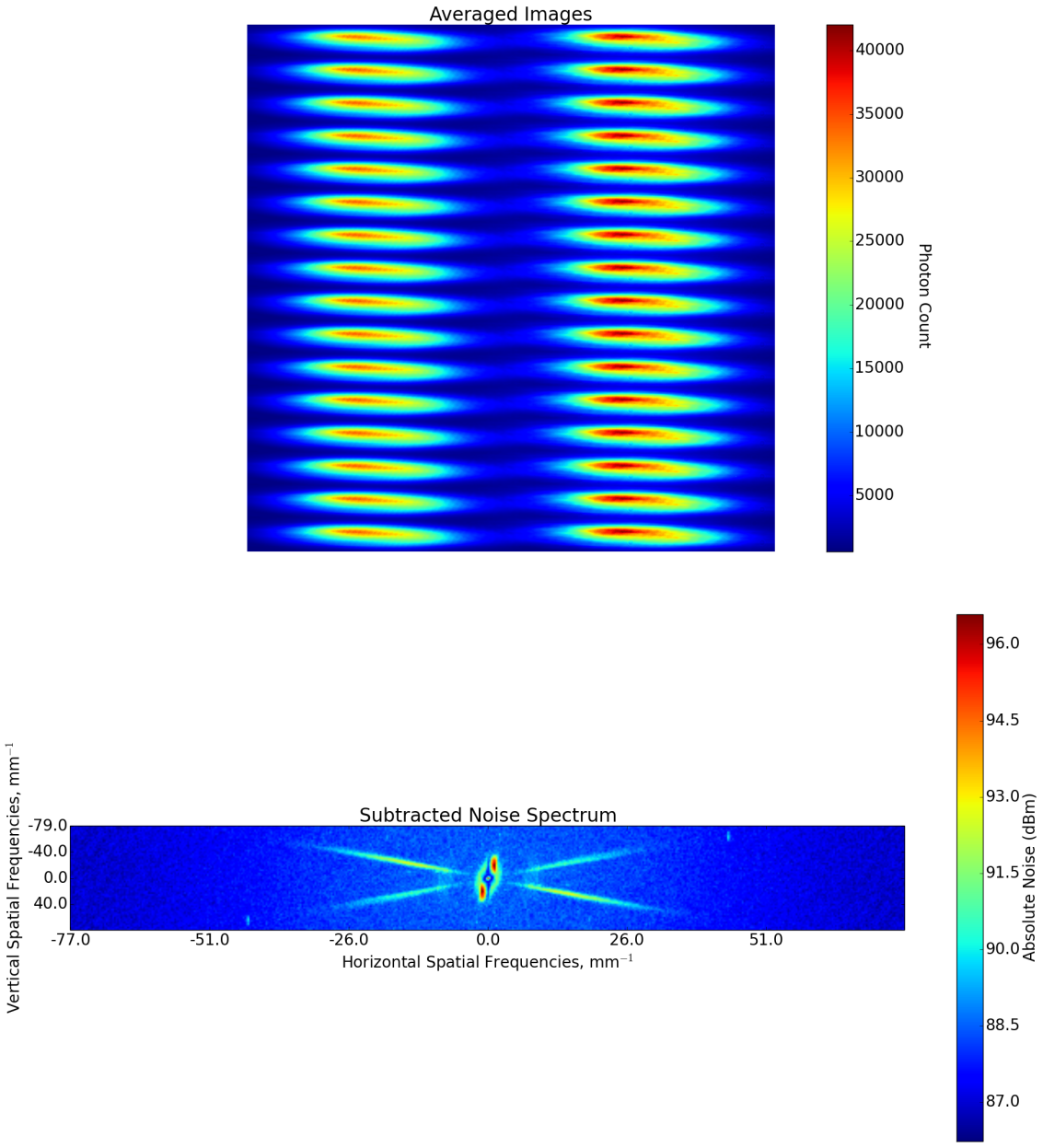

Figure 6.11: Analysis of 42 frames of data from CCD camera, taken with a two photon detuning of 1481MHz. These results had no beamsplitter just before the camera. An independent squeezing measurement using the verification set-up in Figure 6.3 gave a reading of -4.3dB. The polarising beamsplitter, intended to remove excess light, was not implemented for these results.

with 42 frames, and are representative of MSM squeezing results in this thesis.

The results in Figure 6.11 were taken after an extensive manual optimisation. After arranging the pre-cell system to optimise the gain, the post-cell required precise alignment due to the length of the imaging system, supplemented by optimisation alignment using the twin mirrors. This optimisation placed the beams onto the centre of their respective slices as close as could be determined from the resulting data.

Radial averaging was then implemented to investigate the noise spectrum further. Figure 6.12 shows the circular path algorithm used for sequentially larger radii, giving a measure of the average noise from DC out to the higher frequencies.

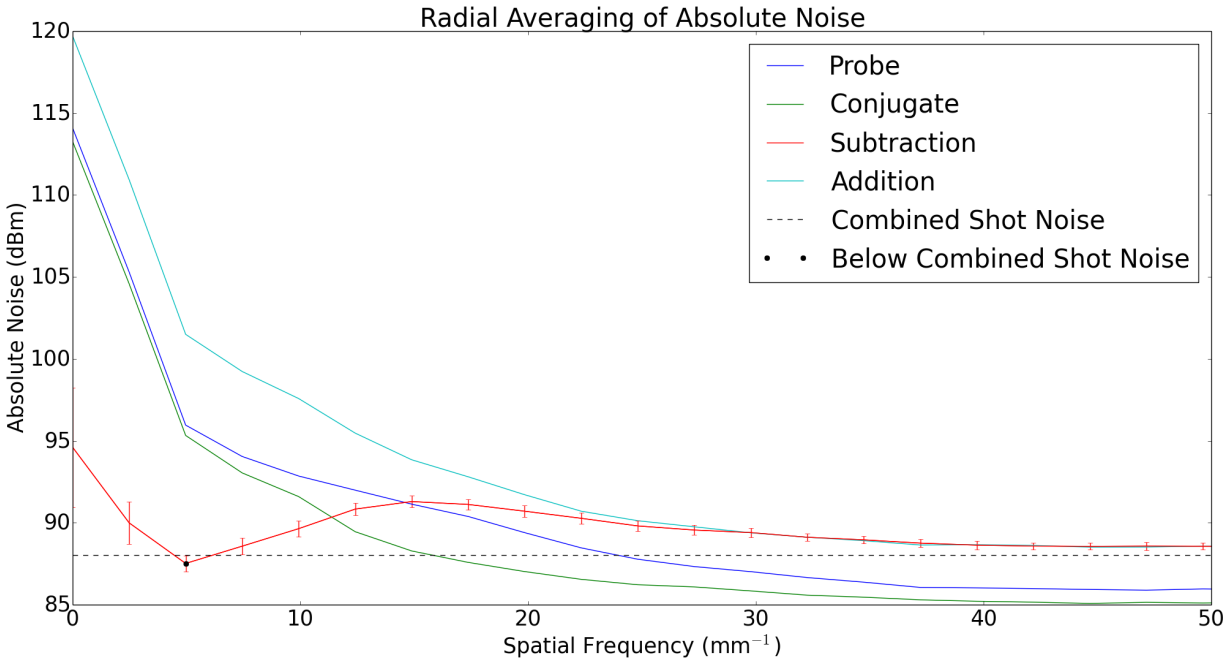

Figure 6.12: Radial Averaging plot, showing the noise about the DC in the noise spectra of the probe and conjugate separately, then of them added together and finally subtracted. The subtracted spectrum radial average is of most interest given its sub-shot noise points. The error bars included here are the standard deviation of the radial averages of each frame in the set of 42.

The red error bars on the subtraction results in Figure 6.12 are the standard deviation of this average noise. These error bars imply that for the most part, these noise values do not fluctuate much over the 42 spectra, at least not for higher spatial frequencies. A single point, marked by the black dot in Figure 6.12, shows that a single set of spatial frequencies yielded squeezing. The radius corresponding to this sub-zero noise average is then used to plot the constituent noise values at their respective points in the noise spectra, as shown in Figure 6.13.

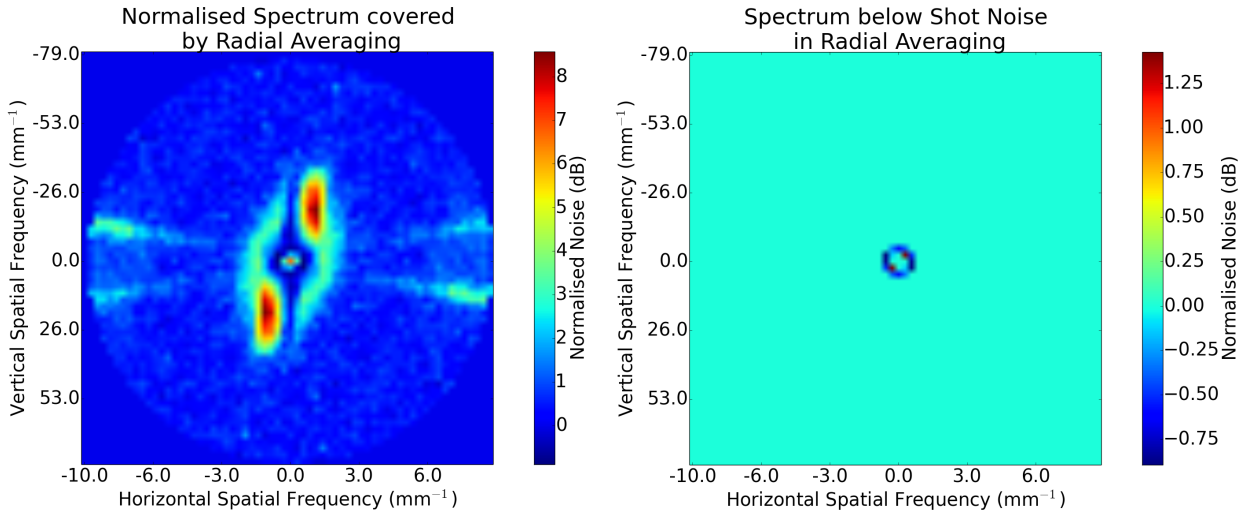

Figure 6.13: Magnified and normalised view of the noise spectrum of the data in Figure 6.11. Also filtered firstly with respect to the spectrum covered by the radial averaging algorithm, then with respect to the sub-zero points in Figure 6.12. The maximum squeezing achieved is ∼-0.75dB.

As can be seen from Figure 6.13, there is a clear, albeit single pixel width, circle of squeezed spatial frequencies in these results, displaying ∼-0.75dB of squeezing. The number of squeezed spatial modes in these results is 8, with vertical frequencies $\pm 4.96\text{mm}^{-1}$, $\pm 2.48\text{mm}^{-1}$ and 0mm^{-1} and horizontal frequencies $\pm 0.60\text{mm}^{-1}$, $\pm 0.30\text{mm}^{-1}$ and 0mm^{-1}. The 0mm^{-1} in these spatial frequencies corresponds to the vertical and horizontal DC, corresponding to regions with the same height or width as the slice. The total number of coordinates on the

circle in these results is 8, which would be the number of spatial modes.

It is noted that there is also an unusual amount of noise surrounding these spatial frequencies. The noise on the DC and surrounding frequencies falls away quickly to squeezed values, around -0.75dB below shot noise. At such points, these frequencies should then be sufficiently far from DC that no technical or excess noise is present. Yet, despite this, the noise increases again, forming noise lobes of ∼90dBm surrounding the supposedly squeezed frequencies. As this noise has no obvious source, it is considered anomalous.

The position of this noise would suggest that the achieved squeezing may potentially be a glimpse of a larger region of squeezing, unseen due to this anomalous noise. To investigate, further results were taken, this time utilizing a beamsplitter just in front of the camera to observe whether the results in Figure 6.11 could be improved. Again, data was collected with the probe blocked, to observe whether squeezing would be compromised by any other noise sources: The difference in noise between Figure 6.10 and Figure 6.14 is small, ∼1dB, with the beamsplitter results being less noisy. This small change is unlikely to overcome the bulk of ∼4dB noise we have observed. This was verified by taking 38 frames of signal data. These results are shown in Figure 6.15.

These results show a similar issue as the results in Figure 6.11, which appears to be a cloud of anomalous noise surrounding a region of potential squeezing. From these results however, it appears that the beamsplitter has displaced the noise from the spatial frequencies it inhabited in the original results. As such, this anomalous noise now covers frequencies within the observed ring of squeezed values from before, disrupting our radial averaging algorithm. This can be seen in Figure 6.16.

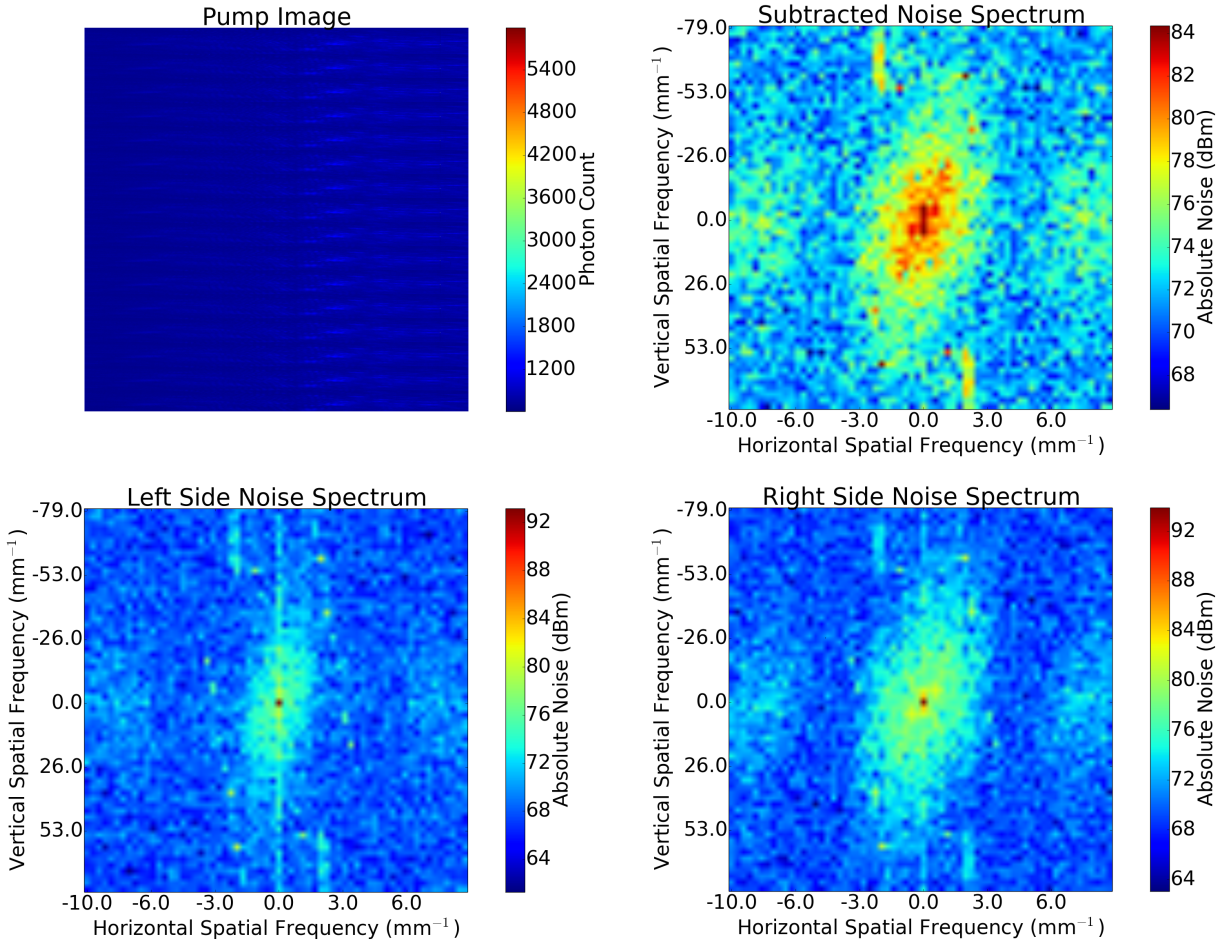

Figure 6.14: A single frame of camera data, with the probe beam blocked and a beamsplitter directly in front of the camera. The spectra here are calculated using the spatial frequency spectrum analysis. The subtracted spectrum is presented as a display of how much noise the excess light contributes to the intensity difference noise spectrum. The lower spectra are included as a measure of extraneous noise in the probe and conjugate slices separately.

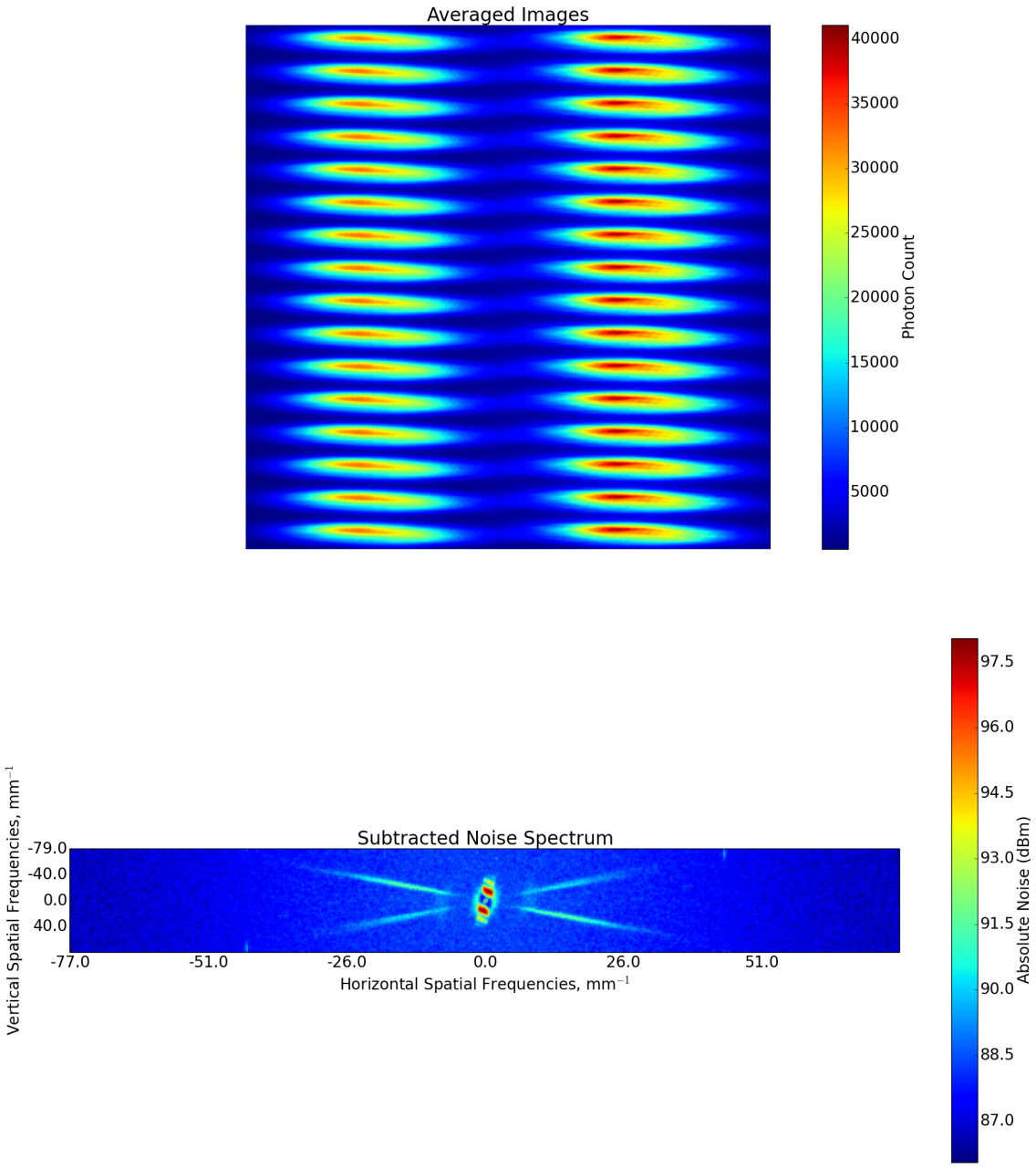

Figure 6.15: Analysis of 38 frames of data, taken at 1481MHz two-photon detuning with 3 µs exposure durations and a polarising beamsplitter placed before the CCD. The noise spectrum was calculated using the spatial frequency spectrum analysis.

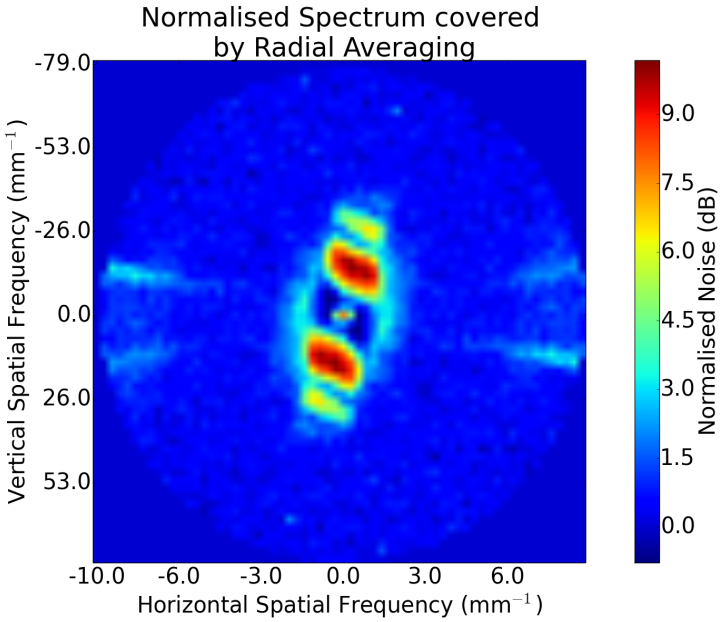

Figure 6.16: Magnified and normalised view of the noise spectrum in Figure 6.15. This was also filtered to include only the noise covered by the radial averaging algorithm. However, due to the change in the distribution of noise, the radial averaging algorithm found no circularly arranged noise values and so could not filter out squeezed spatial frequencies.

As such, it appears that any benefit of the beamsplitter is countered by some effect it introduces that distributes the noise differently within the noise spectrum. In doing so, it prevents the radial averaging algorithm from working. As removal of excess light and its noise has proven to be ineffective, the cause of the anomaly was considered to be elsewhere. To this end, the carriers of the intensity difference squeezing, the probe and the conjugate, were examined separately. The noise for the probe and conjugate that produced the results from Figure 6.11 (without the beamsplitter) are shown in Figure 6.17.

As can be seen from Figure 6.17, the probe's spatial frequencies exhibit larger noise for a broader spatial bandwidth surrounding the DC. These spatial frequencies appear to correspond to the same frequencies compromised by the anomalous noise in Figure 6.11. This suggests

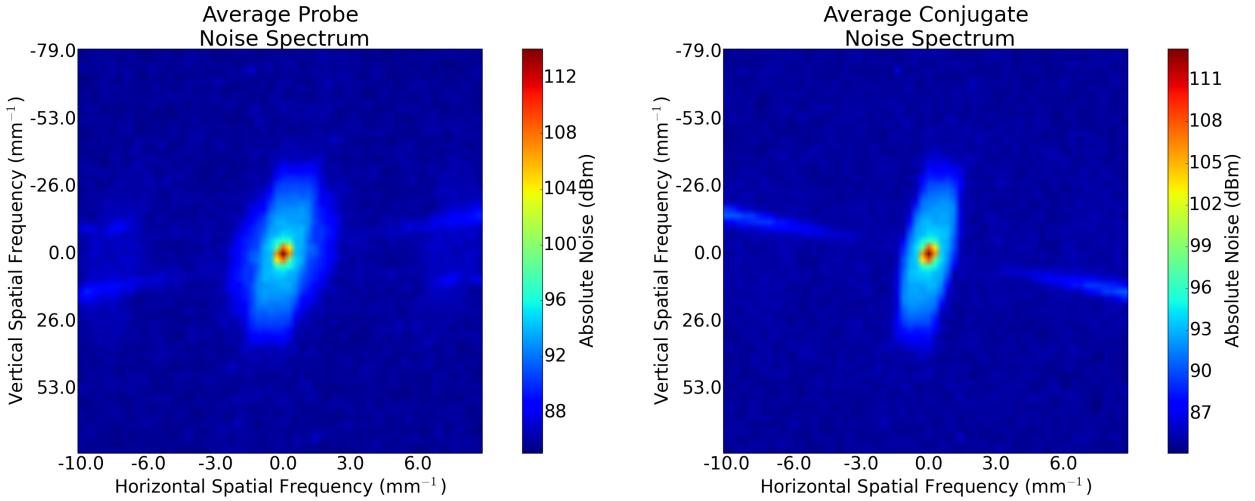

Figure 6.17: Close ups of the centre of the noise spectra of the probe (left) and conjugate (right) from Figure 6.11. These spectra were calculated using the spatial frequency spectrum analysis.

additional noise on the probe is the subversive element preventing clear observation of intensity difference squeezing.

As this noise is on the probe only, we can surmise that the issue is with the probe beam, and must occur after the cell. If the pre-cell probe had issues with anomalous noise, it would be manifest in the conjugate as well, given the conjugate signal beam's dependency on the probe due to the 4WM process. Hence, the probe signal beam must encounter some post-cell component that increases its noise.

Despite this, the post-cell imaging system given in this thesis is not considered defective, as the probe's beam path could require further optimisation beyond the manual adjustment of the twin mirrors and with a metric other than the degree of squeezing possible with this adjustment. To compare, the same analysis is applied to the probe and conjugate beams in Figure 6.15 (with the beamsplitter), providing the noise spectra in Figure 6.18.

The same cloud of noise persists in the spectra of Figure 6.18, though there is no obvious shifting of noise in the spatial frequencies. Given the appearance of severe additional noise, the red blobs, in Figure 6.11 and 6.15, it is possible that additional phenomena/interactions

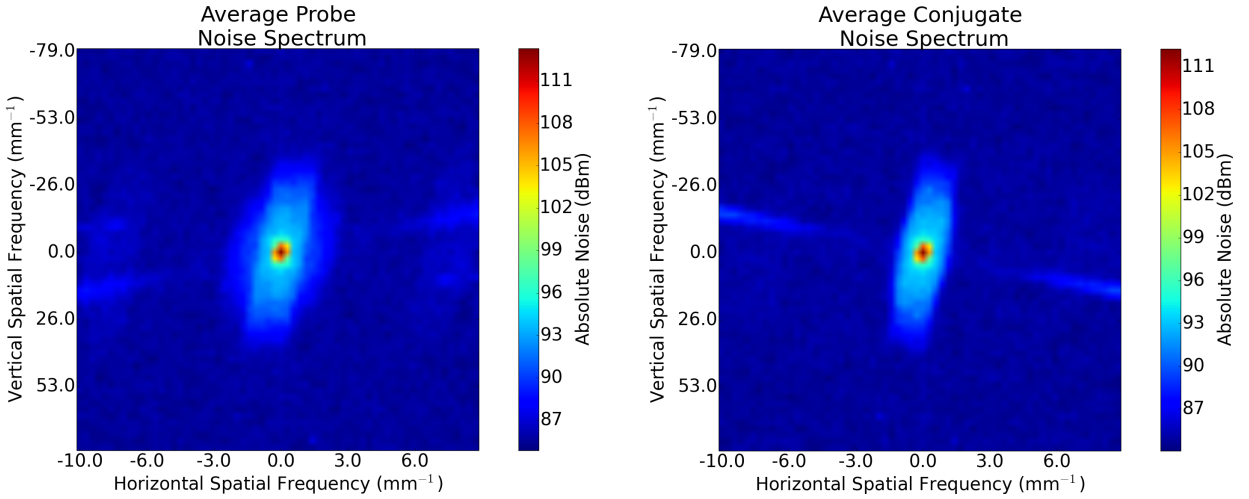

Figure 6.18: Close ups of the centre of the noise spectra of the probe (left) and conjugate (right) from Figure 6.15. These spectra were calculated using the spatial frequency spectrum analysis.

are influencing the noise. Both this anomalous noise and the indication of squeezing in these results will be investigated further in the next section.

6.2.1 Alternative Analysis

Though the spatial frequency spectrum analysis is sufficient to observe squeezing, alternative analyses were considered and implemented as a means of verifying the squeezing it displayed. Furthermore, these analyses explore the behaviour of the noise and how it reacts to a variety of computational manipulations.

The first such analysis was a beam displacement algorithm which digitally moved one of the beams then conducted the spatial frequency spectrum analysis and radial averaging algorithm. Due to the inherent role of the Fourier transform in the analysis, the displacement algorithm used the Fourier shifting theorem to displace one of the beams in Fourier space:

$$\mathcal{F}[I(x \pm x_0, y \pm y_0)] = \mathcal{F}[I(k_x, k_y)]e^{\pm ik_x x_0 + k_y y_0}.$$

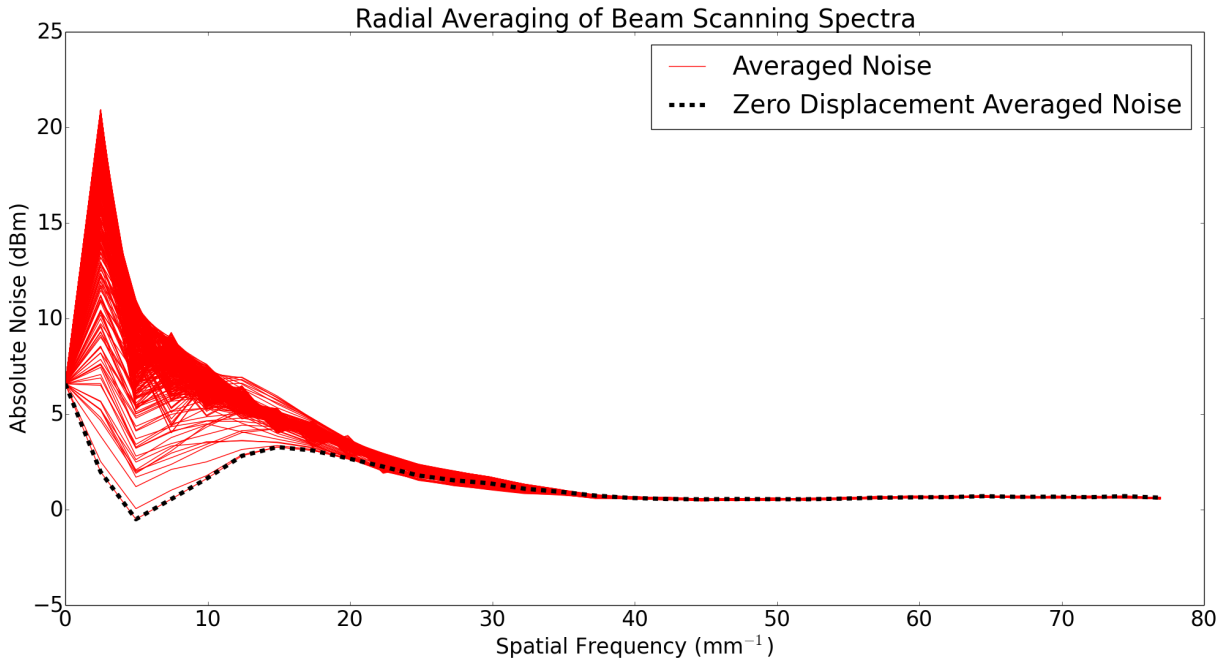

Figure 6.19: Beam scanning of the 42 frames of data in Figure 6.11. The probe beam was shifted by incremental displacements, subtracted from the conjugate, then analysed. This figure shows the radial averaging of each resultant noise spectrum, displaying how the noise changes as the probe is displaced.

The beam was shifted by a single pixel at a time in real space, then the spatial frequency spectrum analysis and radial averaging were applied. This procedure was then repeated until the beam had been moved to all positions within the slice. To speed up the process and avoid erroneous/nonsensical spectra, the algorithm was also designed to move the beam only until its $1/e^2$ radius met an edge of its slice. This would avoid moving the beam off one side of the slice and onto the opposing side.

This analysis was applied to observe whether the probe could be digitally overlapped with the conjugate better than what had been achieved physically. Additionally, it was attempted to observe any changes to the anomalous noise. The beam selected for displacement was the probe, starting first with the results without a beamsplitter, giving the results shown in Figure 6.19. The results of Figure 6.19 are depicted as red for a radial averaging involving

a displaced beam, and dashed black for the original radial averaging where there was no displacement. As can be seen, none of the displaced results improves upon the original positioning of the beams since none of them produce a lower radial averaging. This infers that the squeezing in the results cannot be improved further by adjusting beam position. It is also noted that the anomalous noise does not dissipate either, and worsens in some instances. The same approach was applied to the results in Figure 6.15 (with beamsplitter), as shown in Figure 6.20

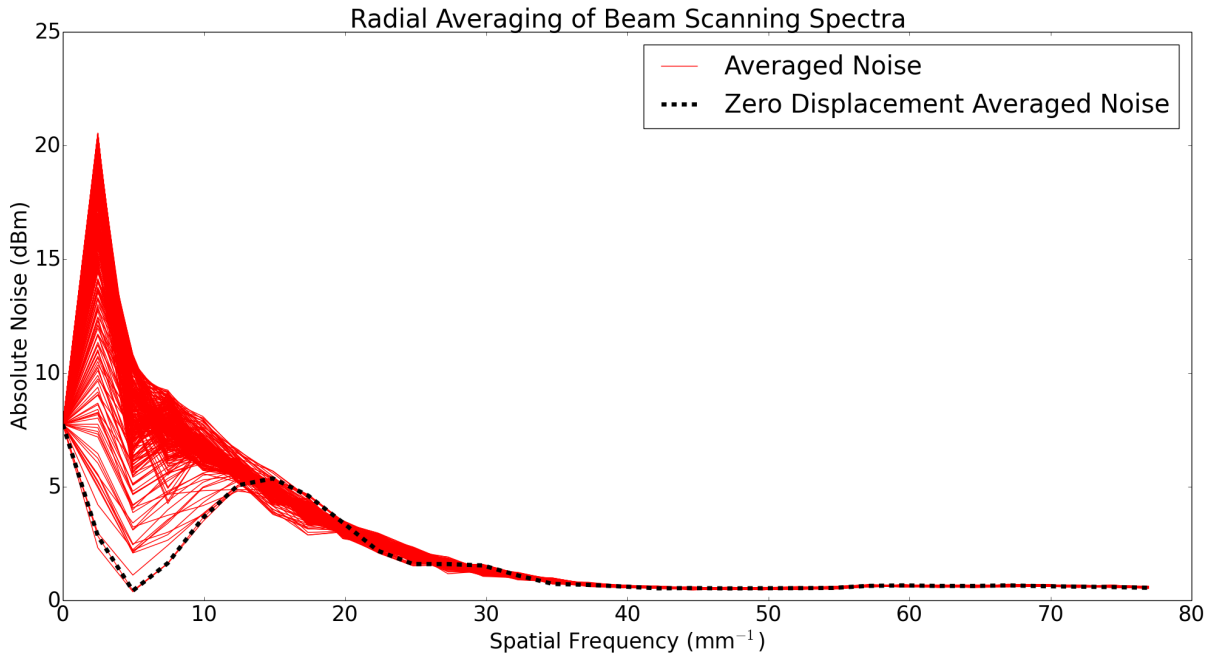

Figure 6.20: Beam scanning of the 38 frames of data in Figure 6.15. Each red line represents the radial averaging of a noise spectrum, each spectrum being calculated from a set of probe and conjugate images where the probe is displaced to different positions. This then shows whether there is any difference between the probe and conjugate positions that disrupts the squeezing.

These results indicate a similar conclusion, that displacement of the probe fails to yield better squeezing. The original positions of these beams is hence the optimum for these

results. However, these same results do indicate a lowering of the anomalous noise, around the 15mm^{-1} mark. A number of displacements appear to reduce this noise, which implies that the beamsplitter used in these results may be working as intended, but has itself displaced the beams, counteracting its efforts.

Another set of analyses were considered to further process the results. These algorithms intended to realise a similar procedure as the conduit experiment's slits scanning from Section 5.3. To do so, digital slits were placed on and moved across the beams by lifting sections from them, observing the noise of the intensity difference between them at each point. The noise analysis in this case deviated from the spatial frequency spectrum analysis, instead opting for a process yielding a single value for each slit position in the vertical and horizontal directions:

$$\mathrm{QNR}_{dB}(y) = 10\log_{10}\left(\left\langle \frac{\mathrm{Var}_s(\sum_{x'=0}^{w}(\sum_{y'=y}^{y+\mathcal{Y}} I_p(y',x') - \sum_{y'=y_c}^{y_c+\mathcal{Y}} I_c(y',x')))}{\langle\sum_{x'=0}^{w}(\sum_{y'=y}^{y+\mathcal{Y}} I_p(y',x') + \sum_{y'=y_c}^{y_c+\mathcal{Y}} I_c(y',x'))\rangle_s}\right\rangle_f\right) \tag{6.2}$$

$$\mathrm{QNR}_{dB}(x) = 10\log_{10}\left(\left\langle \frac{\mathrm{Var}_s(\sum_{y'=0}^{h}(\sum_{x'=x}^{x+\mathcal{X}} I_p(y',x') - \sum_{x'=x_c}^{x_c+\mathcal{X}} I_c(y',x')))}{\langle\sum_{y'=0}^{h}(\sum_{x'=x}^{x+\mathcal{X}} I_p(y',x') + \sum_{x'=x_c}^{x_c+\mathcal{X}} I_c(y',x'))\rangle_s}\right\rangle_f\right) \tag{6.3}$$

Here the symbols x and y refer to points within the xy dimensions of the slices while y_c and x_c are the centre of the conjugate slice. The symbols h and w are the height and the width of the slices, respectively, while $\mathcal{Y}$ and $\mathcal{X}$ are the height and widths of the slits imposed on each slice.

The symbols y' and x' are the y and x coordinates of each position within the slits, while $I_c(y',x')$ and $I_p(y',x')$ are shorthand for $I_c(f,s,y',x')$ and $I_p(f,s,y',x')$ respectively. Equations 6.2 and 6.3 are depicted in diagrams a) and b) in Figure 6.21 respectively, with vertical scanning shown in diagram a) and horizontal scanning in diagram b).

These formulas thus integrate the sections of the intensity difference within the digital slits in each slice, take the variance of this integral over the slices and compare it to the average

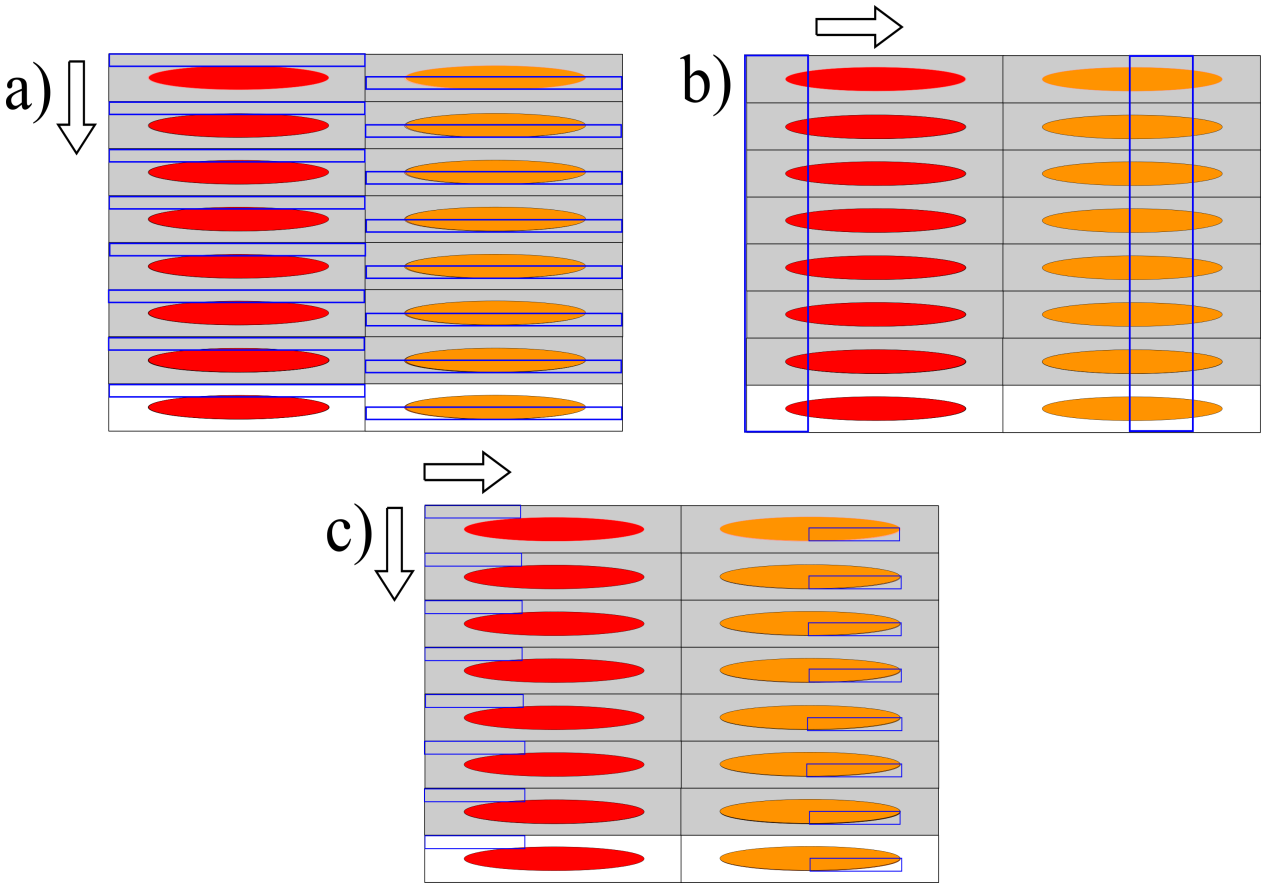

Figure 6.21: The scanning processes, with apertures shown in blue. The direction the slits move in is shown by the arrows next to each diagram. Diagram a) shows the horizontal slits placed on the beams for vertical slit scanning. Diagram b) shows the vertical slits placed on the beams for horizontal slit scanning. Diagram c) shows the windows placed on the beams for entire beam scanning. The directional arrows apply only to the slits on the probe beam, with the conjugate slits remaining static.

total power of the same sections for a range of positions x or y. This process is depicted in Figure 6.21.

Further to this, the x and y points within these formulae do not span the full extent of the respective slice dimensions, as the vertical and horizontal slits already span lengths $\mathfrak{X}$ and $\mathfrak{Y}$ respectively. Considering the full range of x and y points would result in the slits extending beyond the slice (resulting in a runtime error, as this would extend the slits' area beyond the indices of the data array). As these slits also span the entire height or width of slice for the

horizontal and vertical scanning respectively, the resultant QNR expressions are reduced to one-dimensional functions as the slits cannot be moved in directions they fully span.

The slit sizes $\mathcal{X}$ and $\mathcal{Y}$ were determined by taking an arbitrary area of 32 pixels by 32 pixels and shaping it to fit the aspect ratio of the $1/e^2$ radius of the probe beam. The area was chosen as being large enough as to not infringe on the coherence area of the beams. The vertical and horizontal slit sizes were then set to the length and height of this area, respectively. If the area had been smaller, or not shaped to the beams' aspect ratio, it ran the risk of being smaller than the coherence area. This would result in a loss of correlations and so impair and hinder the slit scanning.

This algorithm was conducted firstly on the results of Figure 6.11 (no beamsplitter), with a static slit positioned on the conjugate and a scanning slit moved over the probe. The results are shown in Figure 6.22, for both horizontal and vertical scanning.

As can be seen in Figure 6.22, the QNR of each slit position begins to drop toward the centre of the scanning, where the conjugate slit is positioned. Due to DC noise however, these results do not display squeezing as previous analyses did. The same approach was applied to the results from Figure 6.15 (with beamsplitter), as shown in Figure 6.23.

These results show a similar trend to those in Figure 6.22, with a gradual decrease in intensity difference noise down to where the probe slit reaches the region correlated to the conjugate slit. However, again, these results are DC noise limited and fail to exhibit squeezing. Despite this, both sets of results are good indications of a good positioning of the beams within their respective slices.

The slits where then applied simultaneously to form a window, resulting in a new algorithm, giving a QNR of the form:

$$\mathrm{QNR}_{dB}(x,y) = 10\log_{10}\left(\left\langle \frac{\mathrm{Var}_s(\sum_{x'=x}^{x+\mathcal{X}}\sum_{y'=y}^{y+\mathcal{Y}} I_p(y',x') - \sum_{x'=x_c}^{x_c+\mathcal{X}}\sum_{y'=y_c}^{y_c+\mathcal{Y}} I_c(y',x'))}{\langle \sum_{x'=x}^{x+\mathcal{X}}\sum_{y'=y}^{y+\mathcal{Y}} I_p(y',x') + \sum_{x'=x_c}^{x_c+\mathcal{X}}\sum_{y'=y_c}^{y_c+\mathcal{Y}} I_c(y',x')\rangle_s} \right\rangle_f\right) \tag{6.4}$$

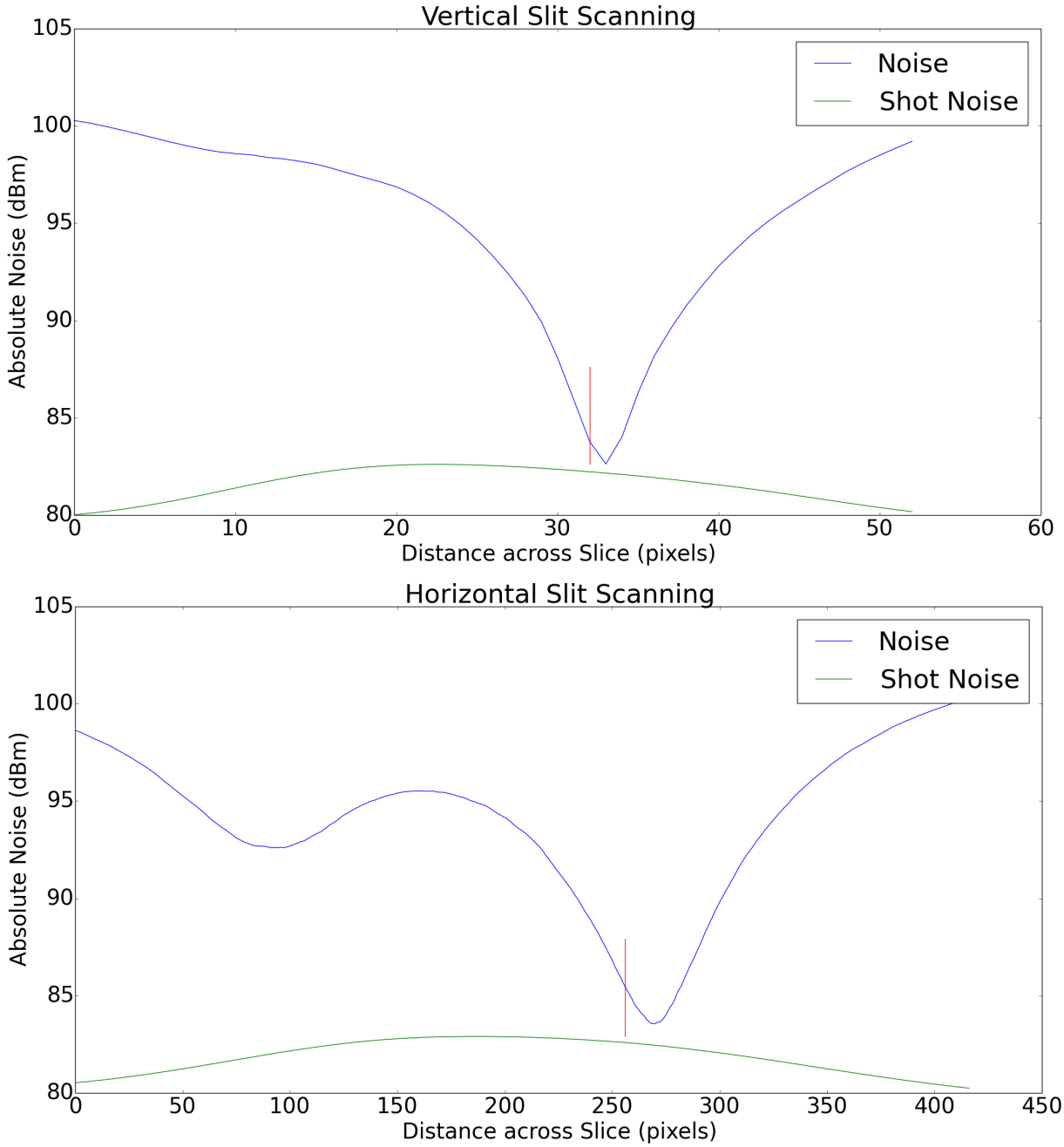

Figure 6.22: Slit scanning of results in Figure 6.11 to locate the approximate probe region correlated to a set region within the conjugate through intensity difference noise measurements. Also provided is the shot noise of the two regions (green line). The red line shows where the conjugate slits top and left side were placed in the vertical and horizontal scanning respectively.

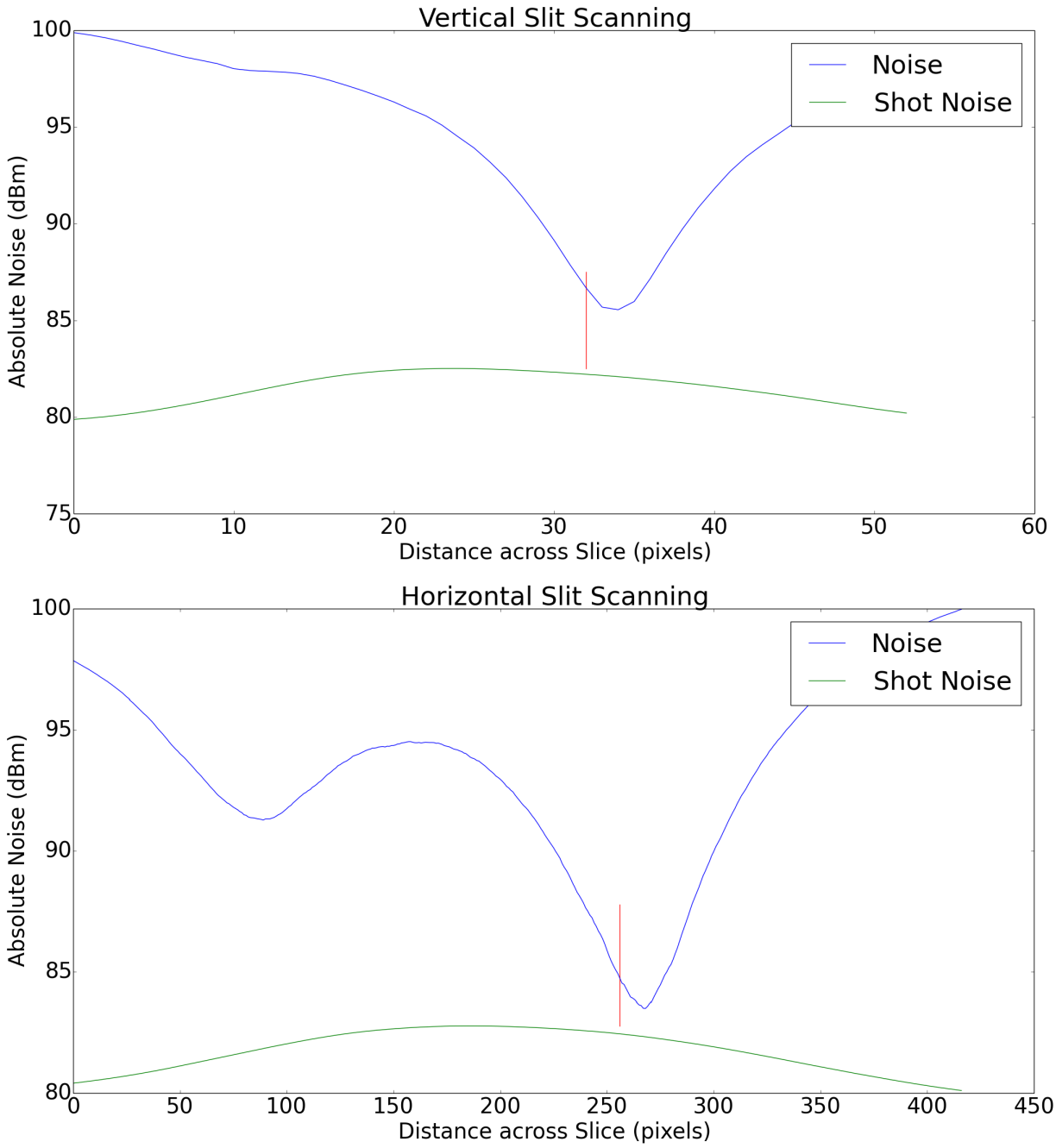

Figure 6.23: Slit scanning of results in Figure 6.15 to locate the approximate probe region correlated to a set region within the conjugate through intensity difference noise measurements. Also provided is the shot noise of the two regions (green line). The red line shows where the conjugate slits top and left side were placed in the vertical and horizontal scanning respectively.

All symbols in Equation 6.4 have their previous meaning, though now the QNR is a two-dimensional function. This is due to the algorithm's use of a window, which can be moved in both x and y simultaneously, as in Figure 6.21. Again, this procedure was applied first to the results from Figure 6.11 (no beamsplitter), yielding Figure 6.24.

While these results are also DC noise limited, they still display a similar result to the slit scanning algorithm. When applied to the images in Figure 6.15 (with beamsplitter), the window scanning algorithm produces Figure 6.25.

Both sets of results show a similar conclusion to the slit scanning algorithm, indicating that the beams are positioned as optimally as can be resolved by the camera's CCD.

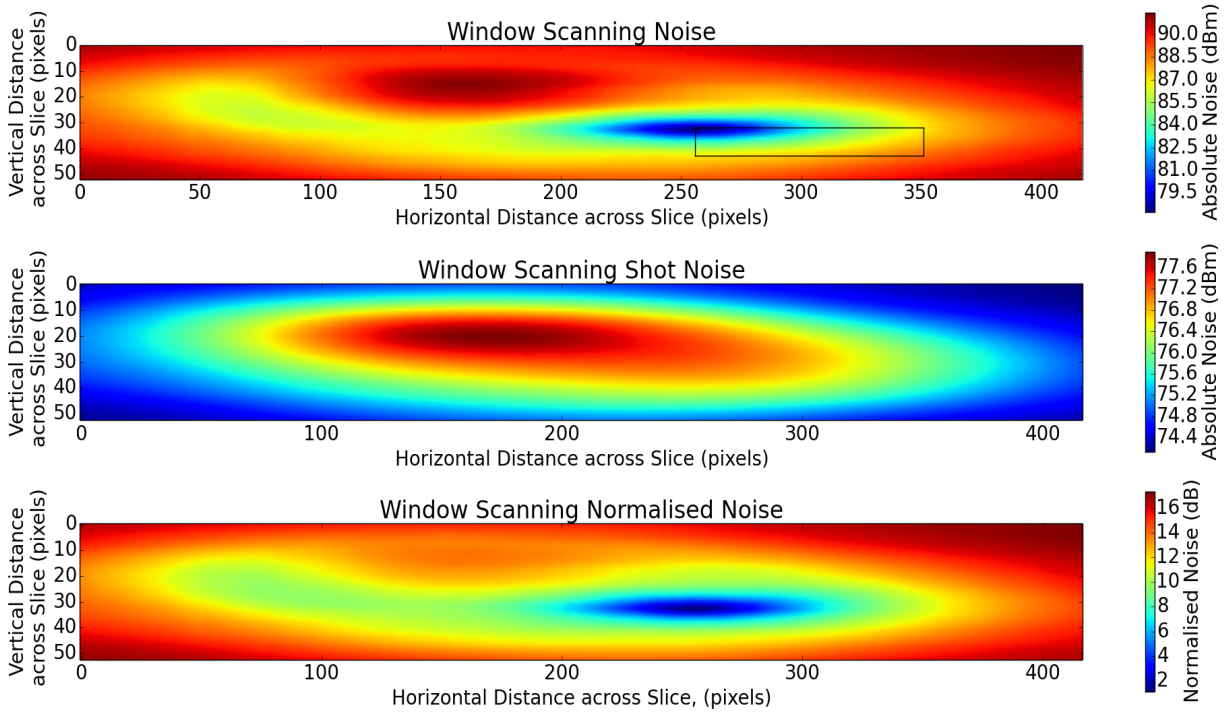

Figure 6.24: Window Scanning of the beams in Figure 6.11. The three different plots show absolute noise, shot noise and normalised noise. The black square in the absolute noise shows where the window was placed on the conjugate.

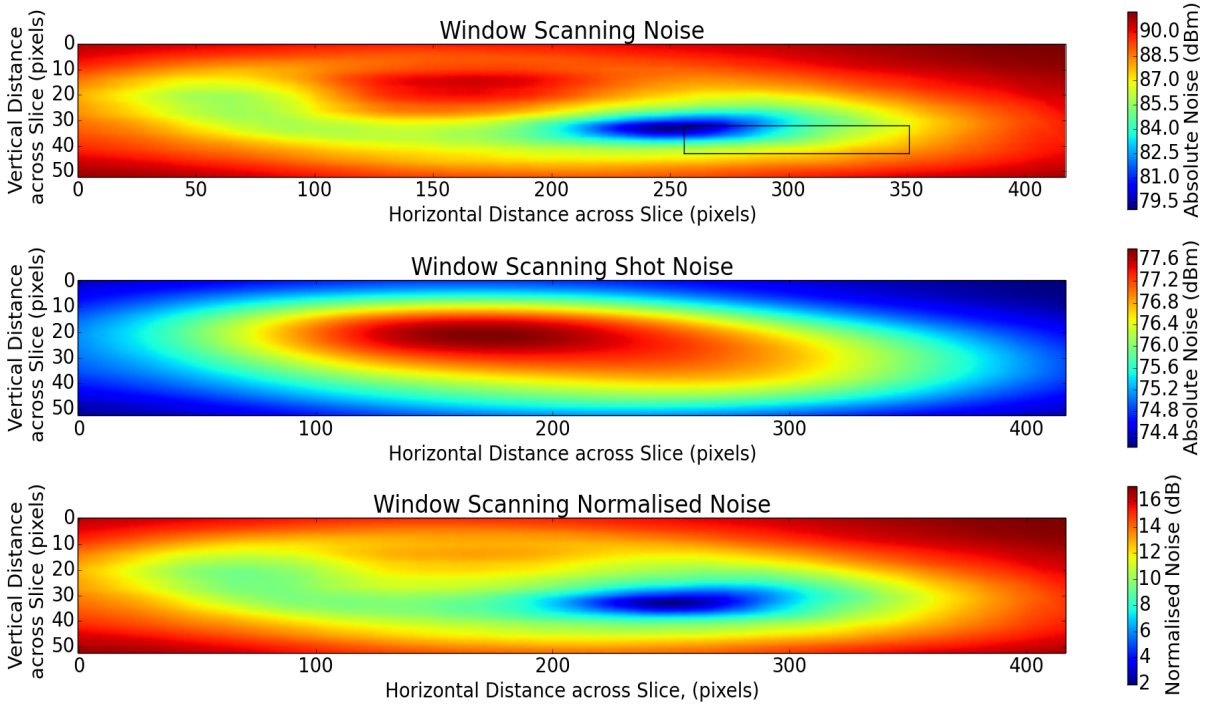

Figure 6.25: Window scanning of the beams in Figure 6.15. The three different plots show absolute noise, shot noise and normalised noise. The black square in the absolute noise shows where the window was placed on the conjugate.

6.2.2 Summary

Given this exhaustive computational investigation, the results have conclusively shown MSM squeezing in signal beams generated from 4WM in a Rb85 vapour. Using the results from Figure 6.11 (without beamsplitter), this squeezing is distributed across 8 distinct spatial modes, with vertical spatial frequencies of $\pm 4.96\text{mm}^{-1}$, $\pm 2.48\text{mm}^{-1}$ and 0mm^{-1} (DC) and horizontal frequencies $\pm 0.60\text{mm}^{-1}$, $\pm 0.30\text{mm}^{-1}$ and DC.

More specifically, these frequencies can be arranged in the following pairs, giving the (k_x, k_y)

coordinates of the circle of squeezed values in Figure 6.13:

$$(0\text{mm}^{-1}, 4.96\text{mm}^{-1}),$$

$$(0\text{mm}^{-1}, -4.96\text{mm}^{-1}),$$

$$(0.30\text{mm}^{-1}, 2.48\text{mm}^{-1}),$$

$$(-0.30\text{mm}^{-1}, -2.48\text{mm}^{-1}),$$

$$(-0.30\text{mm}^{-1}, 2.48\text{mm}^{-1}),$$

$$(0.30\text{mm}^{-1}, -2.48\text{mm}^{-1}),$$

$$(0.60\text{mm}^{-1}, 0\text{mm}^{-1}),$$

$$(-0.60\text{mm}^{-1}, 0\text{mm}^{-1})$$

These frequencies correspond to real space vertical sizes of 0.20mm and 0.40mm and horizontal sizes of 1.66mm and 3.33mm. The DC values correspond to the height and width of the slices, which were 0.83mm and 6.63mm respectively. The areas that can be calculated from these lengths can be seen to be MSM squeezed regions, given that the size of the beams in the results were larger than this. The average heights of the probe and conjugate were 0.70mm and 0.66mm respectively, while the average widths were 6.17mm and 5.95mm respectively. These beam sizes exceed the length scales derived from the spatial frequencies, inferring that they correspond to regions within the beams. As such, the beam can be decomposed into regions that are squeezed, thus indicating MSM squeezing.

Chapter 7

Conclusion

In summary, I have examined the theoretical work that describes the states and modes of light that can be exploited in pursuit of squeezing. I have explained how these states are established, firstly theoretically and secondly within a Rb85 medium. I have detailed the operation of the detection methods implemented in the experiment's of this thesis, and also noted how their loss can resultantly effect the squeezing.

I have discussed how the generation of BLO and vacuum states, combined appropriately, allows one to measure the quadratures of squeezed vacuum signals via BLO homodyne detection. I have specified the set-up required to ensure that such signals are overlapped with their BLOs, to ensure a clear beat frequency. I have then shown how this scheme yields results that show the squeezing bandwidth of 4WM in Rb85, and its multi-temporal mode nature.

I have also used this same generation of correlations to experimentally verify the transmission of said correlations through a rigid conduit. I have shown how the aforementioned correlations and their MSM characteristics are preserved throughout the waveguide, and thus still yield squeezing, through different isolated regions and measuring their correlation.

Finally, I have also attempted an experimental verification of near field MSM squeezing by the use of a CCD camera and an appropriate analysis, realising a spatial frequency spectrum analysis. I found compromised but promising results in the noise spectra calculated from the difference of the CCD-captured images.

These noise spectra displayed maximum detected squeezing of $\sim$-0.75dB across a range of regions, with widths 1.66mm and 3.33mm and heights 0.20mm and 0.40mm. Given the probe and conjugate both had approximate $1/e^2$ heights and widths of 0.70mm and 6mm respectively. Given that the squeezed spatial frequencies correspond to length scales that are smaller than these beam size, these results thus exhibit MSM squeezing. Due to the presence of anomalous noise however, it is unclear whether this maximum is the largest achievable squeezing using this set-up, or whether these length scales are the smallest possible regions that could be squeezed within the beams.

These experiments provide a proof of principle for the use and manipulation of correlations in various scenarios. In particular, the conduit and camera experiments provide the groundwork for further application of MSM correlations in quantum imaging. In particular, the conduit experiment lays the groundwork for the first steps in realising and applying integrated quantum imaging, while the camera experiment provides a similar foundation for the imaging of faint objects and their motion, such as particle tracking. Further work in this area can develop these successes further, including more robust and compact systems for real-life applications.

Appendix A

Verification of Harmonic Oscillator as an EM field

In Section 2.1.1, we were quantising a light field with the intent of manipulating it and its fluctuations to decrease the uncertainty in certain observables of interest. To do so, we assumed an EM field of the form:

$$\begin{aligned} \hat{E}_x(z,t) &= \sqrt{\frac{2\omega^2}{\epsilon}} q(t)\sin(kz), \\ \hat{B}_y(z,t) &= \frac{\mu_0\epsilon_0}{k}\sqrt{\frac{2\omega^2}{\epsilon}} p(t)\cos(kz). \end{aligned} \tag{A.1}$$

Here $q(t)$ and $p(t)$ are the canonical position and momentum factors for a harmonic oscillator, which, in the same section, we convert to operators through the correspondence rule, $\hat{q}(t)$ and $\hat{p}(t)$. We also note that, using Equations 2.2 to 2.11, these operators can be expressed

by:

$$\begin{aligned}\hat{q}(t) &= \sqrt{\frac{\hbar}{2\omega}}(\hat{a}(t) + \hat{a}^\dagger(t)),\\ \hat{p}(t) &= i\sqrt{\frac{\hbar\omega}{2}}(\hat{a}^\dagger(t) - \hat{a}(t)).\end{aligned} \tag{A.2}$$

Here, the time dependency of annihilation operator can be ascertained by considering the Hamiltonian in Equation 2.4. To this end, we substitute the operators in Equation A.2 into this Hamiltonian, giving:

$$\hat{H} = (\hat{a}^\dagger\hat{a} + \frac{1}{2})\hbar\omega \tag{A.3}$$

Using Equation A.3 with Heisenberg's equation, the time dependency can be found thus:

$$\begin{aligned}\frac{d\hat{a}}{dt} &= \frac{i}{\hbar}[\hat{H}, \hat{a}]\\ &= i\omega(\hat{a}^\dagger\hat{a}\hat{a} - \hat{a}\hat{a}^\dagger\hat{a})\\ &= -i\omega[\hat{a}, \hat{a}^\dagger]\hat{a}\\ &= -i\omega\hat{a}\end{aligned}$$

As $[\hat{a}, \hat{a}^\dagger] = 1$, we can see that

$$\frac{d\hat{a}}{dt} = -i\omega\hat{a}, \tag{A.4}$$

which has the solution

$$\hat{a}(t) = \hat{a}(0)e^{-i\omega t}. \tag{A.5}$$

The solution in Equation A.5 can be directly substituted into Equations A.2, yielding:

$$\begin{aligned}\hat{q}(t) &= \sqrt{\frac{\hbar}{2\omega}}(\hat{a}e^{-i\omega t} + \hat{a}^\dagger e^{i\omega t}),\\ \hat{p}(t) &= i\sqrt{\frac{\hbar\omega}{2}}(\hat{a}^\dagger e^{i\omega t} - \hat{a}e^{-i\omega t}).\end{aligned} \tag{A.6}$$

Thus, our proposed EM field in Equations A.1 was considered suitable on the basis that it's dependency on the annihilation operator, with it's subsequent dependency on time, fulfilled both Maxwell's equations and also the EM wave equations:

$$\begin{aligned}\left(c^2\nabla^2 - \frac{\partial^2}{\partial t^2}\right)\hat{E} = 0,\\ \left(c^2\nabla^2 - \frac{\partial^2}{\partial t^2}\right)\hat{B} = 0.\end{aligned} \tag{A.7}$$

Here we intend to show that Equations A.1 do indeed fulfil both requirements, and we begin with the electric field in A.7:

$$\begin{aligned}&\left(c^2\nabla^2 - \frac{\partial^2}{\partial t^2}\right)\hat{E}_x(z,t) =\\ &\left(c^2\nabla^2 - \frac{\partial^2}{\partial t^2}\right)\sqrt{\frac{2\omega^2}{\epsilon}}\hat{q}(t)\sin(kz) =\\ &\left(c^2\nabla^2 - \frac{\partial^2}{\partial t^2}\right)\sqrt{\frac{2\omega^2}{\epsilon}}\sqrt{\frac{\hbar}{2\omega}}(\hat{a}e^{-i\omega t} + \hat{a}^\dagger e^{i\omega t})\sin(kz) =\\ &\sqrt{\frac{2\omega^2}{\epsilon}}\sqrt{\frac{\hbar}{2\omega}}\left(c^2\nabla^2(\hat{a}e^{-i\omega t} + \hat{a}^\dagger e^{i\omega t})\sin(kz) - \frac{\partial^2}{\partial t^2}(\hat{a}e^{-i\omega t} + \hat{a}^\dagger e^{i\omega t})\sin(kz)\right) =\\ &\sqrt{\frac{2\omega^2}{\epsilon}}\sqrt{\frac{\hbar}{2\omega}}\sin(kz)(\hat{a}e^{-i\omega t} + \hat{a}^\dagger e^{i\omega t})\left(-c^2k^2 + \omega^2\right) = 0.\end{aligned}$$

As $c^2k^2 = \omega^2$, we thus find that:

$$\sqrt{\frac{2\omega^2}{\epsilon}}\sqrt{\frac{\hbar}{2\omega}}\sin(kz)(\hat{a}e^{-i\omega t} + \hat{a}^\dagger e^{i\omega t})\left(-\omega^2 + \omega^2\right) = 0, \tag{A.8}$$

which is clearly evident, and so verifies that our electric field from Equation A.2 is theoretically

suitable and consistent. We now use the same approach for the magnetic field:

$$\left(c^2\nabla^2 - \frac{\partial^2}{\partial t^2}\right)\hat{B}_y(z,t) =$$
$$\left(c^2\nabla^2 - \frac{\partial^2}{\partial t^2}\right)\sqrt{\frac{2\omega^2}{\epsilon}}\hat{p}(t)\cos(kz) =$$
$$\left(c^2\nabla^2 - \frac{\partial^2}{\partial t^2}\right)i\sqrt{\frac{2\omega^2}{\epsilon}}\sqrt{\frac{\hbar\omega}{2}}(\hat{a}^\dagger e^{i\omega t} - \hat{a}e^{-i\omega t})\cos(kz) =$$
$$i\sqrt{\frac{2\omega^2}{\epsilon}}\sqrt{\frac{\hbar}{2\omega}}\left(c^2\nabla^2(\hat{a}^\dagger e^{i\omega t} - \hat{a}e^{-i\omega t})\cos(kz) - \frac{\partial^2}{\partial t^2}(\hat{a}^\dagger e^{i\omega t} - \hat{a}e^{-i\omega t})\cos(kz)\right) =$$
$$i\sqrt{\frac{2\omega^2}{\epsilon}}\sqrt{\frac{\hbar}{2\omega}}\cos(kz)(\hat{a}^\dagger e^{i\omega t} - \hat{a}e^{-i\omega t})\left(-c^2k^2 + \omega^2\right) = 0.$$

Again, as $c^2k^2 = \omega^2$, we also find that:

$$i\sqrt{\frac{2\omega^2}{\epsilon}}\sqrt{\frac{\hbar}{2\omega}}\cos(kz)(\hat{a}^\dagger e^{i\omega t} - \hat{a}e^{-i\omega t})\left(-\omega^2 + \omega^2\right) = 0 \tag{A.9}$$

which, once again, is clearly evident and so verifies that our proposed EM field is valid.

Appendix B

Derivation of Intensity Difference Variance

In Section 2.3.2, we were deriving the variance of two correlated signal fields output from an amplifier with a seed state given by $|\alpha, 0\rangle$. The signal annihilation operators are given by Equation 2.25:

$$\begin{aligned} \hat{b}_1 &= \sqrt{G}\hat{a}_1 + \sqrt{G-1}\hat{a}_2^\dagger, \\ \hat{b}_2 &= \sqrt{G}\hat{a}_2 + \sqrt{G-1}\hat{a}_1^\dagger. \end{aligned} \tag{B.1}$$

These then provide the number operators of the signals, $\hat{n}_1 = \hat{b}_1^\dagger \hat{b}_1$ and $\hat{n}_2 = \hat{b}_2^\dagger \hat{b}_2$. The intensity difference, I_- is thus proportional to $\langle \hat{n}_1 - \hat{n}_2 \rangle$, the variance of which is given by:

$$\begin{aligned} \langle (\Delta I)^2 \rangle &\propto \langle (\Delta(\hat{n}_1 - \hat{n}_2))^2 \rangle \\ &= \langle (\hat{n}_1 - \hat{n}_2)^2 \rangle - \langle \hat{n}_1 - \hat{n}_2 \rangle^2. \end{aligned} \tag{B.2}$$

Given that the seed state is comprised of two states, one being a number state $|0\rangle$, we also

note that the annihilation operator operates on number states as follows:

$$\begin{aligned}\hat{a}|n\rangle &= \sqrt{n}|n-1\rangle, \\ \hat{a}^\dagger|n\rangle &= \sqrt{n+1}|n+1\rangle.\end{aligned} \tag{B.3}$$

Thus, for any $\hat{a}_1$ that is not preceded by $\hat{a}_1^\dagger$ the seed state $|0\rangle$ returns an eigenvalue of 0. Hence, this fact can be used in tandem Equation B.1 to provide expressions for $\hat{n}_1$ and $\hat{n}_2$ in Equation B.2. We can now calculate the averages required to obtain the variance, starting with $\langle(\hat{n}_1 - \hat{n}_2)^2\rangle$:

$$\begin{aligned}\langle(\hat{n}_1 - \hat{n}_2)^2\rangle = \langle &(G-1)^2\hat{a}_2\hat{a}_2^\dagger\hat{a}_2\hat{a}_2^\dagger + G^2 + \hat{a}_1^\dagger\hat{a}_1\hat{a}_1^\dagger\hat{a}_1 + 1 \\ &- 2G(G-1)\hat{a}_2\hat{a}_2^\dagger + 2(G-1)\hat{a}_2\hat{a}_2^\dagger\hat{a}_1^\dagger\hat{a}_1 \\ &+ 2(G-1)\hat{a}_2\hat{a}_2^\dagger - 2G\hat{a}_1^\dagger\hat{a}_1 - 2G + 2\hat{a}_1^\dagger\hat{a}\rangle \\ &+ (G-1)^2 + G^2 + |\alpha|^2 + |\alpha|^4 + 1 - 2G(G-1) \\ &+ 2(G-1)|\alpha|^2 + 2(G-1) - 2G|\alpha|^2 - 2G + 2|\alpha|^2 \\ &= |\alpha|^2 + |\alpha|^4\end{aligned} \tag{B.4}$$

We then move onto the other part of the variance, $\langle\hat{n}_1 - \hat{n}_2\rangle^2$:

$$\langle\hat{n}_1 - \hat{n}_2\rangle^2 = (\langle\hat{n}_1\rangle - \langle\hat{n}_2\rangle)^2 \tag{B.5}$$

where

$$\begin{aligned}\langle\hat{n}_1\rangle &= (\sqrt{G}\hat{a}_1 + \sqrt{G-1}\hat{a}_2^\dagger)^\dagger(\sqrt{G}\hat{a}_1 + \sqrt{G-1}\hat{a}_2^\dagger) \\ &= G\hat{a}_1^\dagger\hat{a}_1 + \sqrt{G(G-1)}\hat{a}_1^\dagger\hat{a}_2^\dagger + \sqrt{G(G-1)}\hat{a}_2\hat{a}_1 + (G-1)\hat{a}_2\hat{a}_2^\dagger \\ &= G|\alpha|^2 + (G-1)\end{aligned}$$

and

$$\begin{aligned}\langle\hat{n}_2\rangle &= (\sqrt{G}\hat{a}_2 + \sqrt{G-1}\hat{a}_1^\dagger)^\dagger(\sqrt{G}\hat{a}_2 + \sqrt{G-1}\hat{a}_1^\dagger) \\ &= G\hat{a}_2^\dagger\hat{a}_2 + \sqrt{G(G-1)}\hat{a}_2^\dagger\hat{a}_1^\dagger + \sqrt{G(G-1)}\hat{a}_1\hat{a}_2 + (G-1)\hat{a}_1\hat{a}_1^\dagger \\ &= G + (G-1)|\alpha|^2\end{aligned}$$

yielding:

$$\begin{aligned}\langle\hat{n}_1\rangle - \langle\hat{n}_2\rangle &= G|\alpha|^2 + G - 1 - G - G|\alpha|^2 + |\alpha|^2 \\ &= |\alpha|^2 - 1 \end{aligned} \tag{B.6}$$

We now consider $|\alpha|^2$ to be significantly large enough to ignore other smaller terms. Thus we find that:

$$(\langle\hat{n}_1\rangle - \langle\hat{n}_2\rangle)^2 = |\alpha|^4. \tag{B.7}$$

Hence Equations B.4 and B.7 give the two terms needed to calculate the variance of the photon number. We now substitute these terms into our original variance equation yielding:

$$\begin{aligned}\langle(\Delta(\hat{n}_1 - \hat{n}_2))^2\rangle &= \langle(\hat{n}_1 - \hat{n}_2)^2\rangle - \langle\hat{n}_1 - \hat{n}_2\rangle^2 \\ &= |\alpha|^2 + |\alpha|^4 - |\alpha|^4 \\ &= |\alpha|^2\end{aligned}$$

Thus, referring back to Equation B.2, we conclude that the variance of the intensity difference is proportional to $|\alpha|^2$.

Appendix C

Derivation of Intensity Difference Variance with Loss

In Section 4.2.2, we were attempting to observe the effects of loss on relative intensity squeezing, where we introduced Equation 3.11:

$$\langle(\Delta I_{-D})^2\eta_{11}^2\langle(\Delta\hat{n}_1)^2\rangle + \eta_{11}(1-\eta_{11})\langle\hat{n}_1\rangle + \eta_{21}^2\langle(\Delta\hat{n}_2)^2\rangle + \eta_{21}(1-\eta_{21})\langle\hat{n}_2\rangle - 2\eta_{11}\eta_{21}cov(\hat{n}_1,\hat{n}_2). \tag{C.1}$$

To proceed to the result, 3.12, we first recall that the probe and conjugate signals are linked to the probe seed, n, via the gain, G of the amplifier the seed passes into. This dependency gives the following variances:

$$\begin{aligned}\langle(\Delta\hat{n}_1)^2\rangle &= G^2\langle(\Delta\hat{n})^2\rangle + G(G-1)\langle\hat{n}\rangle,\\ \langle(\Delta\hat{n}_2)^2\rangle &= (G-1)^2\langle(\Delta\hat{n})^2\rangle + G(G-1)\langle\hat{n}\rangle.\end{aligned} \tag{C.2}$$

The covariance of the squeezing process can then be obtained by observing the invariance of

the number difference operator under the squeezing transformation, which implies that:

$$\begin{aligned}\langle(\Delta\hat{n})^2\rangle &= \langle(\Delta(\hat{n}_1-\hat{n}_2))^2\rangle - 2\mathrm{cov}(\hat{n}_1,\hat{n}_2)\\ &\Rightarrow \mathrm{cov}(\hat{n}_1,\hat{n}_2) = \frac{1}{2}(\langle(\Delta\hat{n})^2\rangle - \langle(\Delta\hat{n}_1)^2\rangle - \langle(\Delta\hat{n}_2)^2\rangle)\end{aligned} \tag{C.3}$$

Combining Equations C.2 and C.3, the relative intensity variance of squeezed beams after losses is given by:

$$\begin{aligned}&\langle(\Delta(\hat{n}_1-\hat{n}_2))^2\rangle = (\eta_1 G - \eta_2(G-1))^2\langle(\Delta\hat{n})^2\rangle +\\ &(\eta_1 G(\eta_1 G - 2\eta_1 + 1) + \eta_{21}(G-1)(\eta_2 G - \eta_2 + 1) - 2\eta_p\eta_2 G(G-1))\langle\hat{n}\rangle.\end{aligned} \tag{C.4}$$

For a shot-noise limited seed beam, $\langle(\Delta\hat{n})^2\rangle = \langle\hat{n}\rangle$, simplifying Equation C.4, the QNR, to the resultant Equation 3.12:

$$\frac{\langle(\Delta(\hat{n}_1-\hat{n}_2))^2\rangle}{\langle\hat{n}\rangle} = 2G^2(\eta_{11}-\eta_{21})^2 + G\eta_{11}(1-2\eta_{11}) + (G-1)\eta_{21}(1-2\eta_{21}) + 2G\eta_{21}(2\eta_{11}-\eta_{21}). \tag{C.5}$$

Appendix D

RF Components in Pulsed Set-Up

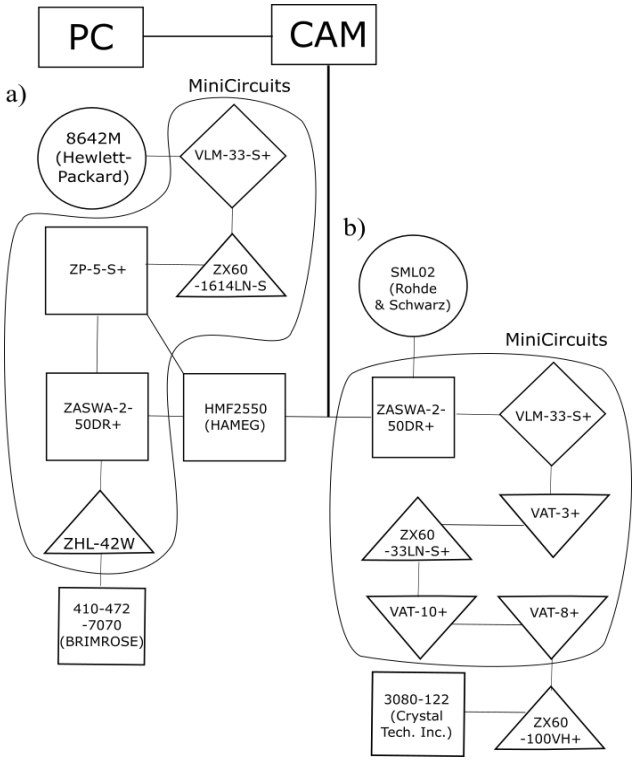

Figure D.1: The RF components used in providing pulses to the AOMs. Diagram a) shows the probe AOM RF supply chain. Diagram b) shows the pump AOM RF supply chain.

List of References

[1] Klauder, J.R. & Sudarshan, E.C.G. (1968) *Fundamentals of Quantum Optics*. New York: W.A. Benjamin, Inc.

[2] Louisell, W.H. (1973) *Quantum Statistical Properties of Radiation*. New York: John Wiley & Sons.

[3] Haken, H. (1985) *Light, Volume I: Waves, Photons and Atoms*. North Holland Publishing Company.

[4] Fox, M. (2006) *Quantum Optics: An Introduction*. Oxford University Press.

[5] Knight, P. & Gerry, C. (2008) *Introductory Quantum Optics*. Cambridge University Press.

[6] Einstein, A. (1917) *The Quantum Theory of Radiation*. Physikalische Zeitschrift, Vol. 18, Issue 121.

[7] Heitler, W. (1954) *The Quantum Theory of Radiation*. Oxford University Press..

[8] Roychoudhuri, C., Roy, R., Zajonc, A., Loudon, R., Finkelstein, D., Muthukrishnan, A., Scully, M.O., Zubairy, M.S., Mack, H. and Schleich, W.P. (2003) *The Nature of Light: what is a photon?*. Optics and Photonics News.

[9] Hong, S.H. & Javidi, B. (2004) *Improved resolution 3D object reconstruction using computational integral imaging with time multiplexing*. Optics Express, Vol. 12, Issue 19.

[10] Cheng, J. (2009) *Ghost imaging through turbulent atmosphere*. Optical Express, Vol. 17, Issue 10.

[11] Miller, S.E., Marcatali, E.A.J. & Li, T. (1973) *Research Toward Optical-Fiber Transmission Systems*. Proceedings of the IEEE, Vol. 61, Issue 12.

[12] Alferness, R. (1981) *Guided-Wave Devices for Optical Communication*. IEEE Journal of Quantum Electronics, Vol. 17, Issue 6.

[13] Xiaoying L., Chen, J., Voss, P., Sharping, J. and Kumar, P. (2004) *All-fiber photon-pair source for quantum communications: Improved generation of correlated photons*. Optical Express, Vol. 12, Issues 16.

[14] Halder, M., Beveratos, A., Thew, R.T., Jorel, C., Zbinden, H. & Gisin, N.. (2008) *High coherence photon pair source for quantum communication*. New Journal of Physics, Vol. 10, Issue 2.

[15] Kuzmich, A., Bowen, W. P., Boozer, A. D., Boca, A., Chou, C. W., Duan, L.-M. & Kimble, H. J. (2003) *Generation of nonclassical photon pairs for scalable quantum communication with atomic ensembles*. Nature, Vol. 423.

[16] Heisenberg, W. (1927) *Über den anschaulichen Inhalt der quantentheoretischen Kinematik und Mechanik*. Zeitschrift für Physik, Vol. 43, Issue (3-4).

[17] Kennard, E.H. (1927) *Zur Quantenmechanik einfacher Bewegungstypen*. Zeitschrift für Physik, Vol. 44, Issue 4.

[18] Bransden, B.H. & Joachain, C.J. (2000) *Quantum Mechanics*. Prentice Hall.

[19] Glauber, R.J. (1963) *Coherent and Incoherent States of the Radiation Field*. Physical Review, Vol. 131, Issue 6.

[20] Walls, D.F. (1983) *Squeezed States of Light*. Nature, Vol. 306.

[21] Einstein, A. (1905). *Concerning an Heuristic Point of View Toward the Emission and Transformation of Light*. Annalen Phys., Vol. 17.

[22] Bohr, N. (1913) *On the Constitution of Atoms and Molecules*. The London, Edinburgh, and Dublin Philosophical Magazine and Journal of Science, Vol. 26, Issue 151.

[23] de Broglie, L. (1925) *Recherches sur la thorie des quanta*. Ann. de Physique Vol. 10, Issue 3.

[24] Heisenberg, W. (1925) *Quantum theoretical re-interpretation of kinematic and mechanical relations*. Zeitschrift für Physik, Vol. 33.

[25] Schrodinger, E. (1926) *Quantisierung als Eigenwertproblem*. Annalen der Physik., Vol. 384, No. 4.

[26] Dirac, P.A.M. (1925) *The fundamental equations of quantum mechanics*. Proceedings of the Royal Society of London A: Mathematical, Physical and Engineering Sciences, Vol. 109, Issue 752.

[27] Born, M., Heisenberg, W. & Jordan, P. (1926) *Zur Quantenmechanik. II*. Zeitschrift fr Physik, Vol. 35, Issue 8-9.

[28] Dirac, P. A. M. (1928) *The quantum theory of the electron*. Proceedings of the Royal Society of London A: Mathematical, Physical and Engineering Sciences, Vol. 117, Issue 778.

[29] Fermi, E. (1932) *Quantum Theory of Radiation*. Review of Modern Physics, Vol. 4, Issue 1.

[30] Einstein, A., Podolsky, B., and Rosen, N. (1935) *Can Quantum-Mechanical Description of Physical Reality Be Considered Complete?* Physical Review, Vol. 47, Issue 10.

[31] Brown, R. H. & Twiss, R. Q. (1956) *Correlation between Photons in two Coherent Beams of Light*. Nature, Vol. 177.

[32] Maiman, T. H. (1960)*Stimulated Optical Radiation in Ruby*. Nature, volume 187.

[33] Wolf, E. (1959) *Coherence properties of partially polarized electromagnetic radiation* Il Nuovo Cimento, Vol. 13, Issue 6.

[34] Glauber, R.J. (1963) *The Quantum Theory of Optical Coherence*. Physical Review, Vol. 130, Issue 6.

[35] Sudarshan, E.C.G. (1963) *Equivalence of Semiclassical and Quantum Mechanical Descriptions of Statistical Light Beams*. Physical Review Letters, Vol. 10, Issue 7.

[36] Mehta, C.L. & Wolf, E. (1964) *Coherence Properties of Blackbody Radiation. I & II. Correlation Tensors of the Classical Field*. Physical Review, Vol. 134, Issue 5A.

[37] Mehta, C. L. & Sudarshan, E.C.G. (1965) *Relation between Quantum and Semiclassical Description of Optical Coherence*. Physical Review, Vol. 138, Issue 1B.

[38] Mehta, C.L & Sudarshan, E.C.G. (1966) *Time Evolution of Coherent States*. Physics Letters, Vol. 22, Issue 5.

[39] Mehta, C.L. & Wolf, E. (1967) *Coherence Properties of Blackbody Radiation. III. Cross-Spectral Tensors*. Physical Review, Vol. 161, Issue 5.

[40] Mehta, C.L., Chand, P., Sudarshan, E.C.G. & Vedam, R. (1967) *Dynamics of Coherent States* Physical Review, Vol. 157, Issue 5.

[41] Cahill, K.E. & Glauber, R.J. (1969) *Density Operators and Quasiprobability Distributions*. Physical Review, Vol. 177, Issue 5.

[42] Andersen, U.L., Gehring, T., Marquardt, C. & Leuchs, G. (2016) *30 years of squeezed light generation*. Physica Scripta, Vol. 91, Issue 5.

[43] Yuen, H. & Shapiro, J. (1978) *Optical communication with two-photon coherent states–Part I: Quantum-state propagation and quantum-noise*. IEEE Transactions on Information Theory, Vol. 24, Issue 6.

[44] Caves, C.M. (1982) *Quantum Noise Limits on Linear Amplifiers*. Physical Review D, Vol. 26, Issue 8.

[45] Kolobov, M.I. & Solokov, I.V. (1989) *Squeezed States of Light and Noise-Free Imaging*. Physics Letters A, Volume 140, Issue 3.

[46] Wu, L.A., Kimble, H.J., Hall, J.L. & Wu, H. (1986) *Generation of Squeezed States by Parametric Down Conversion*. Physical Review Letters, Vol. 57, Issue 20.

[47] Slusher, R.E., Hollberg, L.W., Yurke, B., Mertz, J.C. & Valley, J.F. (1985) *Observation of squeezed states generated by four-wave mixing in an optical cavity*. Physical Review Letters, Vol. 55, Issue 22.

[48] Slusher, R.E., Grangier, P., LaPorta, A., Yurke, B. & Potasek, M.J. (1987) *Pulsed Squeezed Light*. Physical Review Letters, Vol. 59, Issue 22.

[49] Slusher, R.E., Yurke, B., Grangier, P., LaPorta, A., Walls, D.F. & Reid, M. (1987) *Squeezed-light generation by four-wave mixing near an atomic resonance*. Journal of the Optical Society of America B, Vol. 4, Issue 10.

[50] Grangier, P., Slusher, R.E., Yurke, B. & LaPorta, A. (1987) *Squeezed-Light-Enhanced polarization interferometer*. Physical Review Letters, Vol. 59, Issue 19.

[51] Bennett, C.H. & Brassard, G. (1984) *Quantum cryptography: Public key distribution and coin tossing*. Proceedings of IEEE International Conference on Computers, Systems and Signal Processing, Vol. 175.

[52] Artur K. Ekert, A.K. (1991) *Quantum cryptography based on Bells theorem*. Physical Review Letters Vol. 67, Issue 6.

[53] Slusher, R.E. & Yurke, B. (1990) *Squeezed Light for Coherent Communications*. Journal of Lightwave Technology, Vol. 8, Issue 3.

[54] Kwiat, P.G., Mattle, K., Weinfurter, H., Zeilinger, A., Sergienko, A.V. & Shih, Y. (1995) *New High-Intensity Source of Polarization-Entangled Photon Pairs*. Physics Review Letters, Vol. 75, Issue 24.

[55] Beskrovnyy, V.N. & Kolobov, M.I. (2004) *Quantum limits of super-resolution in reconstruction of optical objects*. Physical Review A, Vol. 71, Issue 4.

[56] Poppe, A., Fedrizzi, A., Ursin, R., Böhm, H.R., Lorünser, T., Maurhardt, O., Peev, M., Suda, M., Kurtsiefer, C., Weinfurter, H., Jennewein, T. & Zeilinger, A. (2004) *Practical*

quantum key distribution with polarization entangled photons. Optics Express, Vol. 12, Issue 16.

[57] McCormick, C.F., Boyer, V., Arimondo, E. & Lett, P.D. (2007) *Strong relative intensity squeezing by four-wave mixing in rubidium vapor*. Optics Letters, Vol. 32, Issue 2.

[58] Vahlbruch, H., Mehmet, M., Chelkowski, S., Hage, B., Franzen, A., Lastzka, N., Goler, S., Danzmann, K. & Schnabel, R. (2008) *Observation of Squeezed Light with 10-dB Quantum-Noise Reduction*. Physical Review Letters, Vol. 100, Issue 3.

[59] Halder, M., Beveratos, A., Thew, R.T., Jorel, C., Zbinden, H. & Gisin, N. (2008) *High coherence photon pair source for quantum communication*. Journal of Physics, Vol. 10, Issue 2.

[60] Boyer, V., Marino, A.M. & Lett, P.D. (2008) *Generation of Spatially Broadband Twin Beams for Quantum Imaging*. Physical Review Letters, Vol. 100, Issue 14.

[61] Boyer, V., Marino, A.M., Pooser, R.C. & Lett, P.D. (2009) *Entangling light in its spatial degrees of freedom with four-wave mixing in an atomic vapor*. ChemPhysChem, Vol. 10, Issue 5.

[62] Eckstein, A., Christ, A., Mosley, P.J. & Silberhorn, C. (2009) *Highly Efficient Single-Pass Source of Pulsed Single-Mode Twin Beams of Light*. Physical Review Letters, Vol. 106, Issue 1.

[63] Corzo, N.V., Marino, A.M., Jones, K.M. & Lett, P.D. (2012) *Noiseless Optical Amplifier Operating on Hundreds of Spatial Modes*. Vol. 109, Issue 4.

[64] Walmsley, I.A. (2015) *Quantum optics: Science and technology in a new light*. Science, Vol. 348, Issue 6234.

[65] Embrey, C.S., Hordell, J.S.D., Petrov, P.G. & Boyer, V. (2016) *Bichromatic homodyne detection of broadband quadrature squeezing*. Optics Express, Vol. 24, Issue 24.

[66] Hordell, J.S.D., Benedicto-Orenes, D., Petrov, P.G., Kowalczyk, A.U., Barontini, G. & Boyer, V. (2018) *Transport of spatial squeezing through an optical waveguide*. Optics Express, Vol. 26, Issue 18.

[67] Embrey, C.S. (2015) *Controlling Local Quantum Fluctuations of Light Using Four-Wave Mixing in an Atomic Vapour*. Ph.D. Thesis, University of Birmingham.

[68] Jasperse, M. (2010) *Relative Intensity Squeezing by Four-Wave Mixing in Rubidium*. Masters Thesis, University of Melbourne.

[69] Boyd, R.W. (2008) *Nonlinear Optics*. Academic Press.

[70] Turnbull, M. (2014) *Multi-spatial-mode quadrature squeezing from four-wave mixing in a hot atomic vapour*. Ph.D. Thesis, University of Birmingham.

[71] Lukin, M.D., Hemmer, P.R., & Scully, M.O. (2000) *Resonant Nonlinear Optics in Phase-Coherant Media*. Advances in Atomic, Molecular and Optical Physics, Vol. 42.

[72] Turnbull, M.T., Petrov, P.G., Embrey, C.S., Marino, A.M. & Boyer, V. (2013) *Role of the phase-matching condition in nondegenerate four-wave mixing in hot vapors for the generation of squeezed states of light*. Physical Review A, Vol. 88, Issue 3.

[73] Steck, D. (December 2010) Rubidium 85 D Line Data. http://steck.us/alkalidata, revision 2.1.4 edition.

[74] Lopez. L, Chalopin, B., Rivière de la Souchère, A., Fabre, C., Maître, A. & Treps, N. (2009) *Multimode quantum properties of a self-imaging optical parametric oscillator: Squeezed vacuum and Einstein-Podolsky-Rosen-beams generation*. Physical Review A, Vol. 80, Issue 4.

[75] Goodman, J. (1996) *Introduction to Fourier Optics*. McGraw Hill Higher Education.

[76] Embrey, C.S., Turnbull, M.T., Petrov, P.G. & Boyer, V. (2015) *Observation of Localized Multi-Spatial-Mode Quadrature Squeezing*. Physics Review X, Vol. 5, Issue 3.

[77] Kumar, A., Nunley, H. & Marin, A.M. (2017) *Observation of spatial quantum correlations in the macroscopic regime*. Physical Review A, Vol. 95, Issue 5.